Chapter 12
Applications

The previous chapters demonstrate the capabilities of the bond graph methodology in tackling various basic engineering problems and how various software programmes support this methodology. In this chapter, application of the methodology in various engineering fields is illustrated by considering a number of small case studies. Some of these examples have been analysed elsewhere in the literature without making use of bond graphs. Bond graph models of further examples can be found in text books on bond graph modelling published in various languages and in many research papers. As to text books, readers are referred to, e.g. [13, 17, 21, 29], just to mention a few. In most of the following case studies, the integrated modelling and simulation environment 20-sim®[7], version 3.2, has been used. The open source mathematical software package Scilab [26] and the root finding version LSODAR of the ODE solver LSODA [14, 23] as part of Scilab has been used for the example of a clutch (Section 12.6) and for the example of a quarter vehicle (Section 12.7).

12.1 Inverted Pendulum

In feedback control of engineering systems, the inverted pendulum is often chosen as an example in order to show how a controller can be designed for stabilising an inherently unstable system. The equations of motion are usually set up directly by considering forces and moments in a free body diagram. In [13], Gawthrop and Smith gave a library model for the planar motion of a rigid rod and adapted it to the case of a simple inverted pendulum hinged to a cart. In [29], Vergé and Jaume applied the general multibond graph approach to modelling rigid multibody systems. In this section, it is shown how easily a bond graph model can be developed by graphically representing velocity constraints derived from geometric constraints. From the completed bond graph with all I energy storage elements in derivative causality, equations of motion are derived in the form of Lagrange equations of the second kind.

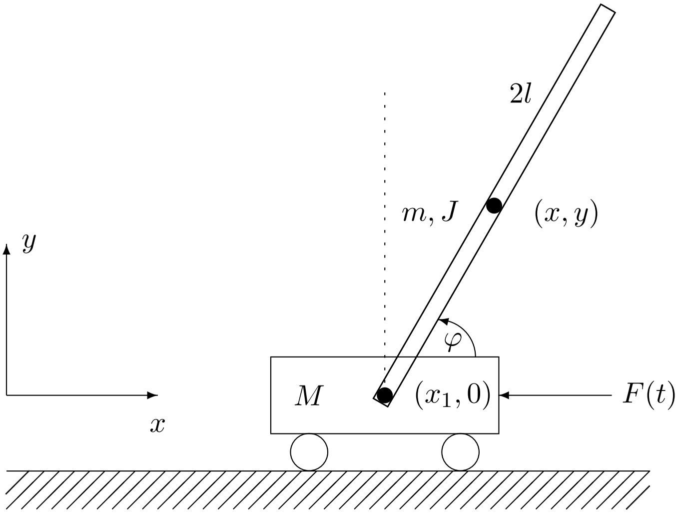

Fig. 12.1 Schematic of an inverted pendulum

Development of a Bond Graph Model

Figure 12.1 shows a schematic of the inverted pendulum with a uniform rigid rod of length $2l$, mass m, moment of inertia J about its centre of mass hinged to a rigid cart of mass M. The cart is pushed by a force $F(t)$.

The schematic provides the following two geometric relations.

$$x = x_1 + l\cos\varphi \tag{12.1a}$$

$$y = l\sin\varphi \tag{12.1b}$$

Differentiation with respect to time gives

$$\dot{x} = \dot{x}_1 - l\dot{\varphi}\sin\varphi = (-l\sin\varphi)\dot{\varphi} + \dot{x}_1 \tag{12.2a}$$

$$\dot{y} = l\dot{\varphi}\cos\varphi = (l\cos\varphi)\dot{\varphi}\,. \tag{12.2b}$$

The velocity constrains 12.2a–12.2b can be represented by the bond graph of Figure 12.2.

A bond graph of the inverted pendulum is obtained by simply adding effort sources, I elements and the resistor R : b representing friction between the wheels of the cart and the ground. For simplicity, a linear friction characteristic is assumed. The completed bond graph is depicted in Figure 12.3.

Note that derivative causality has been assigned to all I elements. The two flow sources with a vanishing effort into the source are artificial flow sources introduced by Karnopp [16]. They resolve the causal conflicts at the 1-junctions they are attached to and indicate the generalised coordinates x_1 and φ (cf. Section 4.10).

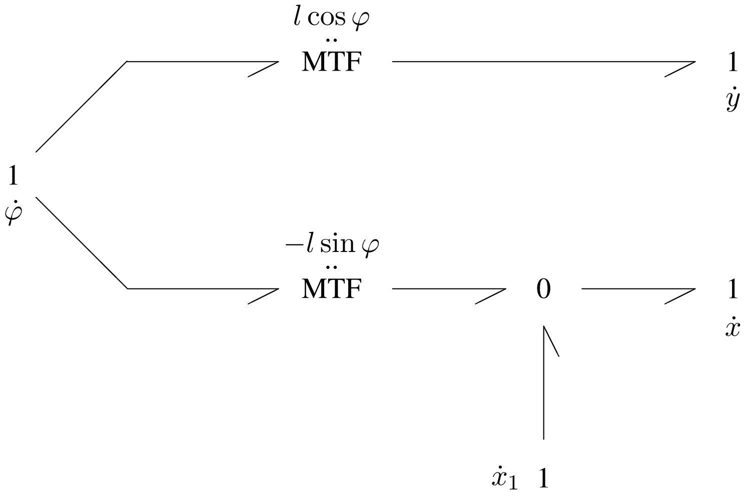

Fig. 12.2 Bond graph representation of the velocity constraints 12.2a–12.2b

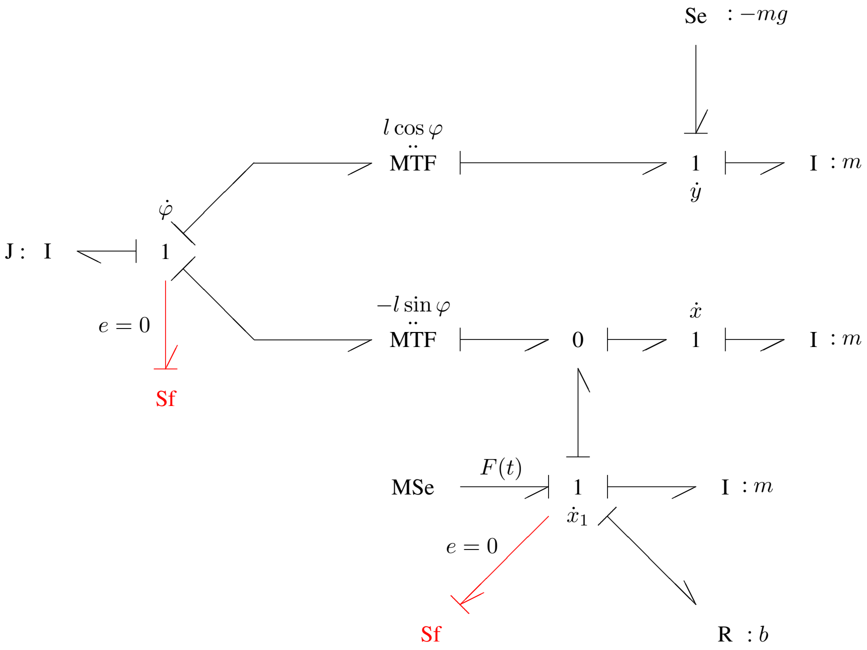

Fig. 12.3 Bond graph of the inverted pendulum

Deriving Lagrange Equations from the Bond Graph

Clearly, the system has two degrees of freedoms. Summing up all moments at the left 1-junction representing $\dot{\varphi}$ gives one of the two Lagrange equations of the second kind.

$$\begin{aligned} 0 &= J\ddot{\varphi} \;+\; l\cos\varphi\,(m\ddot{y} \;+\; mg) \;+\; (-l\sin\varphi)\,m\ddot{x} \\ &= J\ddot{\varphi} \;+\; ml^2\cos\varphi\,(\ddot{\varphi}\cos\varphi \;-\; \dot{\varphi}^2\sin\varphi) \;+\; mgl\cos\varphi \\ &\quad -\; ml\sin\varphi\,[\ddot{x}_1 \;-\; l(\ddot{\varphi}\sin\varphi \;+\; \ddot{\varphi}^2\cos\varphi)] \\ &= (J \;+\; ml^2)\ddot{\varphi} \;-\; ml\,\ddot{x}_1\sin\varphi \;+\; mgl\cos\varphi \end{aligned} \tag{12.3}$$

Summation of all forces at the 1-junction representing $\dot{x}_1$ gives the Lagrange equation for the second degree of freedom.

$$\begin{aligned} 0 &= F(t) \;-\; M\ddot{x}_1 \;-\; m\,\ddot{x} \;-\; b\,\dot{x}_1 \\ &= F(t) -\; M\ddot{x}_1 \;-\; m\,[\ddot{x}_1 \;-\; (\ddot{\varphi}\sin\varphi \;+\; \dot{\varphi}^2\cos\varphi)] \;-\; b\,\dot{x}_1 \\ F(t) \;-b\,\dot{x}_1 &= (M \;+\; m)\,\ddot{x}_1 \;-\; ml\,\ddot{\varphi}\sin\varphi \;-\; ml\,\dot{\varphi}^2\cos\varphi \end{aligned} \tag{12.4}$$

Deriving Equations of Motion from the Lagrangian

For comparison, the equations of motion 12.3–12.4 shall be deduced also from the Lagrangian of the inverted pendulum. As the system has two degrees of freedom, the following equations are to be formed

$$\frac{d}{dt}\left(\frac{\partial L}{\partial \dot{x}_1}\right) \;-\; \frac{\partial L}{\partial x_1} = F(t) \;-\; b\,\dot{x}_1 \tag{12.5a}$$

$$\frac{d}{dt}\left(\frac{\partial L}{\partial \dot{\varphi}}\right) \;-\; \frac{\partial L}{\partial \varphi} = 0\;, \tag{12.5b}$$

where $L := T - V$ is the difference of the kinetic energy, T, and the potential energy V.

The kinetic energy is

$$\begin{aligned} T &= \frac{1}{2}M\,\dot{x}_1^2 \;+\; \frac{1}{2}m\,[(\dot{x}_1 - l\dot{\varphi}\sin\varphi)^2 \;+\; (\,l\dot{\varphi}\cos\varphi)^2] \;+\; \frac{1}{2}J\,\dot{\varphi}^2 \\ &= \frac{1}{2}(M + m)\,\dot{x}_1^2 \;+\; \frac{1}{2}m\,(-2l\,\dot{x}_1\dot{\varphi}\sin\varphi \;+\; l^2\,\dot{\varphi}^2) \;+\; \frac{1}{2}J\,\dot{\varphi}^2\;. \end{aligned} \tag{12.6}$$

The potential energy is

$$V \;=\; -mgl\;\sin\varphi\;. \tag{12.7}$$

Hence,

$$\begin{aligned} \frac{d}{dt}\left(\frac{\partial L}{\partial \dot{x}_1}\right) &= \frac{d}{dt}[(M + m)\,\dot{x}_1 \;-\; ml\,\dot{\varphi}\sin\varphi] \\ &= (M + m)\,\ddot{x}_1 \;-\; ml(\ddot{\varphi}\sin\varphi \;+\; \dot{\varphi}^2\cos\varphi) \end{aligned} \tag{12.8}$$

and

$$\frac{\partial L}{\partial x_1} = 0 \,. \tag{12.9}$$

Substitution of Equations 12.8 and 12.9 into Equation 12.5a gives Equation 12.4.

Furthermore,

$$\begin{aligned} \frac{d}{dt}\left(\frac{\partial L}{\partial \dot{\varphi}}\right) &= \frac{d}{dt}[-mgl\,\dot{x}_1 \sin\varphi \,+\, ml^2\,\dot{\varphi} \,+\, J\,\dot{\varphi}] \\ &= (J+ml^2)\,\ddot{\varphi} \,-\, ml(\ddot{x}_1\,\sin\varphi \,+\, \dot{x}_1\,\dot{\varphi}\cos\varphi) \end{aligned} \tag{12.10}$$

and

$$\frac{\partial L}{\partial \varphi} = -ml\,\dot{x}_1\,\dot{\varphi}\cos\varphi \,-\, mgl\cos\varphi \,. \tag{12.11}$$

Finally, substitution of Equations 12.10 and 12.11 into Equation 12.5b gives Equation 12.3.

Transfer Function of the Inverted Pendulum

Now, let $\varphi := \pi/2 + \phi$. For small ϕ, viz. small deviations from the vertical position of the rod, the equations of motion 12.3–12.4 can be linearised.

$$(J+ml^2)\,\ddot{\phi} \,-\, ml\,\ddot{x}_1 \,-\, mgl\,\phi = 0 \tag{12.12a}$$

$$(M+m)\,\ddot{x}_1 \,-\, ml\,\ddot{\phi} = F(t) \,-\, b\,\dot{x}_1 \tag{12.12b}$$

Laplace transform of the linearised equations of motions gives the transfer function

$$\frac{\mathscr{L}\phi}{\mathscr{L}F} = \frac{mls^2}{(\tilde{M}\tilde{J}-m^2l^2)s^4 \,+\, b\tilde{J}s^3 \,-\, mgl\tilde{M}s^2 \,-\, bmgls}\,, \tag{12.13}$$

where $\tilde{M} := M+m$ and $\tilde{J} := J+ml^2$.

As can be seen from the transfer function of Equation 12.13, there is a pole-zero cancellation at the origin. Furthermore, if the parameter values of Table 12.1 [12] are used, the transfer function has one positive real pole, $p_1 = 5.087$, in the right-half of the s-plane. This is in agreement with the fact that the open-loop system is unstable. Figure 12.4 shows a root locus plot and Figure 12.5 depicts a Nyquist plot of the uncontrolled cart-pendulum system.

Table 12.1 Parameters of the inverted pendulum

Parameter	Value	Units	Meaning
M	0.7429	kg	Cart mass
m	0.21	kg	Mass of the rigid rod
$2l$	0.61	m	Pendulum length
b	7.19	Ns/m	Friction between cart wheels and ground

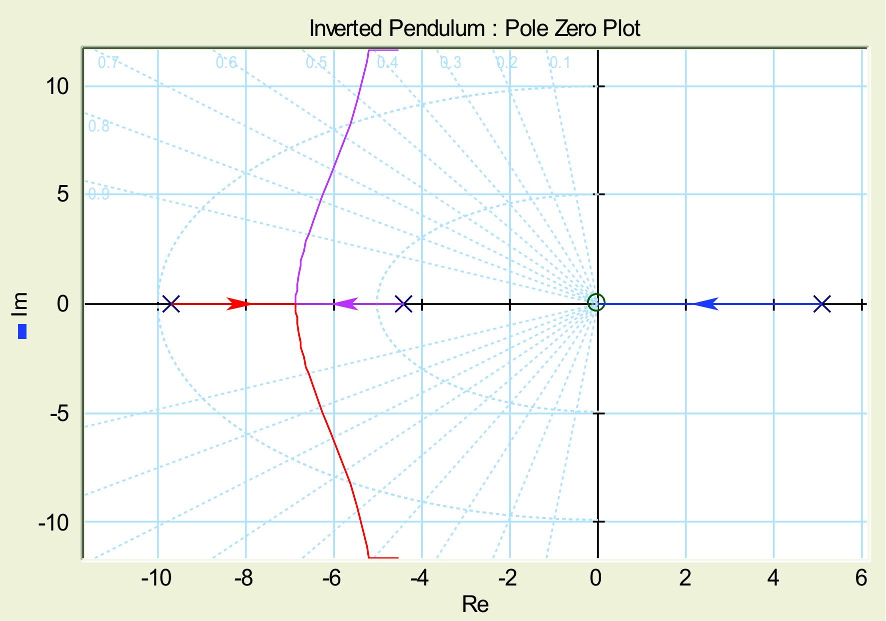

Fig. 12.4 Root locus plot of the uncontrolled cart-pendulum system

If $G(s)$ denotes the open-loop transfer function and $H(s)$ the transfer function of the feedback component then according to the Nyquist stability criterion, $H(s)$ has to be designed so that the Nyquist plot of $G(s)H(s)$ has one anti-clockwise encirclement of the point $-1 + j\,0$. As a result, the number of unstable closed-loop poles is zero. As the purpose of this section has been the development of a bond graph model of the inverted pendulum and the derivation of Lagrange equations of motion from the bond graph, the design of a controller for stabilisation of the unstable inverted pendulum is not considered. The control of the unstable inverted pendulum example has been addressed, for instance, in the textbook of F. Brown [3] (Guided Problem 8.2) and in the online tutorials authored by B. Messner and D. Tilbury [19].

12.2 Shunt Motor

In Chapter 11, a bond graph model of a shunt motor has been used as a reference example for illustration of various aspects. In this section, a small simulation study is carried out to determine the motor's dynamic response to a sudden increase of the load torque. For convenience, the schematic and the bond graph model are reproduced from Chapter 11 (Figures 12.6 and 12.7).

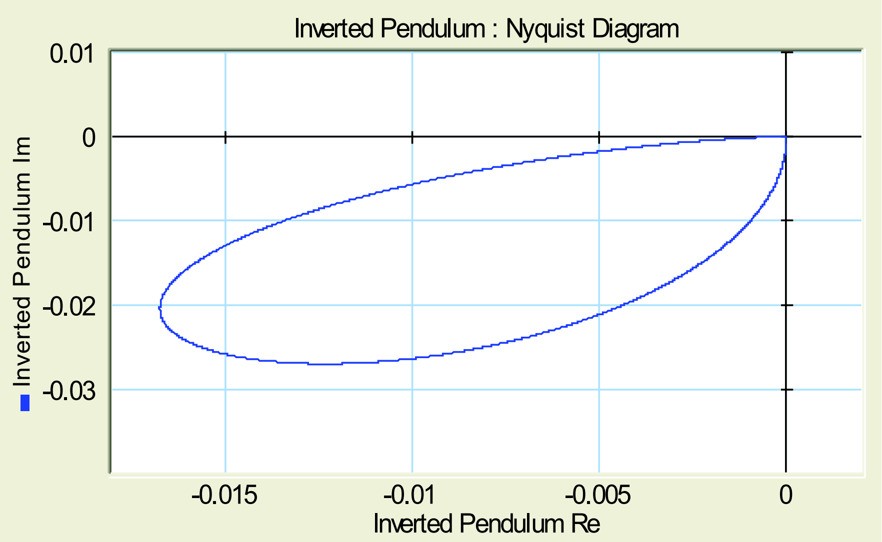

Fig. 12.5 Nyquist plot of the uncontrolled cart-pendulum system

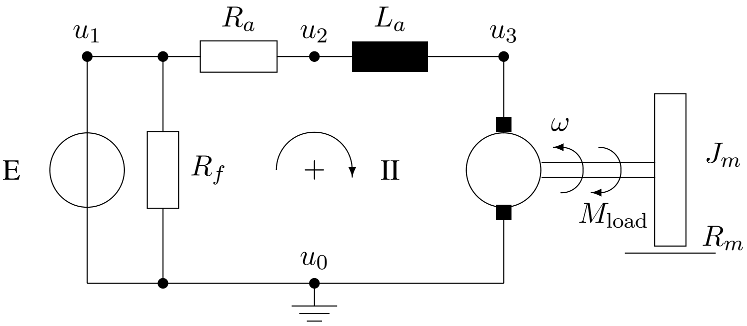

Fig. 12.6 Schematic of a shunt motor

From the causal bond graph in Figure 12.7, the following equations can be derived.

$$i_f = \frac{1}{R_f} E \tag{12.14a}$$

$$u_R = R_a \times i_a \tag{12.14b}$$

$$M_R = R_m \times \omega \tag{12.14c}$$

$$\Psi = K \times i_f \tag{12.14d}$$

$$u_a = \Psi \times \omega \tag{12.14e}$$

$$M = \Psi \times i_a \tag{12.14f}$$

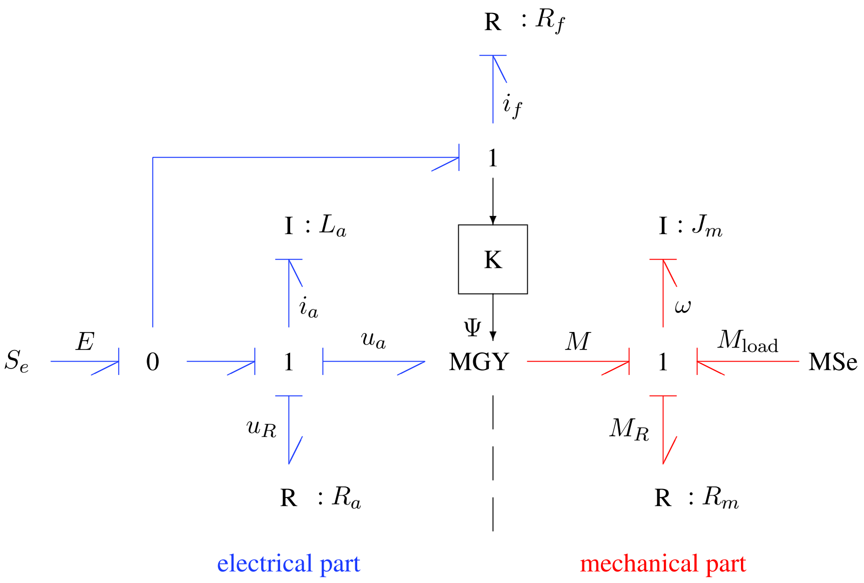

Fig. 12.7 Bond graph model of a shunt motor

$$\frac{di_a}{dt} = \frac{1}{L_a}(E - u_a - u_R) \tag{12.14g}$$

$$\frac{d\omega}{dt} = \frac{1}{J_m}(M - M_R + M_{\text{load}}) \tag{12.14h}$$

For the simulation study, it is assumed that the motor is driven by a constant voltage source. Its value is $E = 220\,V$. First, the motor's idling performance is analysed. Then, after $2.5\,s$, the motor is subjected to an immediate jump of the load torque to a constant value of $100\,Nm$. The parameters used for the simulation are listed in Table 12.2.

Table 12.2 Parameters of the simulation study

Parameter	Value	Units	Meaning
E	220	V	Voltage supply
R_f	5.495	Ω	Resistance of the field winding
R_a	0.875	Ω	Resistance of the armature winding
R_m	0.066	Nms	Friction coefficient
K	0.0307	Vs/A	$\Psi = K \times i_f$
L_a	0.175	H	Self-inductance of the armature winding
J_m	0.8	Nms^2	Moment of inertia of the flywheel
M_{load}	100	Nm	Load torque effective for $t \geq 2.5\,s$

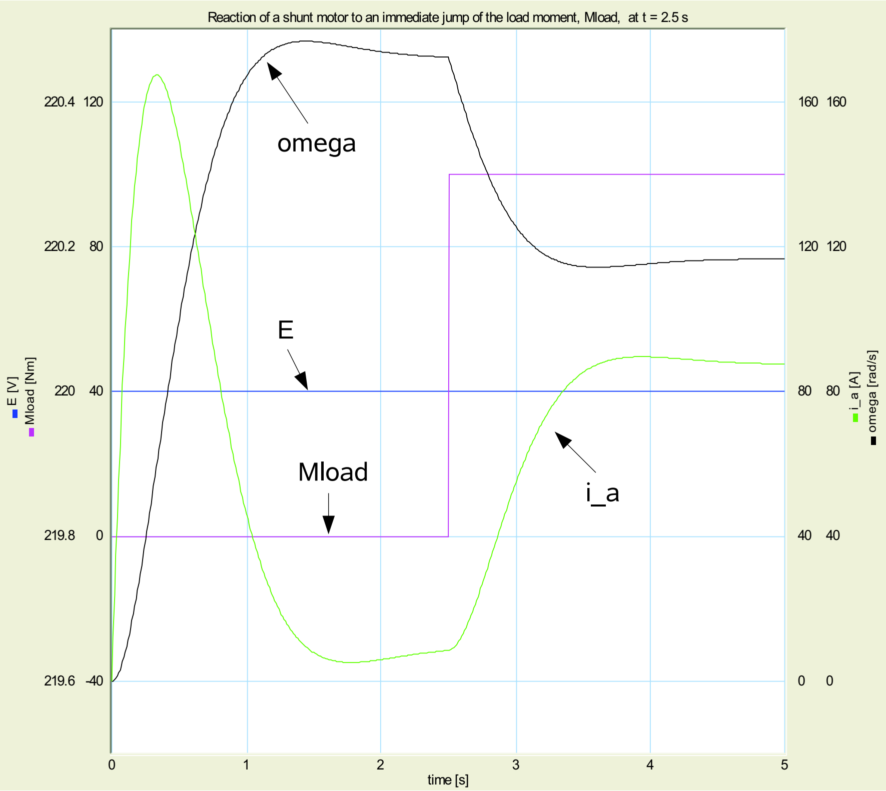

Fig. 12.8 Time evolution of the shaft velocity and the armature current

Simulation Results

Figure 12.8 shows the time evolution of the angular velocity, ω, of the motor shaft and of the current, i_a, through the armature winding. After switching on the voltage supply of the motor, the angular velocity rises and approches a steady idle speed value. During the rise time of the angular velocity, the current consumption reaches a maximum value and peaks off to low values when the angular velocity is around its steady state value.

Some algebra on the dynamic equations results in the following formulae for the steady state values i_a^0 and ω^0.

$$i_a^0 = \frac{R_f}{K\,E}\,R_m\,\omega^0 \tag{12.15a}$$

$$E = \left(\frac{K\,E}{R_f} + R_a\,\frac{R_f}{K\,E}\,R_m\right)\,\omega^0 \tag{12.15b}$$

With the parameters from Table 12.2, i_a^0 and ω^0 take the numerical values

$$i_a^0 = 9.257\ A \tag{12.16a}$$
$$\omega^0 = 172.4\ 1/s\ , \tag{12.16b}$$

which verifies the values obtained by simulation.

When the constant load torque becomes effective at $t = 2.5\,s$, then the angular velocity drops and the current consumption rise to new steady state values, as to be expected.

12.3 A Machine with an Unbalanced Rotor

An unbalanced mass has a feedback on the motor of a shaft-driven machine and can cause unwanted vibrations and noise of a machine mounted on springs. A motor mounted on springs as sketched in Figure 12.9 has been analysed by Christ in his dissertation in as early as 1966 [6].

As the differential equations are nonlinear, Hoffmann has chosen this example for a MATLAB®/Simulink® simulation that starts from given differential equations [15]. Such a spring mounted vertically moving machine is also briefly considered in the textbook by Brown ([3], Example 6.8), where a very simple bond graph is given.

Development of a Bond Graph Model

Similar to the case of the previous example of an inverted pendulum, in this section, the development of a bond graph model starts from considering the position of the unbalanced mass. Differentiation of its coordinates in a global frame with respect to time, again, provides velocity constraints that can be represented in a bond graph fragment. This bond graph for the kinematic constraints can be easily extended into a full dynamic model from which the equations of motion can be derived.

In a global frame, the position of the unbalanced mass, m_2, has the coordinates

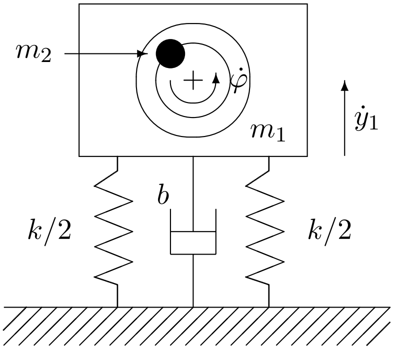

Fig. 12.9 Schematic of a machine with an unbalanced rotor

$$x_2 = 0 + e \sin\varphi \tag{12.3a}$$
$$y_2 = y_1 + e \cos\varphi \, . \tag{12.3b}$$

Differentiation with respect to time gives the velocity constraints

$$\dot{x}_2 = (e \cos\varphi)\, \dot{\varphi} \tag{12.4a}$$
$$\dot{y}_2 = \dot{y}_1 + (-e \sin\varphi)\, \dot{\varphi} \, . \tag{12.4b}$$

As for the rod of the inverted pendulum, the velocity constrains 12.4a–12.4b can be represented by the bond graph of Figure 12.10.

The bond graph fragment of Figure 12.10 is extended into a dynamic model of the machine by adding inertia elements to the 1-junctions, a C and an R element for the spring-damper pair and effort sources accounting for gravitational forces. Figure12.11 shows the resulting bond graph. The machine is driven by a DC motor with constant excitation providing a torque M_m. A bond graph of the motor is depicted in Figure 12.12.

Derivation of Model Equations from the Bond Graph

Summation of all forces at the 1-junction representing $\dot{y}_1$ gives

$$\begin{aligned} m_1 \ddot{y}_1 &= -m_1 g - b \dot{y}_1 - k y_1 - (m_2 g + m_2 \ddot{y}_2) \\ m_1 \ddot{y}_1 + b \dot{y}_1 + k y_1 &= -m_2 \ddot{y}_2 - (m_1 + m_2) g \, . \end{aligned} \tag{12.5}$$

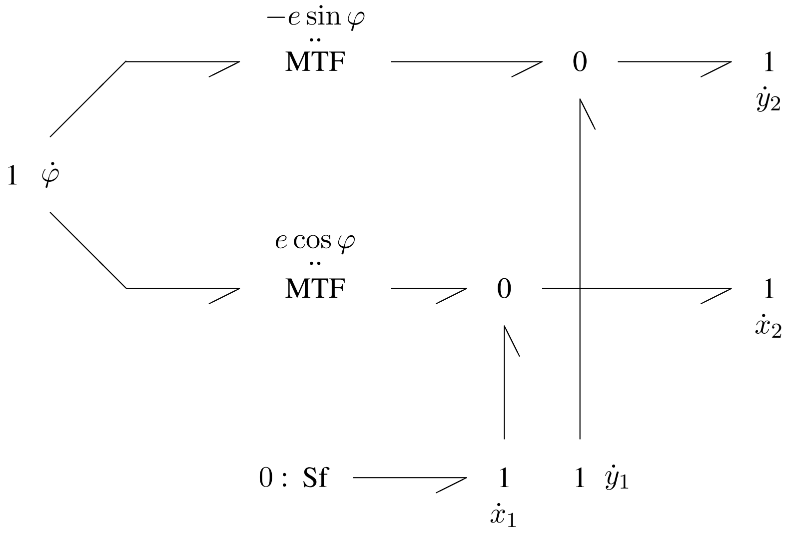

Fig. 12.10 Bond graph representation of the velocity constraints 12.4a–12.4b

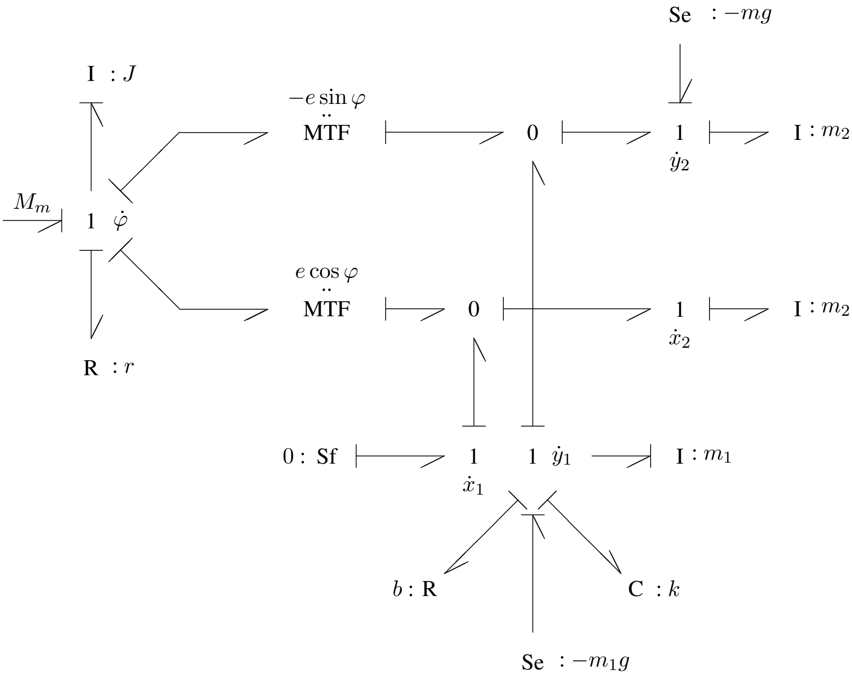

Fig. 12.11 Bond graph of the machine with an unbalanced mass

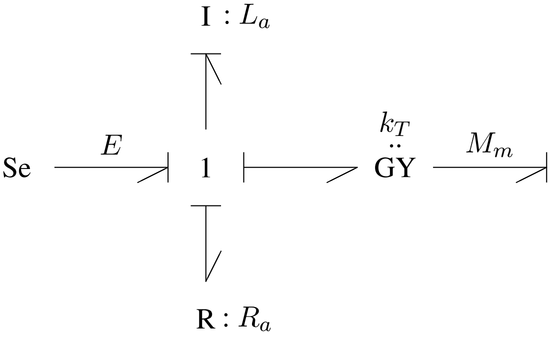

Fig. 12.12 Bond graph of the DC motor driving the machine with an unbalanced mass

The sum of flows at the upper 0-junction reads

$$\dot{y}_2 = (-e\sin\varphi)\,\dot{\varphi} + \dot{y}_1 \,. \tag{12.6}$$

The derivative causality of the I element attached to the 1-junction of $\dot{y}_2$ requires differentiation of Equation 12.6. Substitution of the result into Equation 12.5 yields the equation for the vertical motion of the machine.

$$\begin{aligned}(m_1 + m_2)\,\ddot{y}_1 + b\dot{y}_1 + ky_1 = m_2 e(\varphi^2\cos\varphi + \ddot{\varphi}\sin\varphi) - \\ (m_1 + m_2)g\end{aligned} \tag{12.7}$$

If the system is at rest, then the initial position is

$$y_{10} = -\frac{(m_1 + m_2)g}{k} \,. \tag{12.8}$$

If there is no unbalance with eccentricity e, then natural frequency of the undamped oscillation is

$$\omega_0 = \sqrt{\frac{k}{m_1 + m_2}} \,. \tag{12.9}$$

The unbalanced mass $m_2$with the eccentricity e causes the vertical excitation force

$$F_e = m_2 e(\varphi^2\cos\varphi + \ddot{\varphi}\sin\varphi) \,. \tag{12.10}$$

Summation of all moments at the 1-junction representing $\dot{\varphi}$ yields

$$\begin{aligned}M_m = J\,\ddot{\varphi} + r\dot{\varphi} + (-e\sin\varphi)(m_2\,\ddot{y}_2 + m_2 g) + \\ (e\cos\varphi)m_2\,\ddot{x}_2 \,.\end{aligned} \tag{12.11}$$

Again, summation of all flows at the 0-junctions yields $\dot{y}_2$ and $\dot{x}_2$. Derivative causality at both right-hand side I elements of mass m_2 requires differentiation with respect to time. After substitution of these time derivatives, the balance of moments reads

$$M_m = (J + m_2\,e^2)\,\ddot{\varphi} + r\,\dot{\varphi} - m_2\,e\,(\,\ddot{y}_1 + g)\,\sin\varphi \,. \tag{12.12}$$

From the bond graph of the DC motor in Figure 12.12, the following two equations are derived.

$$M_m = k_T\,i_a \tag{12.13a}$$

$$E = L_a\,\frac{di_a}{dt} + R\,i_a + k_T\,\dot{\varphi} \tag{12.13b}$$

Table 12.3 Parameters of the machine with an unbalanced mass

Parameter	Value	Units	Meaning
m_1	80	kg	Mass of the bed and the rotor
m_2	20	kg	Unbalanced mass
k	1600	N/m	Spring stiffness
b	4	Ns/m	Friction coefficient for translational motion
r	100	Nms	Friction coefficient for rotation
J	9.8	Nms^2	Moment of inertia
e	0.1	m	Eccentricity of m_2
La	1.0	H	Inductance of the armature winding
R_a	0.1	Ω	Resistance of the armature winding
k_T	50	Nm/A	Torque constant of the motor
E	100	V	Voltage applied to the motor

Simulation of the Machine with an Unbalanced Rotor

For simulation, the parameter values in Table 12.3 [15] have been used. If there is no eccentricity, then the rotor speed in steady state, ω_m, is

$$\omega_m = E/(R_a \frac{r}{k_T} + k_T) \ . \tag{12.14}$$

With the given parameter values, the angular velocity takes the value $\omega_m = 1.992 \text{ rad/s}$. The vertical vibration due to the unbalanced mass causes the angular velocity of the motor to oscillate around this mean value, as Figure 12.13 shows.

Furthermore, in case there is no eccentricity, the torque provided by the motor in steady state is

$$M_m = r \times \omega_m \ . \tag{12.15}$$

This steady state value is $M_m = 199.2 \text{ Nm}$. As ω_m oscillates around a mean value, so does the motor torque due to the vibration of the spring-mass system caused by the unbalanced mass m_2 (cf. Figure 12.14). Figure 12.15 shows the time evolution of the vertical oscillation, y_1, of the bed due to the unbalance.

Frequency Analysis of the Machine with an Unbalanced Rotor

A FFT of the time evolution of y_1 (cf. Figure 12.16) reveals that the vertical excitation force at mean angular frequency, $\omega_m = 1.992 \text{ rad/s}$, stimulates the resonant frequency, $\omega_0 = 4 \text{ rad/s}$ of the undamped spring-mass system, which is undesired.

If y_1 is replaced by $y_1 + y_{10}$ in Equation 12.7, then, by observing the expression for the excitation force F_e, Equation 12.10, the Laplace transform of Equation 12.7 gives

$$\frac{\mathscr{L} y_1}{\mathscr{L} F_e} = \frac{1}{(m_1 + m_2)\, s^2 \, + \, bs \, + \, k} \tag{12.16}$$

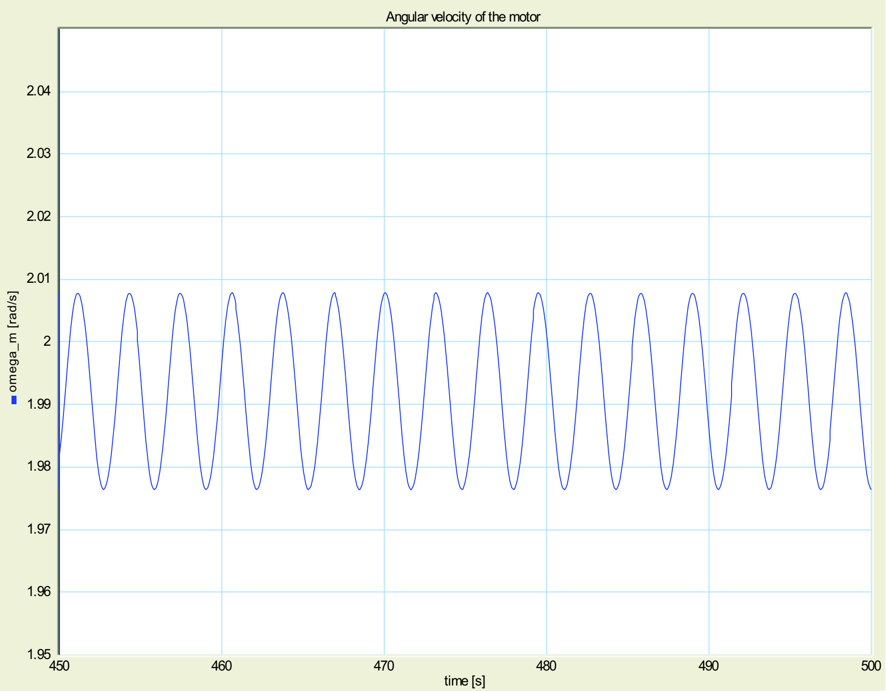

Fig. 12.13 Angular velocity of the motor

in case of a constant excitation frequency $\dot{\varphi} = \omega_m = \text{const}$.

Given the parameter values of Table 12.3, Figure 12.17 depicts the Bode plot of the transfer function of Equation 12.16. As can been seen, for excitation frequencies well above the natural frequency of the spring-mass system, the amplitude of the vertical oscillation rapidly decreases and the phase takes the constant value of -180^o degrees due to the system's inertia.

Reducing the value of the stiffness k of the spring supporting the bed from $1600\ \text{N/m}$ to $160\ \text{N/m}$ results in a natural frequency, $\omega_0 = 1.25\ \text{rad/s}$ of the undamped spring-mass system that is below the mean excitation frequency of the motor. Figure 12.18 shows the oscillation of the bed in case of a reduced spring stiffness. A FFT of the time evolution of y_1 shows that in steady state, the frequency of the vertical oscillation adapts to the excitation frequency (cf. Figure 12.19).

12.4 An Electronic Balance with Displacement Compensation

Figure 12.20 depicts a conceptual schematic of an electronic balance with displacement compensation. If there is no load on the weighing scale, then the gravitational

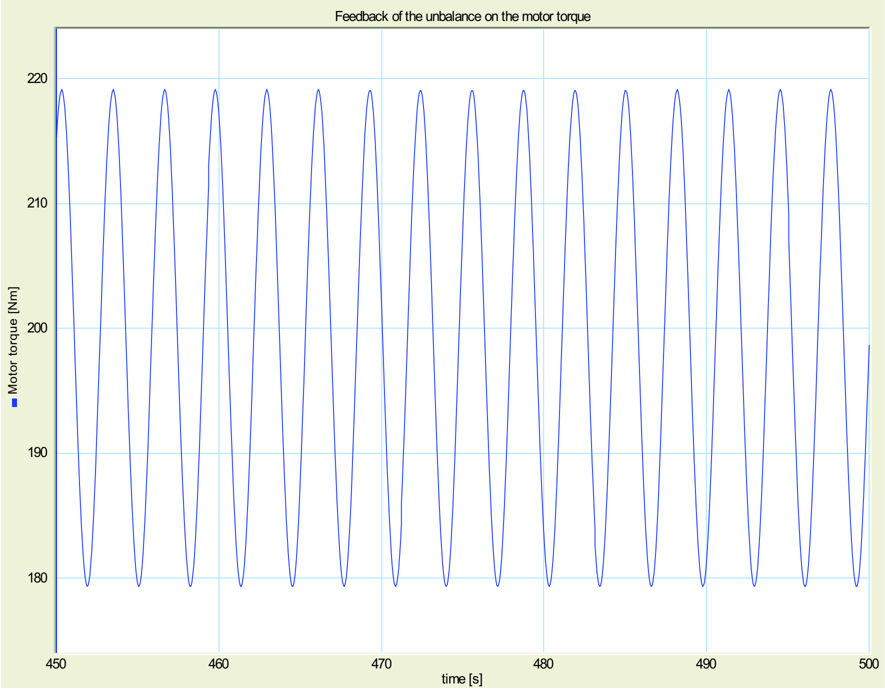

Fig. 12.14 Feedback of the unbalance on the motor torque

force of the scale pan and the spring force will be in equilibrium, defining the set point of the weighing scale's displacement set point $y = 0$. No voltage, E, is applied to the plunger coil and no current is flowing through the coil. Now, a load, m, causes a deviation from this set point. A current through the plunger coil causes an electromagnetic force that lifts the scale pan back into its initial position. The current needed to generate the electromagnetic force for compensation of the scale pan's displacement or the voltage applied to the coil can serve as a measure of the load. The electromechanical energy conversion in the coil can be represented by a gyrator.

Development of a Bond Graph Model

Construction of a bond graph model inspired by the topology of the schematic in Figure 12.20 is straightforward. Figure 12.21 shows the result. The lower 1-junction represents the current through the plunger coil. The attached R and I element account for its resistance and self-inductance. The upper 1-junction represents the velocity of load and scale pan against a spring and a damper force of the suspension. Finally, the Se source accounts for the gravitational force of the total mechanical load.

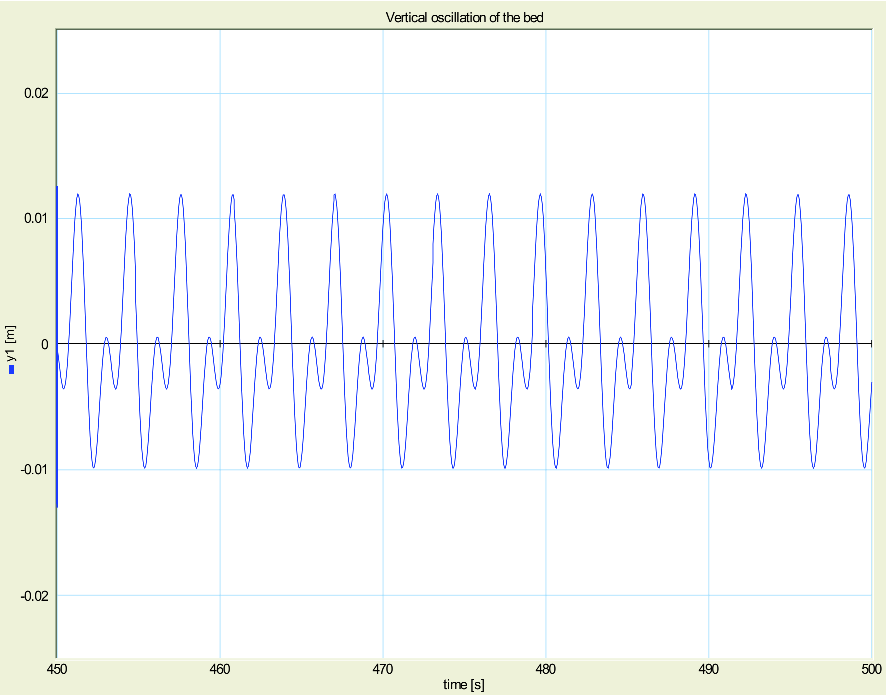

Fig. 12.15 Vertical oscillation y_1 of the bed due to the unbalance

The velocity of the load is sensed and integrated. The deviation from the set point is input into a controller. The output signal of the controller is fed into an amplifier with saturation. The amplifier's output is a voltage that is applied to the coil.

The sum of all efforts at the upper 1-junction yields the equation of motion for the mechanical part of the scale with respect to the equilibrium position.

$$-\,mg + T\,i \;=\; (m + m_b)\ddot{y} + r\dot{y} + k\,y \tag{12.17}$$

The sum of all efforts at the lower 1-junction results in an equation for the dynamic behaviour of the electrical part.

$$E(t) \;=\; L\,\frac{di}{dt} + Ri + T\dot{y} \tag{12.18}$$

The rules for assigning half arrows to the bonds of a bond graph help to ensure that signs in the model equations derived from the bond graph are consistent. This consistency is not automatically ensured if a free body diagram is used for the mechanical part of an electromechanical system and a conventional network for the electrical part. If a load m is put on the scale at some time, t, then, in steady state, the voltage

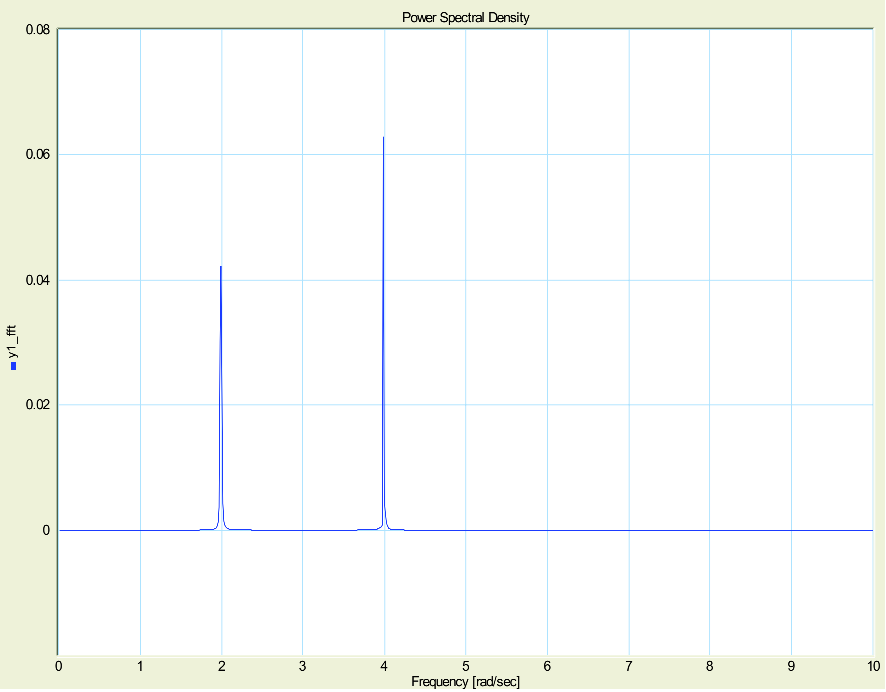

Fig. 12.16 Power spectral density of the vertical oscillation y_1

$$E_s = R\frac{mg}{T} \tag{12.19}$$

is needed to generate an electromagnetic force that compensates for the scale pan's displacement,

$$y_s = -\frac{mg}{k} \; . \tag{12.20}$$

In order to achieve a compensation of the scale's displacement, a PID controller is chosen.

Finally, putting a load on the scale at some time means that the mass of the scale pan is instantaneously increased. However, a rigid body with a time varying mass cannot be represented by a bond graph I element. That is, the I element in Figure 12.21 has to be replaced by a functional block implementing an equation of the form

```
p.f = int(p.e) / ( mb + m * step(tstart)) .
```
(12.21)

In this equation, `p.f` and `p.e` denote the effort and flow variables of port p. The effort is integrated by the function `int` and the function `step` produces a unity step at time `tstart`. The mass of the scale pan is `mb` which is increased by the mass `m` of the load.

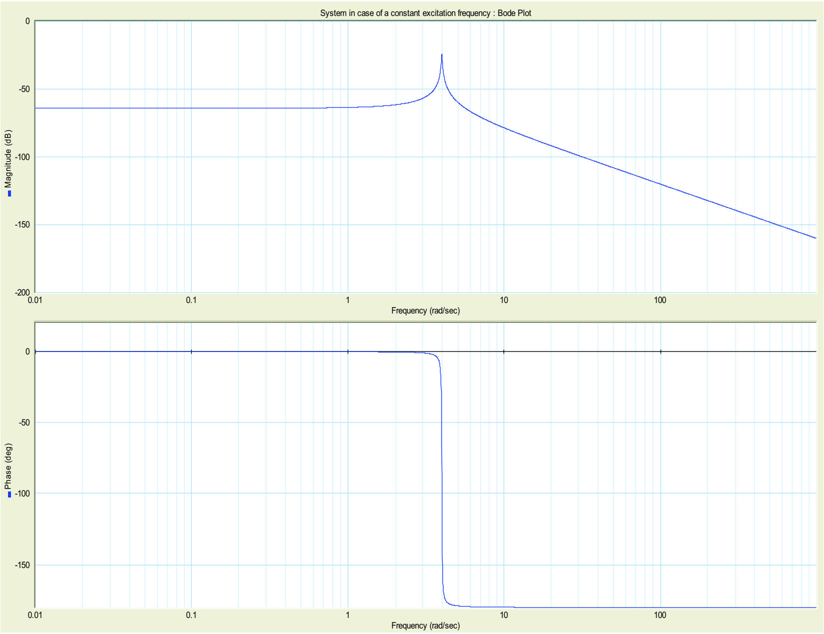

Fig. 12.17 Bode plot of the vertical oscillation case of a constant excitation frequency

Simulation of the Electronic Balance with Displacement Compensation

For simulation of the dynamic behaviour, the parameters given in Table 12.4 have been used [25].

The transfer function of the PID controller is used in the form

$$U(s) \;=\; K \left[1 + \frac{1}{T_i\, s} + \frac{T_d\, s}{1 + \dfrac{T_d}{N}\, s} \right] E(s) \;, \tag{12.22}$$

Table 12.4 Parameters of the controlled balance

Parameter	Value	Units	Meaning
R	1	Ω	Resistance of the coil
L	20	mH	Self-inductance of the coil
T	5	Vs	Transductance of the coil
k	1500	N/m	Stiffness of the spring
r	8.5	Ns/m	Damping coefficient
mb	0.03	kg	Mass of the scale pan
m	0.05	kg	Mass of the load

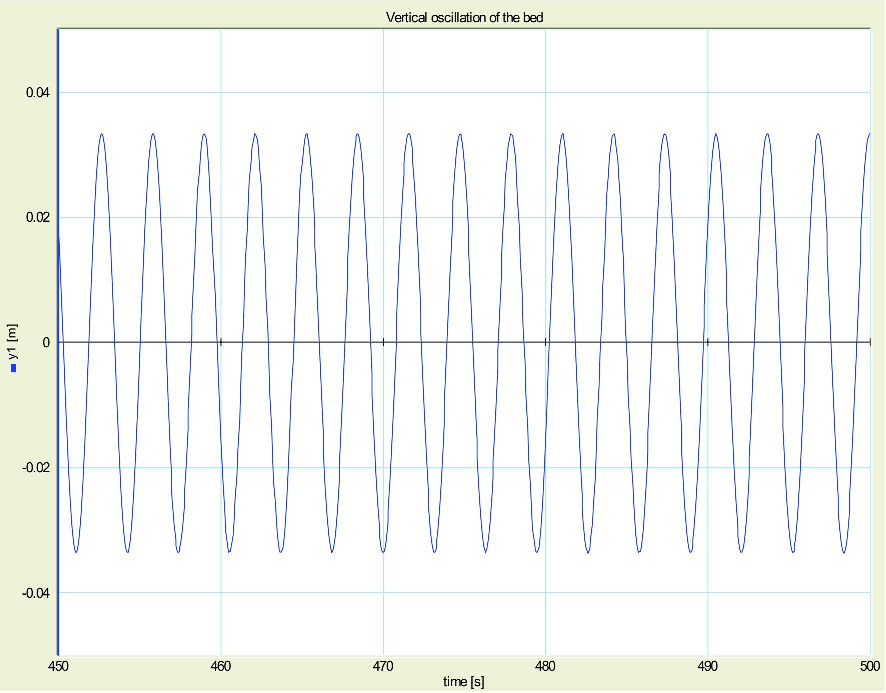

Fig. 12.18 Vertical oscillation y_1 of the bed in case of reduced spring stiffness

where $s \in \mathbb{C}$. In Equation 12.22, E and U denote the Laplace transforms of input and output. As can be seen, the derivative part is approximated. Table 12.5 lists the controller parameters.

Given the parameters in Table 12.4, the steady state value of the voltage needed to compensate the scale's displacement according to Equation 12.19 is

$$E_s \;=\; 1 \times \frac{0.05 \times 9.81}{5} \;=\; 98.1\, mV\ . \tag{12.23}$$

If this voltage is not applied to the coil, then the load of $m = 0.05\ kg$ would cause a displacement of

Table 12.5 Parameters of the PID controller

Parameter	Value	Units	Meaning
K	400		Proportional gain
Ti	0.05	s	Integral time constant
Td	0.01	s	Derivative time constant
N	20		Derivative gain limitation

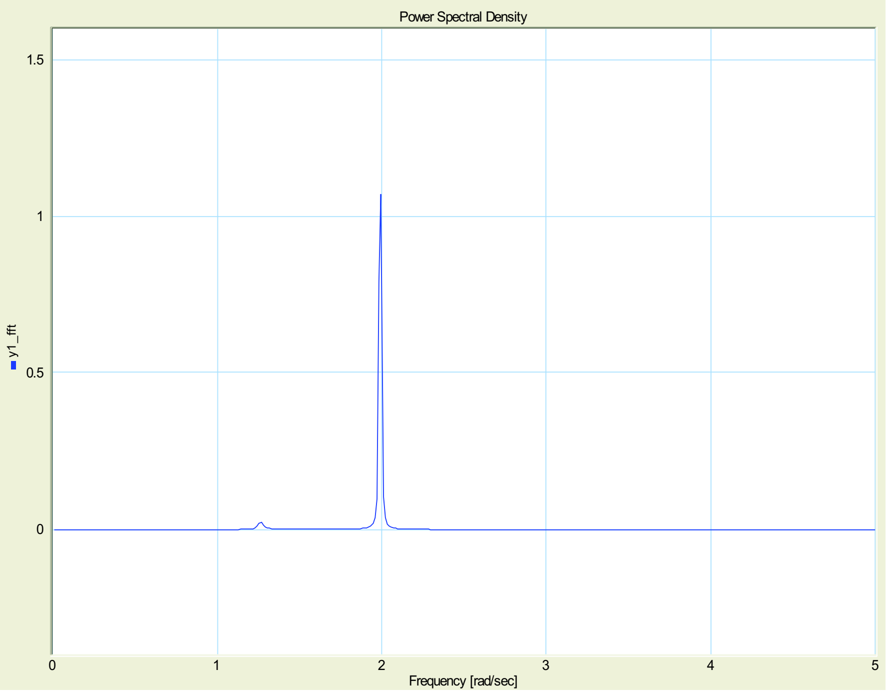

Fig. 12.19 Power spectral density of the vertical oscillation y_1 in case of reduced spring stiffness

$$y_s = -\frac{0.05 \times 9.81}{1500} = 0.33\,mm \tag{12.24}$$

according to Equation 12.20.

Figure 12.22 shows the time evolution of the current and the scale's displacement due to an instantaneous increase of the load from 0 to $0.05\,kg$ at $t = 0.2\,s$. As can be seen from Figure 12.22, the displacement, in fact, is compensated within about $0.4\ s$. When the mechanical load jumps from $0.03\ kg$ to $0.08\ kg$ at $t = 0.2\ s$, then the current just starts from $0\,A$. and the scale pan is lowered by about $0.2\ mm$. When this displacement is reduced to zero at about $t = 0.6\ s$, the current actually reaches the value of $98.1\ mA$, which is necessary for generating the electromagnetic force that compensates the gravitational force of the load.

As an instantaneous increase in the load does not only mean a disturbance of the gravitational load force but also the movement of a heavier body, the dynamic behaviour during compensation is different for different loads with respect to frequency and damping. Figure 12.23 depicts the time evolution of the displacement and the current in the coil for a four times heavier load.

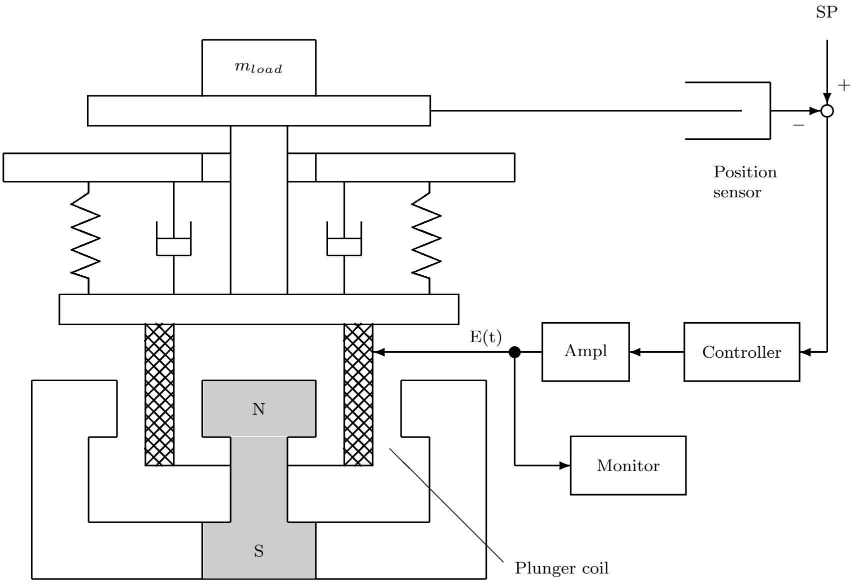

Fig. 12.20 Conceptual schematic of an electronic balance with displacement compensation (cf. [15])

12.5 A Piezoelectric Seismometer

This section addresses the bond graph modelling of a piezoelectric transducer and its use in a seismometer. A piezoelectric crystal can be considered an electromechanical transducer that mechanically behaves like a spring and electrically like a capacitor, and both effects are coupled. That is, a force imposed on the crystal produces results in a (small) voltage drop across the device and vice versa. Piezoelectric crystals are used, e.g. for sensing vibrations, for converting pressures into voltages, or as actuators in hydraulic control valves.

Bond Graph Model of the Piezoelectric Crystal

In the following, a one-dimensional model is considered. That is, it is assumed that mechanical stress or strain is applied in only one direction and the electric field lines are perpendicular to the parallel conductive surfaces of cross-sectional area A. Let x_0 denote the distance of these surfaces for the unbiased crystal. Let S denote the mechanical strain, $\Delta x = x_0 S$, the relative displacement of the parallel conductive surfaces, σ, the tensile stress, $F = A\sigma$, the associated force, E_m, the mechanical modulus of elasticity, E, the electric field strength, $u_p = x_0 E$, the applied voltage, D the electric displacement, ε, the dielectric constant and d_ε, the piezoelectric coupling. The constitutive relations of a piezoelectric crystal are assumed to be linear.

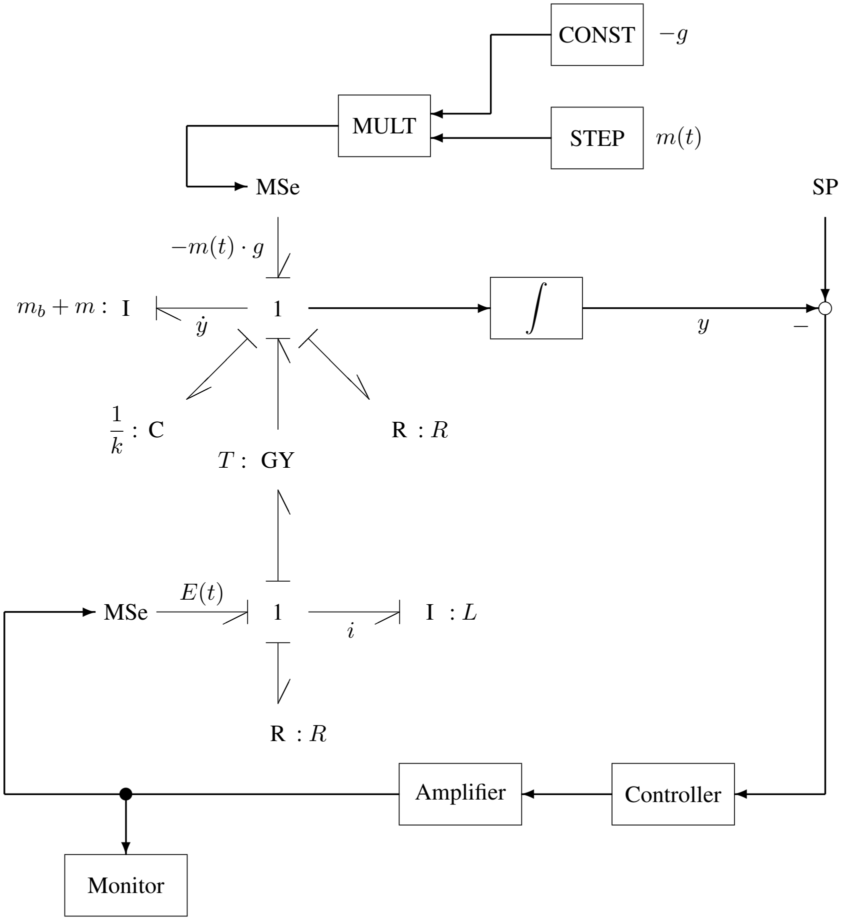

Fig. 12.21 Bond graph model of the electronic balance with displacement compensation

A commonly known form is

$$\begin{bmatrix} S \\ D \end{bmatrix} = \begin{bmatrix} 1/E_m & d_\varepsilon \\ d_\varepsilon & \varepsilon \end{bmatrix} \begin{bmatrix} \sigma \\ E \end{bmatrix} . \tag{12.25}$$

Given the introduced quantities, the constitutive relations can be rewritten as

$$\begin{bmatrix} \Delta x \\ q \end{bmatrix} = \begin{bmatrix} 1/k_p & d_\varepsilon \\ d_\varepsilon & C_p \end{bmatrix} \begin{bmatrix} F \\ u_p \end{bmatrix} , \tag{12.26}$$

where $k_p = EA/x_0$ denotes the mechanical stiffness of the piezoelectric crystal and $C_p = \epsilon A/x_0$, its electrical capacitance.

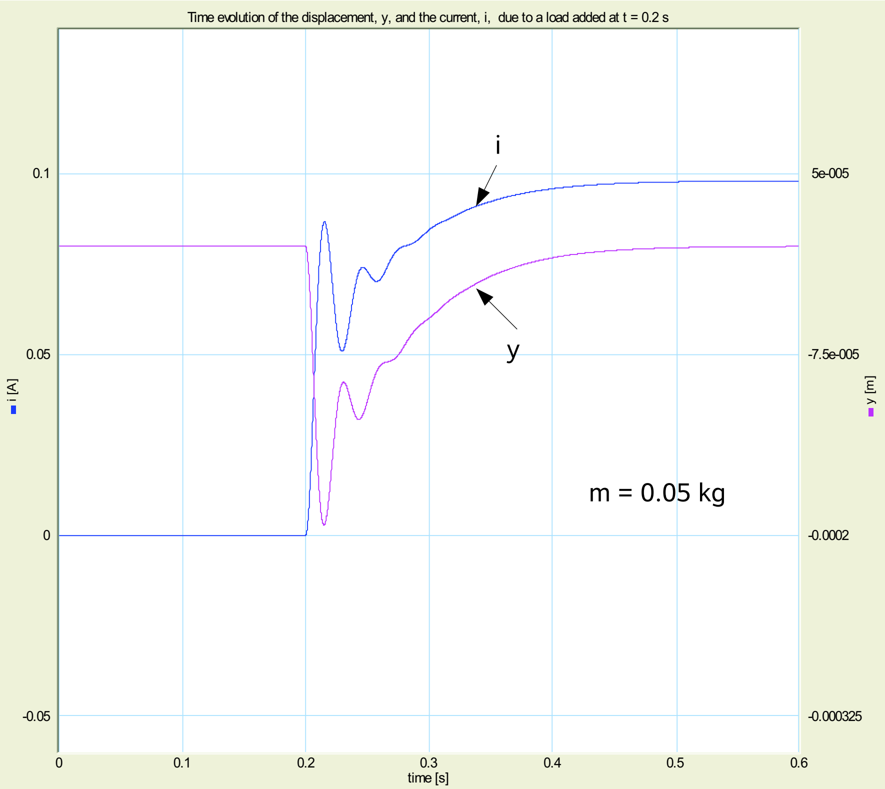

Fig. 12.22 Time evolution of the displacement and the current due to a load added at t = 0.2s

If Equation 12.26 is solved for the vector $[F\, u_p]^t$, then the result can be read as the constitutive relation of a linear energy conservative 2-port C field in integral causality (cf. Figure 12.24). The linear 2-port C field can be decomposed as depicted in Figure 12.25, where $\varDelta := c_p/k_p - d_\varepsilon^2$.

Bond Graph Model of the Piezoelectric Seismometer

In the following, the bond graph of Figure 12.25 is used in the development of a model of a piezoelectric seismometer as sketched in Figure 12.26.

The casing of the piezoelectric seismometer is placed on the ground, or, e.g., on a surface of a machine where vibrations $\dot{u}(t)$ are to be sensed. Inside the case, a piezoelectric crystal is attached to the case. A seismic mass, m, on top of the crystal is fixed to the case by a spring of stiffness k. The piezoelectric crystal reacts to the relative motion, $\dot{y}_r := \dot{y} - \dot{u}$, between the case and the seismic mass. It produces a small current that is fed into an amplifier to be modelled in a third step.

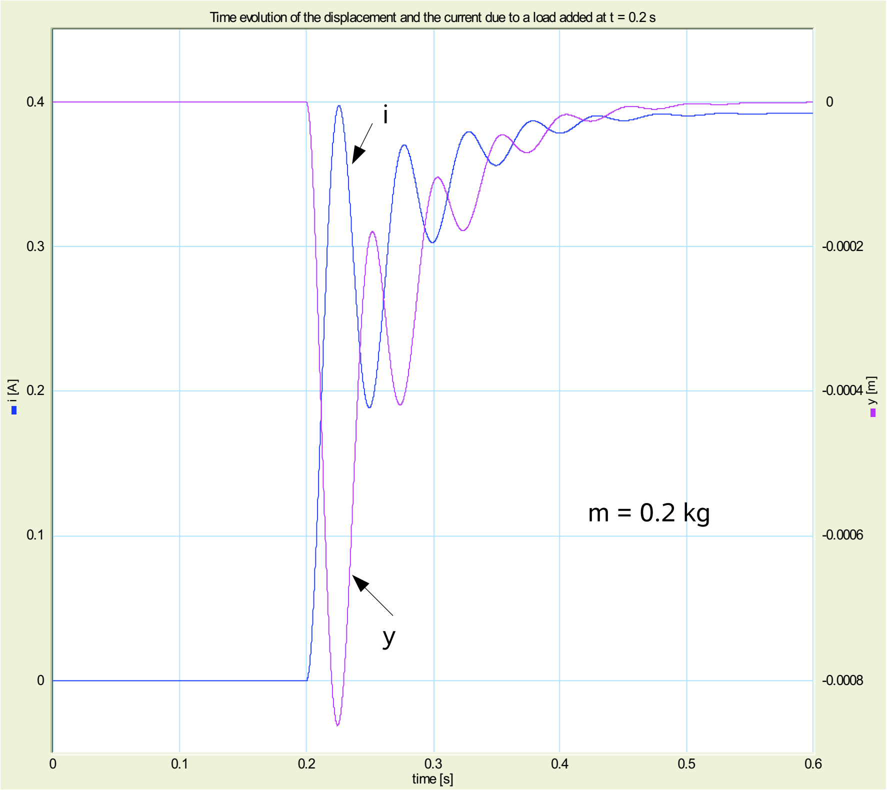

Fig. 12.23 Time evolution of the displacement and the current due to a four times heavier load added at t = 0.2s

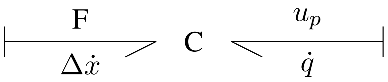

Fig. 12.24 Representation of a piezoelectric crystal by a 2-port C field

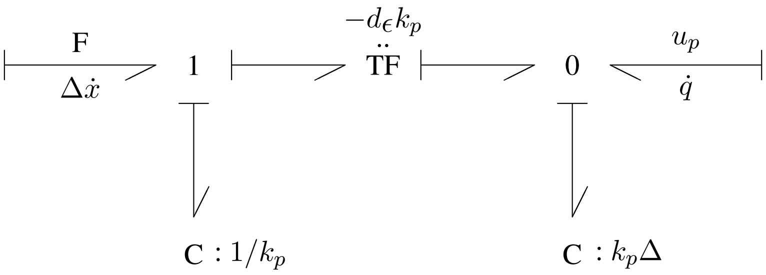

Fig. 12.25 Decomposition of the linear 2-port C field

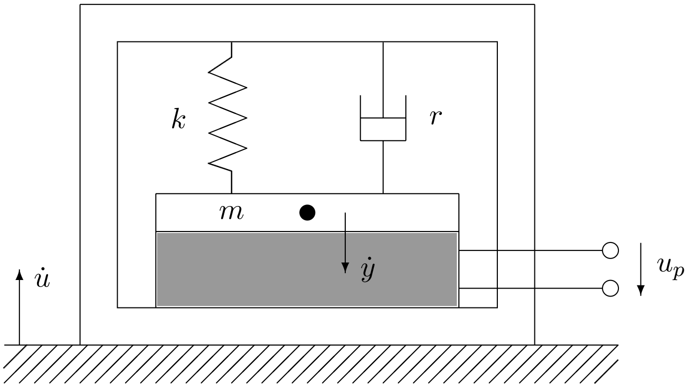

Fig. 12.26 Piezoelectric seismometer

The bond graph modelling of the seismometer is straightforward. The result is depicted in Figure 12.27. Displacements are relative to the position where gravitational force of the seismic load and the spring force of the crystal are in equilibrium.

From the bond graph of Figure 12.27, the following equation of motion is derived for the mechanical part of the piezoelectric sensor.

$$m\ddot{y}_r + r\dot{y}_r + (k + k_p)y_r = -m\ddot{u} - d_\varepsilon k_p u_p \qquad (12.27)$$

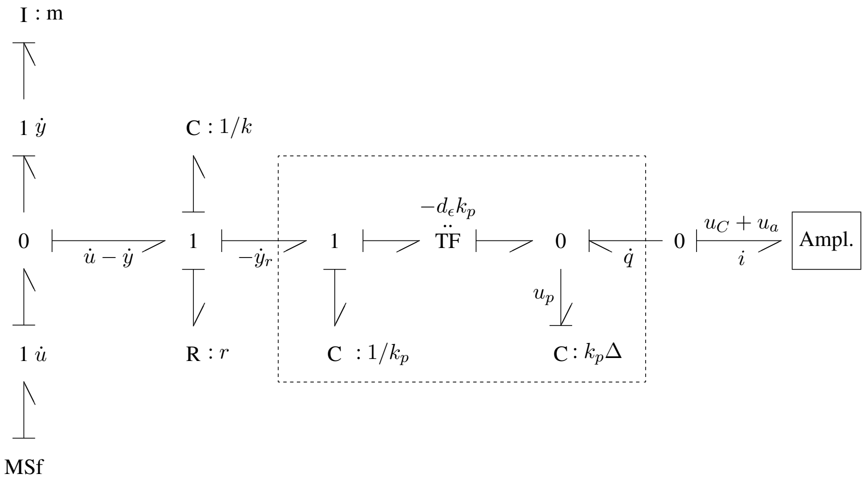

Fig. 12.27 Bond graph of the piezoelectric seismometer

Bond Graph Model of a Charge Amplifier

The current $\dot{q}$, generated by the piezoelectric crystal, is fed into a charge amplifier of which a circuit diagram is shown in Figure 12.28. Figure 12.29 shows a bond graph of the charge amplifier.

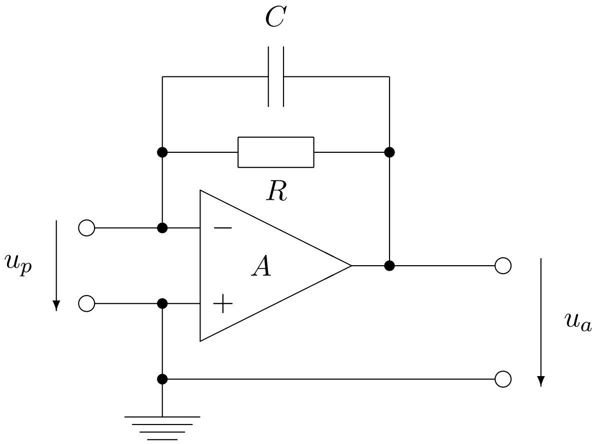

Fig. 12.28 Charge amplifier

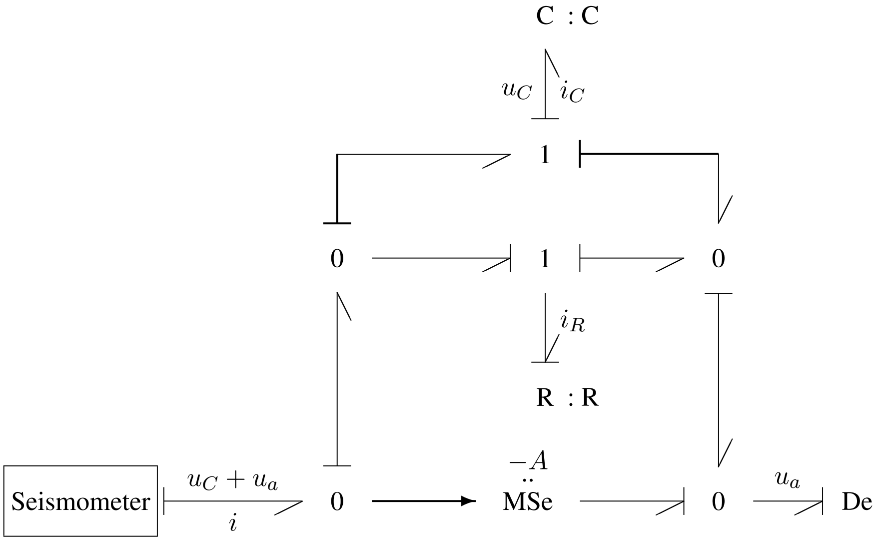

Fig. 12.29 Bond graph of the charge amplifier in Figure 12.28

From the bond graph of Figure 12.29, a relation between the voltage u_a at the amplifier's output and the current $i = -\dot{q}$ into the charge amplifier can be derived.

$$C(1 + \frac{1}{A})\dot{u}_a \; + \; \frac{1}{R}(1 + \frac{1}{A})u_a \; = \; \dot{q} \tag{12.28}$$

For $A \gg 1$, Equation 12.28 reduces to

$$RC\dot{u}_a \; + \; u_a \; = \; R\dot{q} \; . \tag{12.29}$$

Furthermore, the constitutive equation of the modulated voltage source in the bond graph of the amplifier (Figure 12.29) is

$$u_a \; = \; (-A)(u_C + u_a) \; . \tag{12.30}$$

Hence, as $u_p = u_C + u_a$ (cf. Figure 12.27), a high value of the amplification, A, entails a small voltage, u_p, across the electrical terminals of the piezoelectric crystal.

$$u_p \; = \; u_a + \; u_C \; = \; -\frac{1}{A}u_a \approx 0 \tag{12.31}$$

Consequently,

$$-\,\dot{q} \; = \; (-d_\varepsilon k_p)(-\dot{y}_r) \tag{12.32}$$

and

$$m\ddot{y}_r \; + \; r\dot{y}_r \; + \; \underbrace{(k + k_p)}_{k}y_r \; = \; -m\ddot{u} \; . \tag{12.33}$$

Frequency Analysis of the Piezoelectric Seismometer-Amplifier System

Combining the Laplace transforms of Equations 12.29, 12.31, and 12.33 yields the transfer function

$$\begin{aligned} \frac{\mathscr{L}u_a}{\mathscr{L}\ddot{u}} &= \frac{-\dfrac{m}{k}}{\underbrace{\dfrac{m}{k}}_{1/\omega_0^2}\,s^2 + \underbrace{\dfrac{r}{k}}_{2\zeta/\omega_0}\,s + 1}\,(-\underbrace{d_\epsilon k_p}_{T})\,\frac{Rs}{\underbrace{RC}_{\tau}\,s + 1} \\ &= \frac{\dfrac{TR}{\omega_0^2}s}{\left[\left(\dfrac{s}{\omega_0}\right)^2 + \left(\dfrac{2\zeta}{\omega_0}\right)s + 1\right]\,[\tau s + 1]} \; . \end{aligned} \tag{12.34}$$

For a Bode plot of the transfer function (Equation 12.34), the parameters in Table 12.6 have been used (cf. [15]). The frequency domain behaviour of the seismometer-amplifier system is shown in Figure 12.30.

Table 12.6 Parameters of the seismometer-amplifier system

Parameter	Value	Units	Meaning
f_0	10^4	1/s	$\omega_0 = 2\pi f_0$: eigenfrequency of the undamped seismometer
T	10^8	As/m	$T = d_\epsilon k_p$: Transduction coefficient of the piezoelectric crystal
ζ	0.5		Damping coefficient of the seismometer
R	1	Ω	Resistance (cf. Figure 12.28)
τ	5	s	$\tau = R \times C$: Time constant of the amplifier

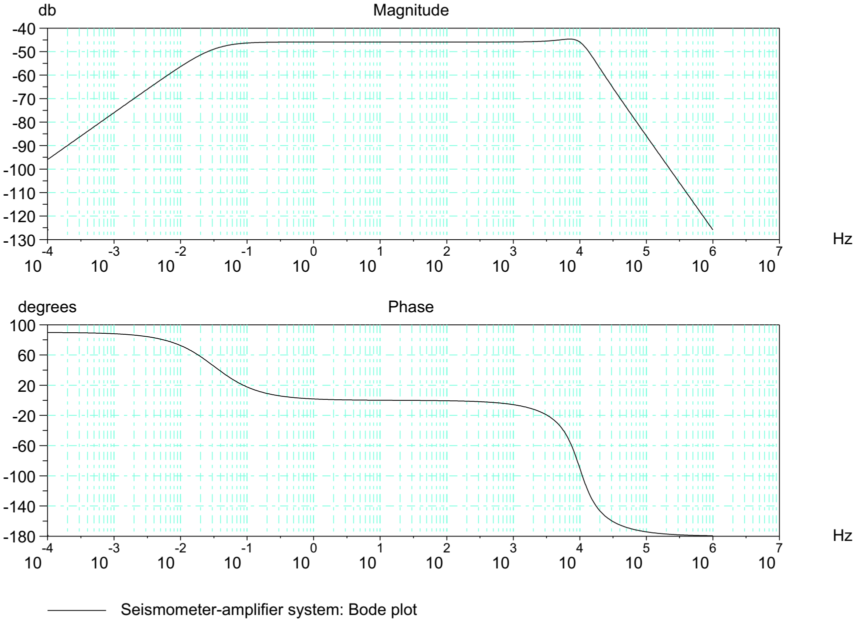

Fig. 12.30 Bode plot of the seismometer-amplifier system

As can be seen from Figure 12.30, the system can sense accelerations of the ground almost up to the eigenfrequency, f_0, of the undamped seismometer. The low frequency behaviour of the system is limited by the high pass filter characteristic of the charge amplifier and its corner frequency $\omega_c = 0.2\ 1/s$.

12.6 Engagement of a Clutch

In Chapter 7, some approaches to a bond graph representation of variable structure models have been discussed. If one wants to keep the structure of the bond graph and the computational causality invariant for all system modes, then one option is

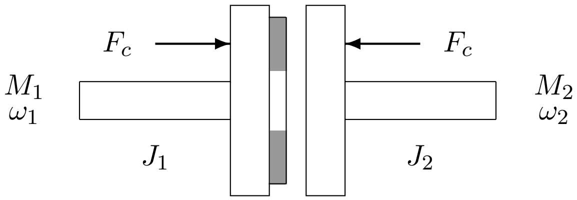

Fig. 12.31 Schematic of a clutch

to use sinks of fixed causality. At the advent of a discrete event, they impose an effort or a flow such that there is an instantaneous state transition and the new state conditions are met (cf. Section 7.1.4). In the following, this approach is used to model the engagement of a clutch. Another option is to model the clutch by an ideal switch of variable causality as has been done by Buisson in [4] (cf. also Section 7.2). In [25], this example has been used for a MATLAB®/Simulink®simulation.

Figure 12.31 shows a schematic of the clutch. Clearly, as long as the clutch is disengaged, the two disks rotate with their own angular velocity. When they get into contact, the two of them encounter a friction moment M_R. This friction moment reduces the angular velocity, ω_1, on the drive side and simultaneously accelerates the power-takeoff side against a possible load moment M_2. If the value of the contact force, F_c, is high enough, then the angular velocities of the disks will converge. At one point in time, they stick together and will continue to rotate as one single body with one and the same angular velocity ω. That is, there are two system modes.

Bond Graph Model of the Clutch

The approach in Section 7.1.4 leads to the bond graph in Figure 12.32.

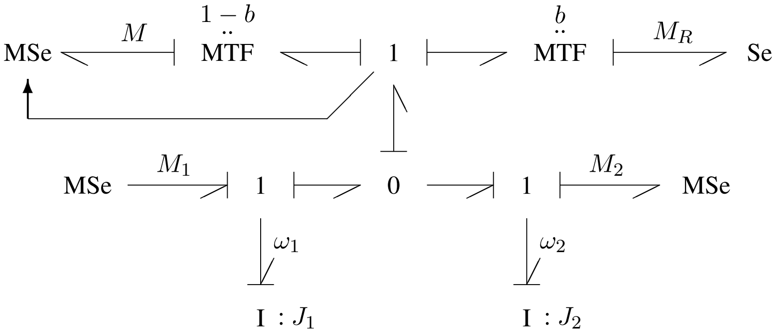

Fig. 12.32 Bond graph of the clutch with invariant structure and invariant computational causality

In the bond graph of Figure 12.32, M_1 and M_2 denote the moment on the drive side and the load moment on the power-takeoff side respectively. According to Section 7.1.2, switches have been modelled by modulated transformers. As long as there is a difference between the two angular velocities on the drive side and on the power-takeoff side, the modulus b equals 1 and both rotating disks encounter a friction moment, M_R, proportional to the contact force F_c. As in [25], it is assumed that the initial angular velocity of the engine is $\omega_{10} = 200\ rad/s$, while the transmission side starts from $\omega_{20} = 0\ rad/sec$. When the increasing angular velocity ω_2 equals ω_1, then the two disks stick together and the modulus b of the right-hand side MTF is set to zero. Consequently, the upper left part of the bond graph becomes active. It provides a moment M that ensures that the two disks stick together and rotate with one and the same angular velocity ω. Note that in both system modes, the two inertia elements are invariantly in integral causality. However, when the two disks rotate with a common angular velocity, the set of equations is a DAE system as there is no differential equation for the moment, M, ensuring that the angular velocity difference remains zero.

Simulation of the Clutch Behaviour

Given the parameter values in Table 12.7 [25], simulation (by means of Scilab) yields the time evolution of the angular velocities depicted in Figure 12.33.

Analytical Evaluation of the Clutch Model

Due to the simplifying assumptions, the problem can also be analytically solved. Hence, essential values obtained by simulation can be checked. For $\omega_2 < \omega_1$ $(b = 1)$, the following two equations for the inertia elements are easily derived from the bond graph.

$$\dot{\omega_1} = \frac{1}{J_1}(M_1 - M_R) \tag{12.35a}$$

$$\dot{\omega_2} = \frac{1}{J_2}(M_R - M_2) \tag{12.35b}$$

Table 12.7 Parameter values used for simulation of the clutch engagement

Parameter	Value	Units	Meaning
M_1	200	Nm	Driving torque
M_2	0	Nm	Load moment
J_1	1	kgm^2	Moment of inertia on the drive side
J_2	5	kgm^2	Moment of inertia on the power-takeoff side
F_c	5000	N	Contact force
k	0.38	m	$M_R = k \times F_c$
$\omega_1(0)$	200	rad/s	Initial angular velocity on the drive side
$\omega_2(0)$	0	rad/s	Initial angular velocity on the transmission side

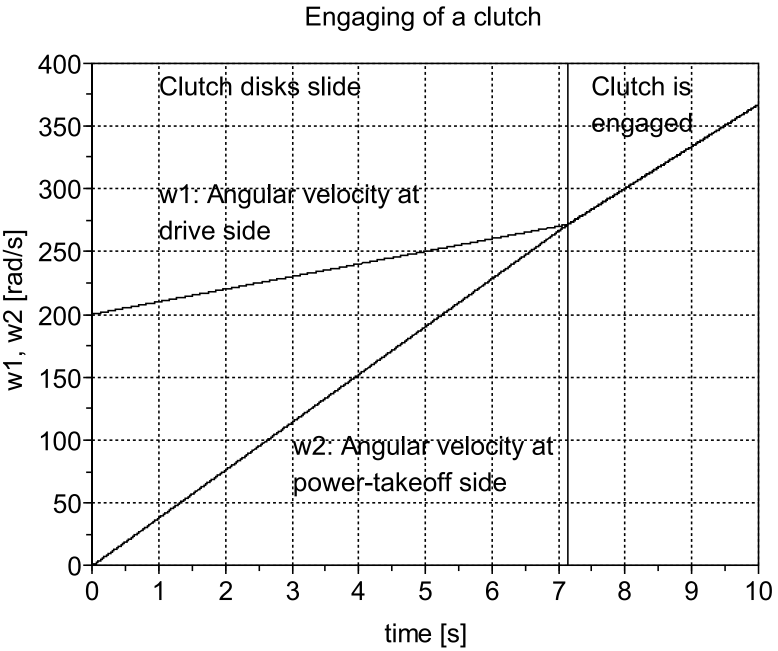

Fig. 12.33 Angular velocities of the clutch disks

Their integration yields

$$\omega_1(t) = \frac{M_1 - M_R}{J_1}\, t \, + \, \omega_{10} \tag{12.36a}$$

$$\omega_2(t) = \frac{M_R - M_2}{J_2}\, t \, + \, \omega_{20} \; . \tag{12.36b}$$

If the value of the contact force, F_c, is sufficiently high, the clutch disks stick together at some time point $t = t_1$ and continue to rotate with one and the same angular velocity ω. Equality of both angular velocities gives for t_1

$$t_1 \; = \; \frac{\omega_{10} - \omega_{20}}{\dfrac{M_2 - M_R}{J_2} + \dfrac{M_R - M_1}{J_1}} \; . \tag{12.37}$$

The parameter values in Table 12.7 result in the value $t_1 = 7.143\ s$. The value of the common angular velocity is $\omega = 271.43\ rad/s$. For $t > t_1$, the angular acceleration $\dot{\omega}$ reads

$$\dot{\omega} \; = \; \frac{M_1}{J_1 + J_2} \; . \tag{12.38}$$

The numerical value is $\dot{\omega} = 33.3\, rad/s^2$.

For $t > t_1$ ($b = 0$), the DAE system derived from the bond graph reads

$$\dot{\omega}_1 = \frac{1}{J_1}(M_1 - M) \tag{12.39a}$$

$$\dot{\omega}_2 = \frac{1}{J_2}(M - M_2) \tag{12.39b}$$

$$0 = \omega_1 - \omega_2 \,. \tag{12.39c}$$

After differentiation of the algebraic constraint with respect to time, solution of the resulting ODE system yields for the moment M

$$M = \frac{J_2}{J_1 + J_2} M_1 + \frac{J_1}{J_1 + J_2} M_2 \,. \tag{12.40}$$

Given the parameter values in Table 12.7, the value is $M = 166.7\,Nm$. Hence, for $t \geq t_1$, the descriptor vector, $[\omega_1, \omega_2, M]^t$, has the initial conditions $[271.43, 271.43, 166.7]^T$. Location of the time point t_1 and continuation of the simulation with the correct initial conditions can be performed by the root finding version of the widely used numerical integration codes DASSL [2] or ODEPACK [14]. These solvers are part of, for instance, the open source mathematical software package Scilab [26].

12.7 Dry Friction in a Suspension Strut of a Car

Another example in which different system modes can be distinguished is the stick-slip effect in a suspension strut of a car. For the analysis of this effect, the widely used simple quarter vehicle model depicted in Figure 12.34 is considered.

As long as there is slip friction effective in the strut, the mass of the chassis, m_c, and the mass of the wheel, m_w, move up and down with different displacements x_c and x_w. If stick friction is effective, there is a holonomic constraint

$$x_w - x_c = \text{const.} \tag{12.41}$$

and the view can be taken that one body with the combined mass is moving up and down. In this mode, one degree of freedom has gone. Once the break value F_H of the sticking force has been overcome, the system returns into the slip mode and the suppressed degree of freedom is available again. In [18], Kölsch and Ostermeyer account for the sticking mode and the switching between slip and sticking mode by a modification of the constraint force between two bodies in the equations of motion.

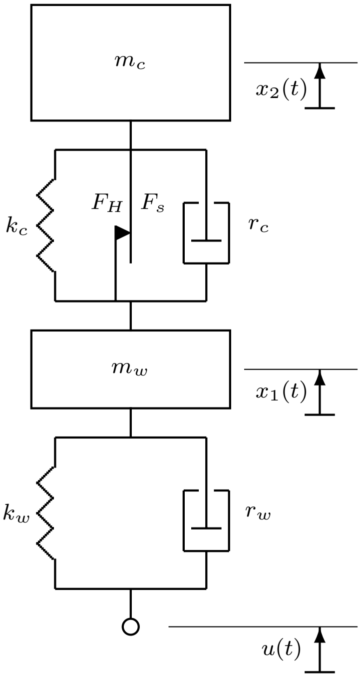

Fig. 12.34 Schematic of a quarter vehicle

Bond Graph Model of the Quarter Vehicle Accounting for Stick-Slip Friction

In the following, the more general bond graph approach using sinks of fixed computational causality described in Section 7.1.4 is applied.

Figure 12.35 shows a bond graph of the quarter vehicle accounting for the slip and the sticking mode. In the bond graph model of Figure 12.35, the modulated effort sink provides the constraint force λ. The value of the transformer modulus b accounts for the system mode. For $b = 1$, the sticking force F_{stick} is enabled and, simultaneously, the slip friction force F_{slip} is disabled and vice versa for $b = 0$. That is, according to the system mode, one part of the bond graph model is switched on and another one is switched off. Note that computational causalities remain fixed independent of the system mode.

Derivation of Model Equations from the Bond Graph

The mathematical model to be derived from the bond graph depends on the system mode. For the slip mode, it is a set of explicit ODEs. For the sticking mode, it is a DAE system of index 2 that can analytically reduced to an explicit ODE system

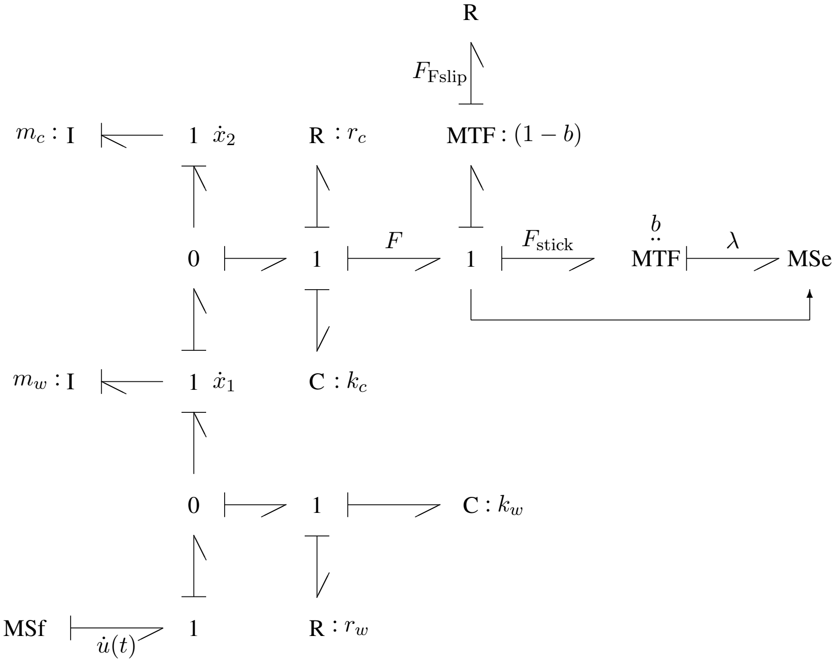

Fig. 12.35 Bond graph of the quarter vehicle accounting for the slip and the sticking mode

different from the one for the slip mode. Clearly, the control logic that switches the value of the transformer modulus b cannot be part of the bond graph and has to be formulated separately. The modulated flow source on the lower left-hand side of the bond graph models the unevenness of the road surface.

Following causal paths, the two equations of motion can be derived directly from the bond graph.

$$\begin{aligned} m_w \ddot{x}_1 &= r_w(\dot{u} - \dot{x}_1) + k_w(u - x_1) - r_c(\dot{x}_1 - \dot{x}_2) - k_c(x_1 - x_2) \\ &\quad -(1-b)\,F_{\mathrm{slip}} - b\,\lambda \qquad (12.42a) \\ m_c \ddot{x}_2 &= r_c(\dot{x}_1 - \dot{x}_2) + k_c(x_1 - x_2) + (1-b)F_{\mathrm{slip}} + b\,\lambda \qquad (12.42b) \end{aligned}$$

For $b = 1$, the two equations of motion together with the constraint for the displacement of the two bodies constitute a DAE system of index 2 for the unknowns x_1, x_2, λ.

In order to obtain an expression for the constraint force λ, the constraint, Equation 12.41, is differentiated twice with respect to time. After substitution of the equations of motion, the result is

$$\lambda = k_c(x_2 - x_1) + r_c(\dot{x}_2 - \dot{x}_1) - k_w \frac{m_c}{m_w + m_c}(x_1 - u) - r_c \frac{m_c}{m_w + m_c}(\dot{x}_1 - \dot{u}) \; . \tag{12.43}$$

In slip mode ($b = 0$), the friction force F is

$$F = F_{\text{slip}} = F_s \, \text{sign}(v_1 - v_2) \; . \tag{12.44}$$

Simulation of the Stick-Slip Problem Using Scilab and LSODAR

Computation of this hybrid model requires the location of times at which the system mode changes from sliding to sticking or vice versa. This suggests the use of the root finding version of an ODE solver. For this case study, Scilab and the ODE solver LSODAR have been used.

Formulation of the model equations as a Scilab function is straightforward. The result is shown in Figure 12.36. The Scilab function `f` is an argument of the Scilab function `ode` which is an interface to the ODE solvers in the software package ODEPACK.

```
// Scilab function of a quarter vehicle
// Suspension with dry friction

function [dy] = f(t,y)

v1     = y(1)
v2     = y(2)
x1     = y(3) // vertical position of the chassis
x2     = y(4) // vertical position of the wheel

u      = ramp(t,t0,t1,u1) // unevenness of the road surface
du     = pulse(t,t0,t1)

Fslip  = Fs*sign(v2 - v1)

lambda = kc*(x2 - x1) + rc*(v2 - v1) - c1*(x1 - u) - c2*(v1 - du)

mwdv1  = -(rw + rc)*v1 + rc*v2 - (kw + kc)*x1 + kc*x2 + kw*u + rw*du
         + (1-b)*Fslip - b*lambda
dv1    = mwdv1 / mw

mcdv2  = rc*v1 - rc*v2 + kc*x1 - kc*x2 - (1-b)*Fslip + b*lambda
dv2    = mcdv2 / mc

dy1    = dv1
dy2    = dv2
dy3    = v1
dy4    = v2

dy     = [dy1;dy2;dy3;dy4]

endfunction
```

Fig. 12.36 Equations of the quarter vehicle model as a Scilab function

Figure 12.37 shows the Scilab script for a simulation run on the quarter vehicle model. In the Scilab script of Figure 12.37, the meaning of variables has been explained by inline comments. The root finding capability of the ODE solver is used to locate the time points t_c at which the system mode may change from sticking to slipping or vice versa. If the current mode is sticking ($b = 1$), then integration is performed up to a time point for which $|\lambda| - F_H = 0$ holds. Otherwise, if the current mode is sliding ($b = 0$), then integration stops at a time point for which $v_1 = v_2$. Both conditions are formulated in the function `g`. If such a time point t_c has been located, it must be checked if the conditions for a change in the system mode are met. If the current mode is sticking and the absolute value of the constraint force reaches the breakaway level, F_H, of the friction force F, then both bodies can slip. On the contrary, if both bodies slide with a common velocity, then there is potential risk for sticking. Both bodies will stick if the absolute value of lambda falls below the slip level, F_s, of the friction force F. The system mode is taken into account by the value of the modulus b, which must be changed appropriately. This is done in the function `change` depicted in Figure 12.38. In this manner, integration proceeds from one discrete event to the next until the final simulation time has been reached.

For simulation runs, parameter values given in [18] have been used (Table 12.8). As to the velocity excitation of the road, $\dot{u}(t)$, it is assumed that the quarter vehicle moves up a ramp (Figure 12.39). Furthermore, it is assumed that the strut is in stiction mode at $t = 0$. The initial conditions for the simulation run are

$$v_1(0) = v_2(0) = 0 \tag{12.45}$$

and

$$x_1(0) = x_2(0) = 0\,. \tag{12.46}$$

The simulation result in Figure 12.40 shows that immediately after the start, the system changes from initial sticking into the slipping mode, which lasts until about $1.43\,s$. During this period, there are two short time intervals in which sticking occurs. As can be seen from Figure 12.40, in fact, the difference between the vertical velocities of the wheel, v_1, and of the chassis, v_2, vanishes during the sticking periods. Figure 12.41 shows the time history of the vertical displacements of the wheel, x_1, and of the chassis (x_2). According to Figure 12.40, for $t > 1.43\,s$, the wheel

Table 12.8 Parameter values used for simulation of the quarter vehicle

Parameter	Value	Units	Meaning
m_w	100	kg	Mass of the wheel
r_w	126	Ns/m	Damping coefficient for the tyre
k_w	395×10^3	N/m	Stiffness of the tyre
r_c	1500	Ns/m	Damping coefficient of the suspension
k_c	39.5×10^3	N/m	Stiffness of the suspension
F_H	500	N	Breakaway level of the friction force F
F_s	500	N	Slip level of the friction force F
m_c	1000	kg	Mass of the chassis

```
// run quarter vehicle model

%ODEOPTIONS=[2,0,0,%inf,0,2,1000,12,5,0,-1,-1];
tf  = 5.0; // [sec] tf: final time of the integration
ng  = 1;
b   = 1;   // inital mode is sticking
//
// 'root': LSODAR from ODEPACK is called
// x0: vector of initial conditions
// t0: initial start time
// f:  right-hand side of the set of ODEs: ydot = f(t,y)
// g:  integration of ydot = f(t,y) is performed
//     until g(t,y) = 0 holds for one component of y
// rd(1): time at which integration stops
// sol: matrix, each row >= 2 contains a component of y at times <= rd(1)
//
[sol,rd] = ode('root',x0,t0,tf,f,ng,g);
m   = size(sol); // m(2): number of columns
tc  = rd(1);
//
bvector=b*ones(1,m(2)); // contains system mode at times <= tc
//
// check if the system mode changes at tc:
//
b = change(sol);
//
// continue the integration as long as tc <= tf:
//
while tc <= tf
//
// use values at tc as new initial conditions xc:
//
xc  = [sol(2,m(2));sol(3,m(2));sol(4,m(2));sol(5,m(2))];
//
// continue the integration until the solution crosses
// the surface g(t,y) = 0:
//
[xsol2,rd2] = ode('root', xc,tc,tf,f,ng,g);
//
m2 = size(xsol2);
bvector2 = b*ones(1,m2(2));
bvector = [bvector,bvector2];
//
sol = [sol,xsol2];
m   = size(sol);
tc = rd2(1);
//
// check if the system mode changes at tc:
//
b = change(sol);
```

Fig. 12.37 Scilab script for a simulation run on the quarter vehicle model

```
// Function change() is called at time point tc
// at which integration has stopped because the conditions
// specified in function g() are met.
// According to the result of the check below function change()
// returns an update of the system mode indicator b used in the
// script that calls change().
// Fs: slip level of the friction force F

function [b] = change(sol)
  v1 = sol(2,m(2))
  v2 = sol(3,m(2))
  x1 = sol(4,m(2))
  x2 = sol(5,m(2))

  u  = ramp(tc,t0,t1,u1)
  du = pulse(tc,t0,t1)

  lambda = kc*(x2 - x1) + rc*(v2 - v1) - c1*(x1 - u) - c2*(v1 - du)

  mode = b; // current system mode
  if (mode == 0 & abs(lambda) <= Fs) then b = 1; end
  if mode == 1 then b = 0; end

endfunction
```

Fig. 12.38 Function `change` changing the system mode indicator b appropriately

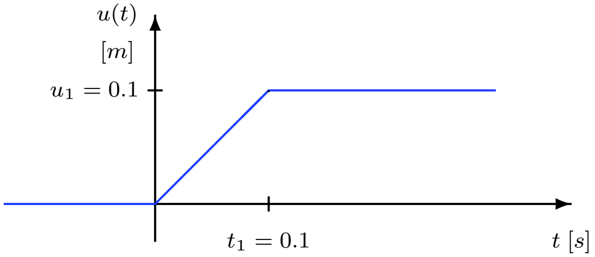

Fig. 12.39 Roadway unevenness u over time

and the chassis stick together and oscillate with a common frequency of about 3 Hz and a very small amplitude up and down. This oscillation is lightly damped because of the low damping coefficient of the tyre.

Finally, Figure 12.42 displays the time evolution of the constraint force λ and of the slip friction force $F_{\text{slip}} = F_s\,\text{sign}(v_1 - v_2)$. The simulation results presented in this case study agree with those given in [18].

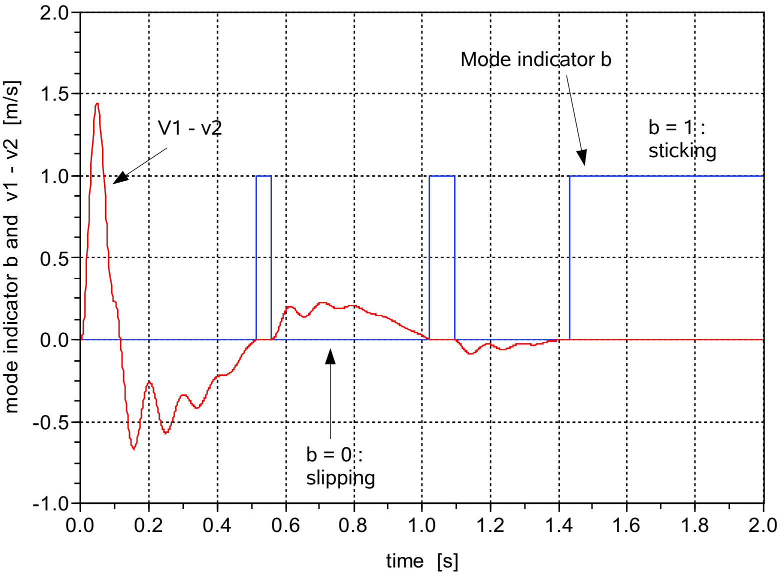

Fig. 12.40 System mode indicator b and relative velocity between wheel and chassis

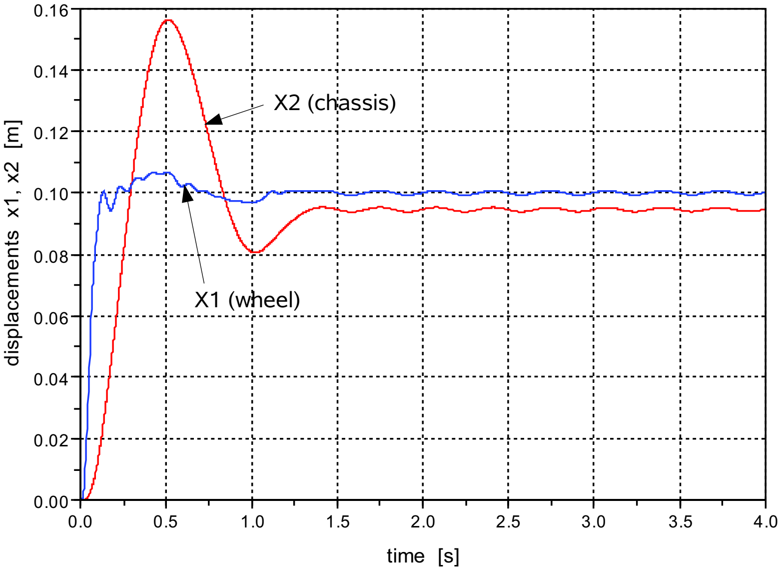

Fig. 12.41 Vertical displacements of the wheel and of the chassis

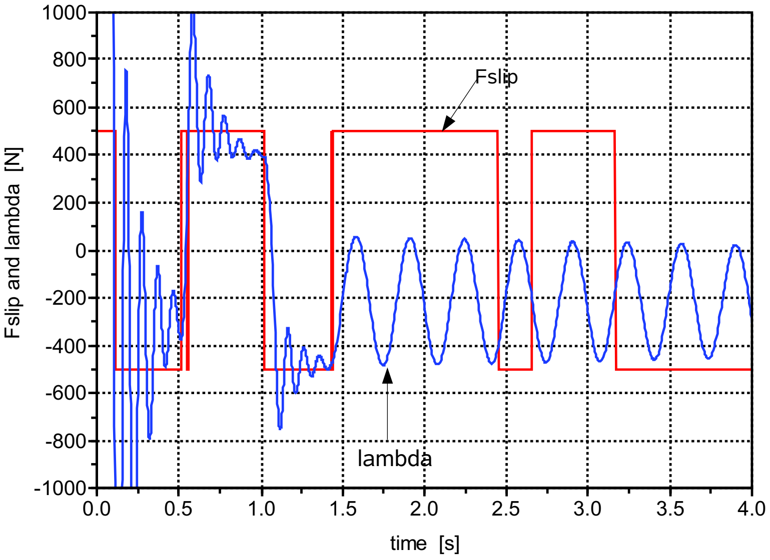

Fig. 12.42 Constraint force λ and slip friction force F_{slip}

12.8 A Buck Converter

Chapter 7 discusses several approaches to a representation of variable structure models. As bond graphs are based on the energy exchange between system components taking place in time periods not equal to zero, they are best suited for continuous time models. Accordingly, Section 7.3 proposes to describe discrete system states and transitions between them by a Petri net and to develop a bond graph model for each system mode. For illustration of this approach and in order to apply bond graph modelling to an electronic circuit beyond passive RLC networks, a DC-DC buck converter as displayed in Fig 12.43 is studied.

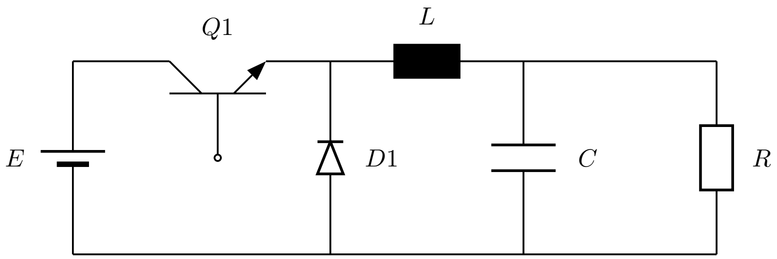

Fig. 12.43 Schematic of a buck converter

A DC-DC buck converter is a well known power electronic device [5]. Its purpose is to reduce a DC input voltage. The use of switching elements enables one to reduce the energy consumption in comparison to linear regulators. Due to its function and the use of switching elements, it is also called step-down switch mode power supply. As the device is superior to linear voltage regulators, they are used in applications where size and power dissipation matters, e.g. for the low voltage power supply of processors in laptop computers, or in rechargers.

In the context of bond graph modelling of power electronic circuits, buck converters have been considered by several authors [1, 10, 11, 20]. The transistor $Q1$ and the diode D are usually modelled as switches with an ON-resistance. In [10, 11], Garcia-Gomez uses a unique bond graph model for all switch modes and represents the switches by means of a modulated transformer and a resistor (cf. Figure 7.6, Section 7.1.2).

System Modes of the Buck Converter

If the transistor and the diode are considered as switches, theoretically, four system modes as listed in Table 12.9 can be distinguished.

When the transistor switch is in ON state (closed), a current is flowing through the inductor into the load composed of the resistor R and the capacitor C in parallel, and the inductor stores energy as highlighted in Figure 12.44. In this system mode, the diode (displayed in grey in Figure 12.44) is off because it is reverse biased. This system mode is known as load state.

Table 12.9 Theoretical switch state combinations

System mode	Transistor	Diode
1	ON	OFF
2	OFF	ON
3	ON	ON
4	OFF	OFF

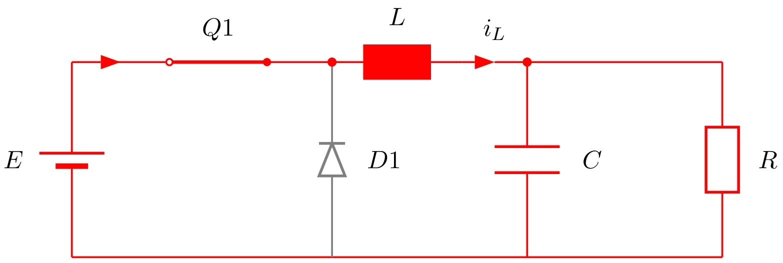

Fig. 12.44 Buck converter in mode 1 (transistor switch on and diode off)

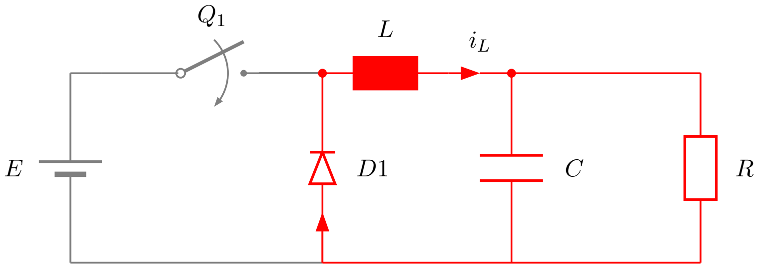

Fig. 12.45 Buck converter in mode 2 (transistor switch off and diode on)

In system mode 2, the transistor switch is off (Figure 12.45). The diode is forward biased and the energy stored in the inductor discharges into the load. This mode is called free wheel mode.

If the ON resistance of both switches is neglected, then the third switch state combination (both switches are closed) would entail a short-circuit of the voltage source and consequently a disfunction of the circuit. That is, this switch state combination can be discarded. This is reflected by a causal conflict in the bond graph of Figure 12.46.

In the fourth system mode (both switches are off), the current through the coil has become zero and the coil does not store any magnetic energy. While the inductor remains empty, the energy of the capacitor discharges via the load resistor (Figure 12.47). In the literature, this state is sometimes called the rest state. In Figure 12.47, there is no current in the part of the circuit displayed in grey. In the following, it is assumed that the transistor is switched on and off periodically and that there are no time periods in which the current through the inductor remains zeros. In this case, the buck converter is said to operate in continuous mode. Accordingly, the circuit toggles between the two system modes 1 and 2. This is captured in the simple Petri net of Figure 12.48. In the Petri net, T denotes the duty cycle of the

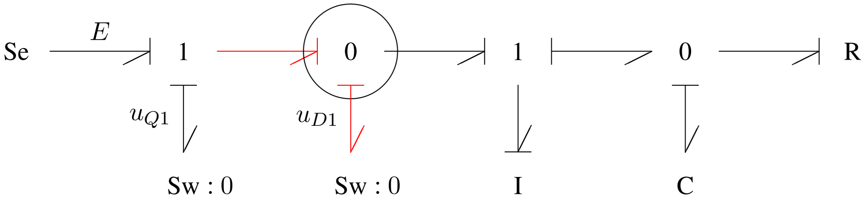

Fig. 12.46 Bond graph of the buck converter in case both switches are on

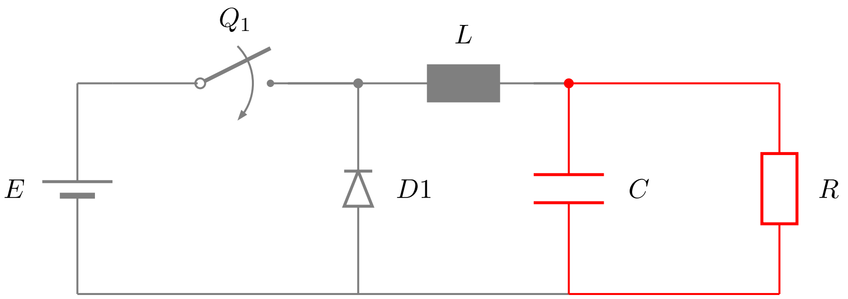

Fig. 12.47 Buck converter in mode 4 (both switches off)

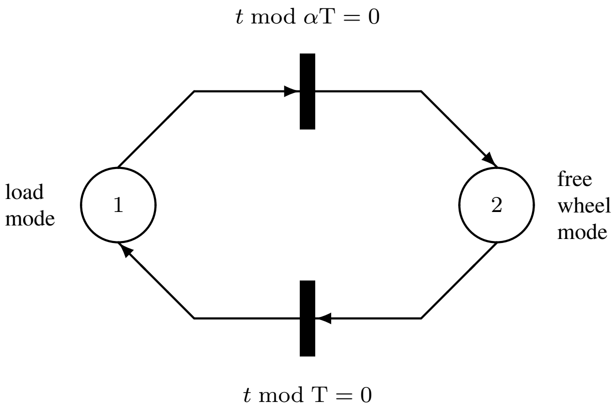

Fig. 12.48 Petri net for a periodically switched buck converter

signal switching the transistor on and off. The transistor is on for the period αT $(0 < \alpha < 1)$, while it is off during the period $(1 - \alpha) T$ (Figure 12.49).

Bond Graph Models of the Buck Converter in Load Mode and in Free Wheel Mode

For both system modes, the construction of a bond graph is straightforward. Figures 12.50 and 12.51 show the results.

A straightforward way to simulate the behaviour of the buck converter is to alternate between the computation of the two models. For the buck converter under study, a look at the equations derived from the bond graph models shows that both models can be combined into one unique bond graph displayed in Figure 12.52. In the bond graph of Figure 12.52, the transformer modulus m is the OnOff-function

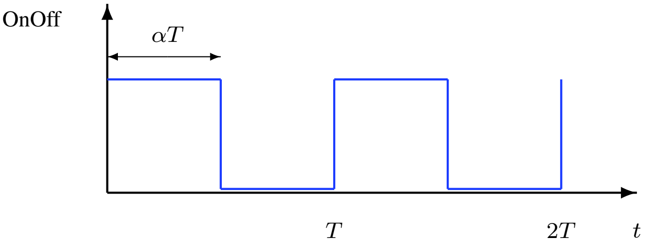

Fig. 12.49 Signal switching the transistor on and off

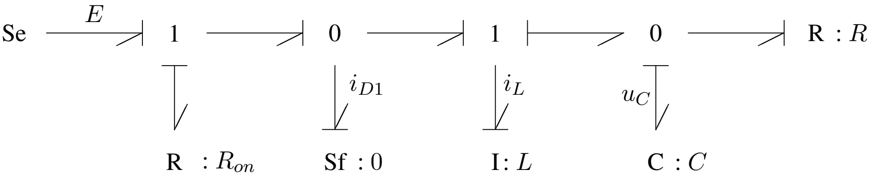

Fig. 12.50 Bond graph of the buck converter in load mode

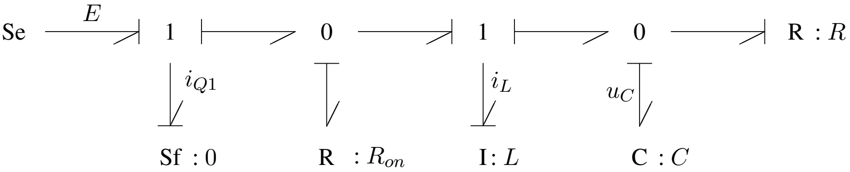

Fig. 12.51 Bond graph of the buck converter in free wheel mode

in Figure 12.49. This modulus toggles the computation between the sets of model equations for the two system modes.

Simulation of the Buck Converter Dynamic Behaviour

The simulation study uses the parameters listed in Table 12.10. Figure 12.53 displays the time evolution of the current, i_L, through the inductor as well as its mean value $\bar{i}_L$ over one duty cycle. Accordingly, Figure 12.54 shows the time evolution of the voltage drop, u_C, across the capacitor as well as its mean value $\bar{u}_C$.

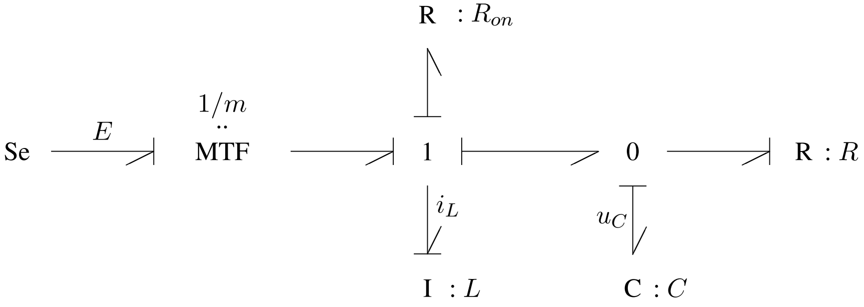

Fig. 12.52 Unique bond graph of the buck converter for system modes 1 and 2

Table 12.10 Parameters used in the simulation study

Parameter	Value	Units
E	100	V
R_{on}	0.1	Ω
L	50	mH
C	50	μF
R	50	Ω
T	10^{-3}	s
α	0.7	-

Verification of Simulation Results

As the circuit under study is rather simple, simulation results can be checked against analytical results. From the bond graph of Figure 12.52, the following two state equations can be derived.

$$\frac{di_L}{dt} = \frac{1}{L}\left[m\,E - R_{on}\,i_L - u_C\right] \tag{12.47a}$$

$$\dot{u}_C = \frac{1}{C}\left[i_L - \frac{1}{R}u_C\right] \tag{12.47b}$$

If the ON resistance R_{on} is neglected and if mE is replaced by the mean value αE, then for $t \rightarrow \infty$, the voltage drop across the capacitor takes the value

$$\bar{u}_C \;=\; \alpha E \;=\; 0.7 \times 100\;V = 70\;V\;. \tag{12.48}$$

Accordingly, for $t \rightarrow \infty$, the current through the inductor takes the value

$$\bar{i}_L \;=\; \frac{1}{R}\bar{u}_C \;=\; \frac{1}{50}70\;A = 1.4\;A\;. \tag{12.49}$$

The mean values ($t \rightarrow \infty$) obtained from simulation are in good agreement with these values.

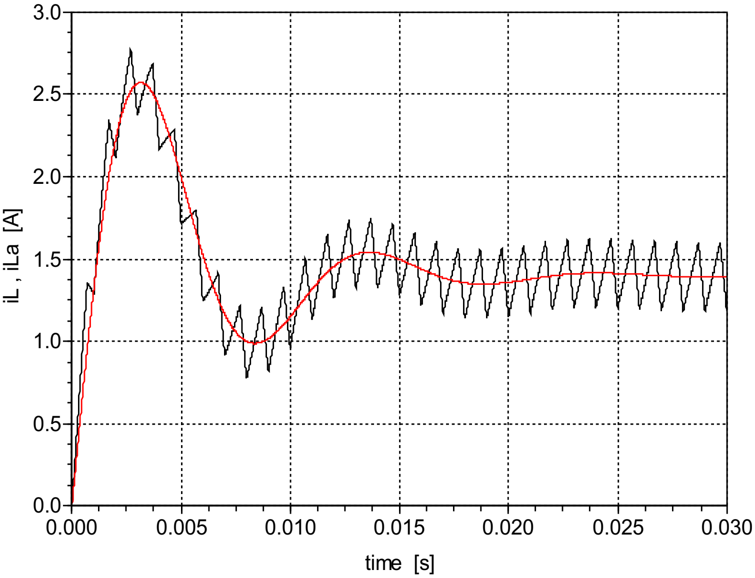

Fig. 12.53 Time evolution of the current through the inductor

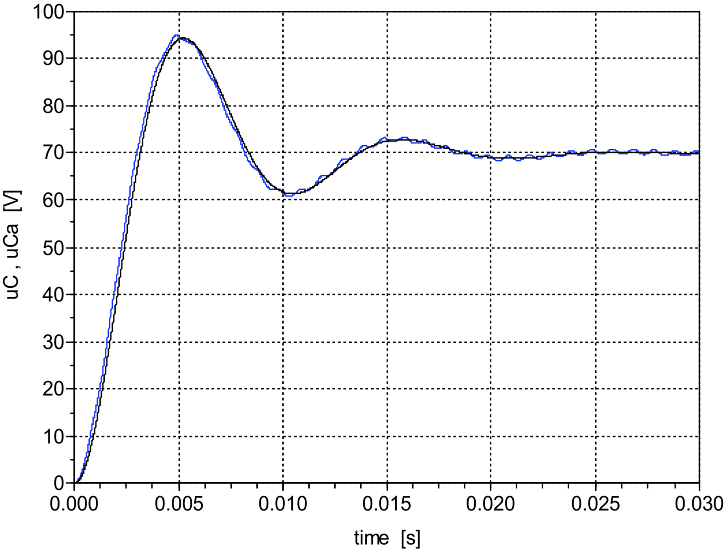

Fig. 12.54 Time evolution of the voltage drop across the capacitor

Furthermore, as Figure 12.53 shows, there is a significant ripple on the waveform of the inductor current. If the ON resistance of the switches is neglected and if the voltage across the capacitor is replaced by the mean value αE, then Equation 12.47a reads

$$\frac{di_L}{dt} = \frac{1}{L}[mE - \alpha E] = \frac{m-\alpha}{L}E \, . \tag{12.50}$$

That is, when the circuit is in load state ($m = 1$), the current through the inductor rises linearly while it falls linearly in the free wheel state ($m = 0$). For $m = 1$, the value of the slope is

$$\frac{di_L}{dt} = \frac{1.0 - 0.7}{50 \times 10^{-3}} \times 100 \; A/s = 600 \; A/s \, . \tag{12.51}$$

For $m = 0$, the inclination is

$$\frac{di_L}{dt} = \frac{-0.7}{50 \times 10^{-3}} \times 100 A/s = -1400 \; A/s \, . \tag{12.52}$$

As can be seen from an enlargement of the ripple depicted in Figure 12.55, simulation results agree well with these values.

According to [24], the amplitude $\Delta I/2$ of the ripple on the waveform of the inductor current i_L is

$$\Delta I = \frac{\alpha \, E(1-\alpha)}{L} T \, . \tag{12.53}$$

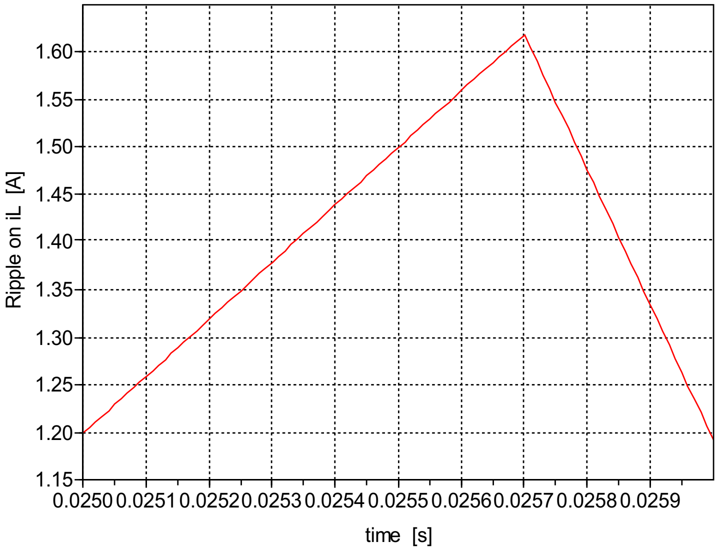

Fig. 12.55 Enlargement of the ripple on the waveform of the inductor current

With the parameters in this case study, the amplitude is 0.21 A. As the mean value is 1.4, values of the ripple should be within the range

$$1.19\ A = (1.40 - 0.21)\ A \leq i_L \leq (1.40 + 0.21)\ A = 1.61\ A\ .$$

This can be verified by inspection of Figure 12.55.

The amplitude $\Delta V/2$ of the ripple on the waveform of u_C is

$$\Delta V \ = \ \frac{\Delta I}{8C} \times T \tag{12.54}$$

[24]. The parameters in this case study give the result $\Delta V = 1.05\ V$. The enlargement of the ripple on the waveform of u_C well confirms this value (Figure 12.56). The ripple on the waveform of u_C oscillates around the mean value of $70\ V$ with an amplitude of about $0.5\ V$.

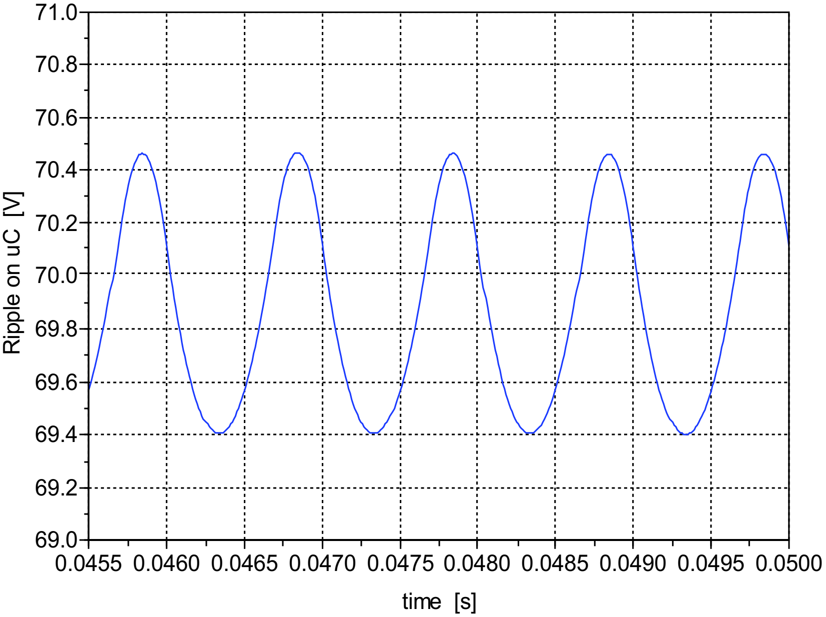

Fig. 12.56 Enlargement of the ripple on the waveform of the voltage drop across the capacitor

12.9 A Two Degrees of Freedom Rotary Joint Manipulator

The concise representation of multibond graphs supports the systematic development of bond graph models of multibody systems. Library models of a freely moving rigid body with hinges and various types of joints can be assembled in the same way the bodies and the joints of the real system are connected. What needs to be taken into account are transformations between body fixed reference frames represented by multiport transformers in a multibond graph.

For illustration, a multibond graph of a part of the Stanford arm has been given in Chapter 8). In the following, it is assumed that the prismatic joint is locked, resulting in a simpler rotary joint manipulator with two degrees of freedom. Figure 12.57 depicts a schematic of this manipulator which may be considered a part of the industrial PUMA robot.

As can be seen from Figure 12.57, body 1 simply rotates on its y_1 axis, while body 2 moves in three dimensions by rotation on an axis through point A that is parallel to the z_1 axis. This axis in turn rotates around the y_1 axis. This type of manipulator has also been considered by Gawthrop and Smith in [13] and by Vergé and Jaume in [29]. In this case study it is shown that the standard form of robot equations [8]

$$\mathbf{M}(\boldsymbol{\Theta})\ddot{\boldsymbol{\Theta}} + \mathbf{V}(\boldsymbol{\Theta}, \dot{\boldsymbol{\Theta}}) + \mathbf{G}(\boldsymbol{\Theta}) = \boldsymbol{\tau} , \tag{12.55}$$

can be directly derived from the multibond graph of the robot in all derivative causality. In Equation 12.55, the vectors $\boldsymbol{\Theta}$, $\dot{\boldsymbol{\Theta}}$, $\ddot{\boldsymbol{\Theta}}$ denote the position, the velocity, and the accelerations of the joints. $\mathbf{M}(\boldsymbol{\Theta})$ is the $n \times n$ mass matrix, $\mathbf{V}(\boldsymbol{\Theta}, \dot{\boldsymbol{\Theta}})$ the $n \times 1$ vector of centrifugal and Corriolis terms, and $\mathbf{G}(\boldsymbol{\Theta})$ is an $n \times 1$ vector of gravity terms. Torques are combined into the vector $\boldsymbol{\tau}$.

In this study, the Lagrange equations have been manually derived from the multibond graph, reformulated as a set of four ODEs and coded as a Scilab function [26]. With software packages supporting multibond graphs, the equations of motion can be automatically derived.

Multibond Graph of the Rotary Joint Manipulator

Since there is no translation, the multibond graphs of the two rigid bodies simplify (cf. to the multibond graph of a freely moving rigid body with two hinge points in Figure 8.16). The robot's base, body 0, does not move at all. As a result, Figure 12.58 gives a multibond graph of the rotary joint manipulator.

Derivation of the Standard Form of Robot Equations from the Multibond Graph

In the multibond graph of Figure 12.58, the vector $\boldsymbol{\omega}_1^1$ ($\boldsymbol{\omega}_2^2$) denotes the angular velocity of body 1 (body 2) with respect to reference frame 0 expressed in coordinates of reference frame 1 (reference frame 2). Actually,

$$\boldsymbol{\omega}_1^1 = \boldsymbol{\omega}_1^0 = [\, 0 \;\; \dot{\Theta}_1 \;\; 0 \,]^T \tag{12.56}$$

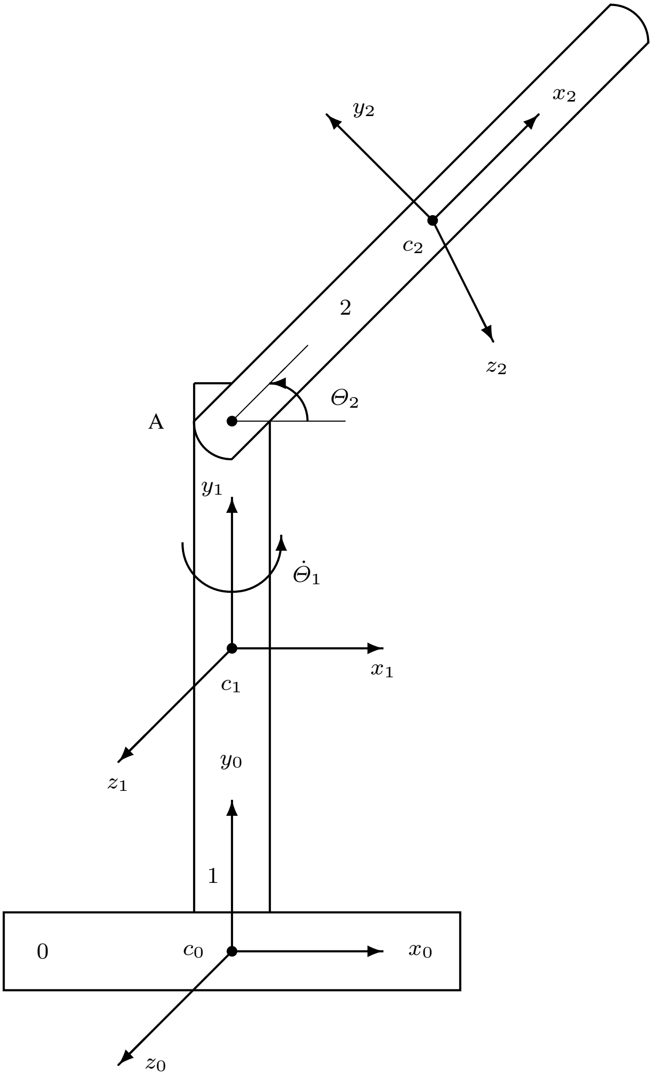

Fig. 12.57 Schematic of a two degrees of freedom rotary joint manipulator

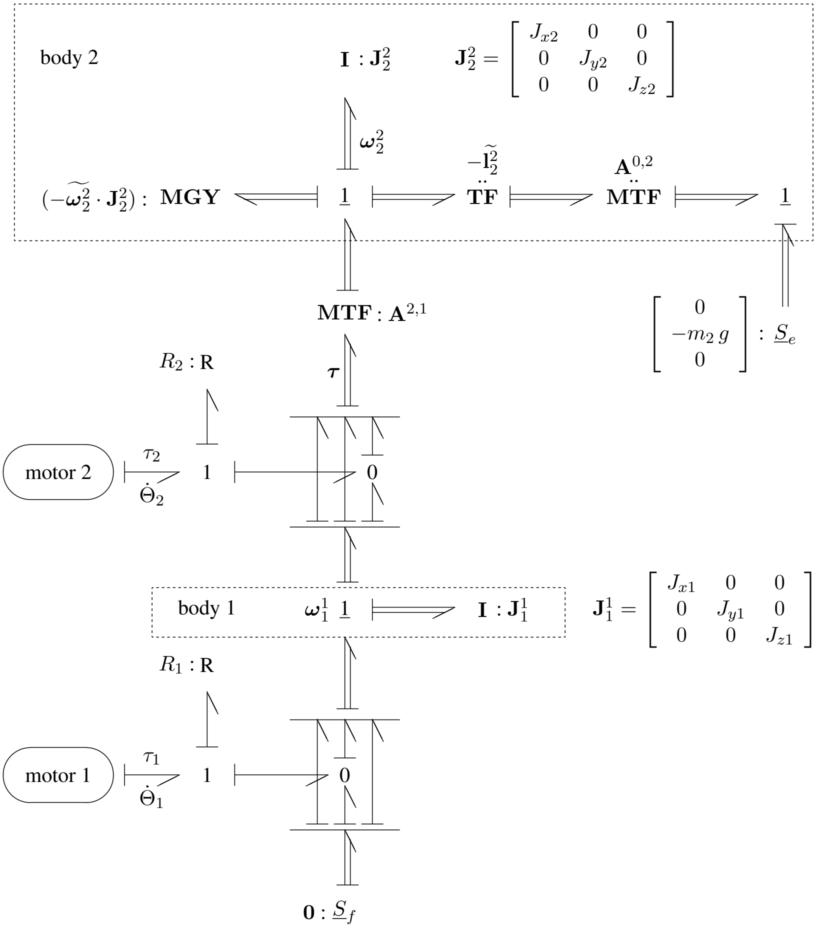

Fig. 12.58 Multibond graph of the two degrees of freedom rotary joint manipulator

where $\dot{\Theta}_1$ denotes the angular velocity of motor 1. Matrix $\mathbf{J}_1^1$ ($\mathbf{J}_2^2$) denotes the inertia matrix of body 1 (body 2) with respect to the reference frame sitting in the centre of gravity of body 1 (body 2). Both matrices are diagonal as the axes of the body fixed reference frames are parallel to the principal axes of inertia.

The modulated multiport transformer $\mathbf{MTF} : \mathbf{A}^{2,1}$ represents the transformation between the two reference frames of body 1 and body 2. Accordingly, the angular velocity of body 1 with respect to reference frame 0 expressed in coordinates of reference frame 2 reads

$$\boldsymbol{\omega}_1^2 = \underbrace{\begin{bmatrix} \cos\Theta_2 & \sin\Theta_2 & 0 \\ -\sin\Theta_2 & \cos\Theta_2 & 0 \\ 0 & 0 & 1 \end{bmatrix}}_{\mathbf{A}^{2,1}} \boldsymbol{\omega}_1^1 = \begin{bmatrix} \dot{\Theta}_1 \sin\Theta_2 \\ \dot{\Theta}_1 \cos\Theta_2 \\ 0 \end{bmatrix} . \tag{12.57}$$

Let $\boldsymbol{\omega}_2^2 = [\ \omega_{x2} \quad \omega_{y2} \quad \omega_{z2}\ ]^T$. Then according to the multibond graph in Figure 12.58,

$$\begin{bmatrix} \omega_{x2} \\ \omega_{y2} \\ \omega_{z2} \end{bmatrix} = \mathbf{A}^{2,1} \begin{bmatrix} 0 \\ \dot{\Theta}_1 \\ \dot{\Theta}_2 \end{bmatrix} = \begin{bmatrix} \dot{\Theta}_1 \sin\Theta_2 \\ \dot{\Theta}_1 \cos\Theta_2 \\ \dot{\Theta}_2 \end{bmatrix} . \tag{12.58}$$

In the same way, the matrix $\mathbf{A}^{0,2}$ relates the absolute velocity of the centre of gravity of body 2, c_2, expressed in coordinates of the body fixed reference frame to the same velocity expressed in coordinates of the inertial frame sitting in the centre of gravity of body 0.

$$\mathbf{A}^{0,2} = \begin{bmatrix} \cos\Theta_2 & -\cos\Theta_1 \sin\Theta_2 & \sin\Theta_1 \\ \sin\Theta_2 & \cos\Theta_2 & 0 \\ -\sin\Theta_1 \cos\Theta_2 & \sin\Theta_1 \sin\Theta_2 & \cos\Theta_1 \end{bmatrix} \tag{12.59}$$

Furthermore, l_2 denotes the distance of the centre of gravity of body 2, c_2, from the hinge point A. The vector from the origin of reference frame 2 to hinge point A expressed in coordinates of frame 2 is $\mathbf{l}_2^2 = [-l_2 \quad 0 \quad 0]^T$ and $\widetilde{\mathbf{l}_2^2}$ denotes the skew symmetric matrix generated by this vector. Consequently, according to the multibond graph in Figure 12.58, the moment acting on body 2 caused by the force of gravity is

$$m_2\, g \begin{bmatrix} 0 \\ 0 \\ l_2 \cos\Theta_2 \end{bmatrix} = \underbrace{\begin{bmatrix} 0 & 0 & 0 \\ 0 & 0 & l_2 \\ 0 & -l_2 & 0 \end{bmatrix}}_{(-\widetilde{\mathbf{l}_2^2})^T} \underbrace{\begin{bmatrix} c\,\Theta_2 & s\,\Theta_2 & -s\,\Theta_1 c\,\Theta_2 \\ -c\,\Theta_1 s\,\Theta_2 & c\,\Theta_2 & s\,\Theta_1 s\,\Theta_2 \\ s\,\Theta_1 & 0 & c\,\Theta_1 \end{bmatrix}}_{(\mathbf{A}^{0,2})^T} \begin{bmatrix} 0 \\ m_2\, g \\ 0 \end{bmatrix} , \tag{12.60}$$

where $c\,\Theta := \cos\Theta$ and $s\Theta := \sin\Theta$.

The moment acting on body 2 contributed by the Eulerian junction structure is

$$-\widetilde{\boldsymbol{\omega}_2^2}\, \mathbf{J}_2^2\, \boldsymbol{\omega}_2^2 = -\begin{bmatrix} 0 & \omega_{z2} & -\omega_{y2} \\ -\omega_{z2} & 0 & \omega_{x2} \\ \omega_{y2} & -\omega_{x2} & 0 \end{bmatrix} \underbrace{\begin{bmatrix} J_{x2} & 0 & 0 \\ 0 & J_{y2} & 0 \\ 0 & 0 & J_{z2} \end{bmatrix}}_{:= \mathbf{J}_2^2} \begin{bmatrix} \omega_{x2} \\ \omega_{y2} \\ \omega_{z2} \end{bmatrix}$$

$$= \begin{bmatrix} J_{z2}\, \omega_{y2}\, \omega_{z2} & - & J_{y2}\, \omega_{y2}\, \omega_{z2} \\ J_{x2}\, \omega_{x2}\, \omega_{z2} & - & J_{z2}\, \omega_{x2}\, \omega_{z2} \\ J_{y2}\, \omega_{x2}\, \omega_{y2} & - & J_{x2}\, \omega_{x2}\, \omega_{y2} \end{bmatrix} . \tag{12.61}$$

Let $\boldsymbol{\tau} \;=\; [\;\tau_{x1}\;\;\tau_{y1}\;\;\tau_{z1}\;]^T$. Then, summation of moments at the 1-junction of $\boldsymbol{\omega}_2^2$ and transformation across the multiport transformer $\mathbf{MTF} : \mathbf{A}^{21,}$ gives

$$\boldsymbol{\tau} \;=\; (\mathbf{A}^{2,1})^T \,(\, \mathbf{J}_2^2\,\dot{\boldsymbol{\omega}}_2^2 \;+\; (-\widetilde{\boldsymbol{\omega}_2^2})\,\mathbf{J}_2^2\,\boldsymbol{\omega}_2^2 \;+\; m_2\,g \begin{bmatrix} 0 \\ 0 \\ l_2\cos\Theta_2 \end{bmatrix} \,)\;. \tag{12.62}$$

Finally, summation of torques at the 1-junction of $\dot{\Theta}_2$ yields

$$\tau_2 \;=\; R_2\dot{\Theta}_2 \;+\; \tau_{z1}\;. \tag{12.63}$$

Expanding this equations by using Equations 12.62, 12.61, 12.58 and 12.57 gives one of the two Lagrange equations describing the motion of the rotary joint manipulator.

$$\tau_2 \;=\; R_2\dot{\Theta}_2 \;+\; \underbrace{J_{z2}}_{=:\,m_{22}}\;\ddot{\Theta}_2 \underbrace{\;-\;(J_{x2}-J_{y2})(\sin\Theta_2\cos\Theta_2)\,\dot{\Theta}_1^2}_{=:\,C_{21}}\;\underbrace{+\;m_2\,g\,l_2\cos\Theta_2}_{=:\,g_{21}} \tag{12.64}$$

The second Lagrange equation is obtained in the same manner. Summation of torques on the 1-junction of $\dot{\Theta}_1$ gives

$$\tau_1 \;=\; R_1\dot{\Theta}_1 \;+\; J_{y1}\ddot{\Theta}_1 \;+\; \tau_{y1}\;. \tag{12.65}$$

After evaluation of Equation 12.62, the torque τ_{y1} becomes

$$\begin{aligned}
\tau_{y1} = \begin{bmatrix}\sin\Theta_2 \;\cos\Theta_2\; 0\end{bmatrix} & \left(\begin{bmatrix} J_{x2}\dot{\omega}_{x2} \\ J_{y2}\dot{\omega}_{y2} \\ J_{z2}\dot{\omega}_{z2} \end{bmatrix} \right. \\
&+ \left. \begin{bmatrix} J_{z2}\,\omega_{y2}\,\omega_{z2} \;-\; J_{y2}\,\omega_{y2}\,\omega_{z2} \\ J_{x2}\,\omega_{x2}\,\omega_{z2} \;-\; J_{z2}\,\omega_{x2}\,\omega_{z2} \\ J_{y2}\,\omega_{x2}\,\omega_{y2} \;-\; J_{x2}\,\omega_{x2}\,\omega_{y2} \end{bmatrix} \;+\; m_2\,g \begin{bmatrix} 0 \\ 0 \\ l_2\cos\Theta_2 \end{bmatrix} \right) \\
= J_{x2}\dot{\omega}_{x2}\sin\Theta_2 \;&+\; J_{y2}\dot{\omega}_{y2}\cos\Theta_2 \\
+\;(J_{z2}-J_{y2})&\omega_{y2}\omega_{z2}\sin\Theta_2 \\
+\;(J_{x2}-J_{z2})&\omega_{x2}\omega_{z2}\cos\Theta_2\;.
\end{aligned} \tag{12.66}$$

Finally, observing Equation 12.58, the second Lagrange equation reads

$$\begin{aligned}
\tau_1 = R_1\dot{\Theta}_1 \;&+\; \underbrace{(J_{y1} + J_{x2}\sin^2\Theta_2 + J_{y2}\cos^2\Theta_2)}_{m_{11}}\,\ddot{\Theta}_1 \\
&+\; \underbrace{(2(J_{x2}-J_{y2})\sin\Theta_2\cos\Theta_2)}_{b_{11}}\;\dot{\Theta}_1\dot{\Theta}_2\;.
\end{aligned} \tag{12.67}$$

That is, Equation 12.55 takes the form

$$\underbrace{\begin{bmatrix} m_{11} & 0 \\ 0 & m_{22} \end{bmatrix}}_{\mathbf{M}} \begin{bmatrix} \ddot{\Theta}_1 \\ \ddot{\Theta}_2 \end{bmatrix} + \underbrace{\begin{bmatrix} b_{11} \\ 0 \end{bmatrix}}_{\mathbf{B}} \begin{bmatrix} \dot{\Theta}_1 \dot{\Theta}_2 \end{bmatrix} + \underbrace{\begin{bmatrix} 0 & 0 \\ c_{21} & 0 \end{bmatrix}}_{\mathbf{C}} \begin{bmatrix} \dot{\Theta}_1^2 \\ \dot{\Theta}_2^2 \end{bmatrix} + \underbrace{\begin{bmatrix} 0 \\ g_{21} \end{bmatrix}}_{\mathbf{G}(\boldsymbol{\Theta})} =$$

$$\begin{bmatrix} \tau_1 \\ \tau_2 \end{bmatrix} - \begin{bmatrix} R_1 \dot{\Theta}_1 \\ R_2 \dot{\Theta}_2 \end{bmatrix} . \qquad (12.68)$$

Notice that the entries in the matrices $\mathbf{B}$ and $\mathbf{C}$ are zero when either $\Theta_2 = 0$ or $\Theta_2 = \pi/2$.

Simulation of the Robot's Motion

For a simulation of the robot's motion, the parameters listed in Table 12.11 have been used [29]. In this table, c_i denotes the centre of gravity of body i. Given the parameters in Table 12.11, Figure 12.59 displays the time evolution of the angular velocities ω_1, ω_2 and of the angle Θ_2. As can be seen from Figure 12.59, with increasing time, the angular velocity of body 1 takes a steady state value of about $0.66\ rad$, ω_2 becomes zero and consequently, takes a constant value of about -0.1. These values can be verified. Under the conditions $\omega_1 =$ const. and $\omega_2 = 0$, the dynamic Equation 12.67 reduces to

$$\omega_1 = \frac{\tau_1}{R_1} = 1.0/1.5 = 0.66\, rad/s\ . \qquad (12.69)$$

When $\Theta_2 =$ const., Equation 12.64 reduces to a nonlinear algebraic equation for Θ_2.

$$\tau_2 = m_2 g l_2 \cos\Theta_2 - (J_{x2} - J_{y2})(\sin\Theta_2 \cos\Theta_2)\dot{\Theta}_1^{\,2} \qquad (12.70)$$

A numerical solution of Equation 12.70 is $\Theta_2 = -0.0999574\ rad$.

Table 12.11 Parameter values used for simulation of the robot's motion

Parameter	Value	Units	Meaning
J_{y1}	6	kgm^2	Moment of inertia of body 1 with respect to c_1
J_{x2}	5	kgm^2	Moment of inertia of body 2 with respect to c_2
J_{y2}	10	kgm^2	Moment of inertia of body 2 with respect to c_2
J_{y2}	10	kgm^2	Moment of inertia of body 2 with respect to c_2
m_2	40	kg	Mass of body 2
l_2	0.5	m	Distance c_2 - pivot point A (cf. Figure 12.57)
R_1	1.5	Nms/rad	Friction between body 0 and body 1
R_2	2.0	Nms/rad	Friction in pivot point A
τ_1	1.0	Nm	Torque acting on body 1
τ_2	195	Nm	Torque acting on body 2

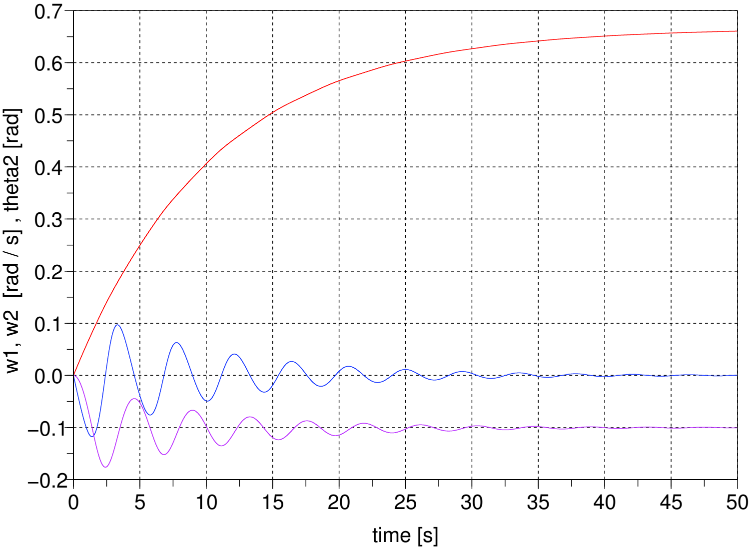

Fig. 12.59 Time evolution of the angular velocities ω_1, ω_2 and of the angle Θ_2

12.10 Fluid Level Control in a Three Tank System

One of the usual tasks in process engineering systems is to control the fluid level in tanks. As an example, the system of three coupled tanks depicted in Figure 12.60 is considered. It is assumed that

- the fluid flow is one way from left to right,
- the fluid inertia can be neglected,
- there is a uniform hydrostatic pressure at the bottom of each tank,
- isothermal conditions apply,
- hydraulic power can be approximated by the product of hydrostatic pressure and volume flow.

In this example, the task is to control the fluid level in the last right-hand side tank. To that end, the level is sensed and fed into a PID controller that controls the fluid flow supply into the first tank as shown in Figure 12.60. In [15], Hoffmann starts from the equations and presents a MATLAB®/Simulink® simulation of this example.

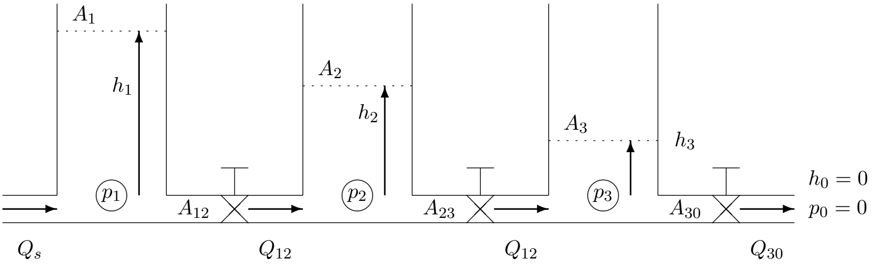

Fig. 12.60 Schematic of a three tank system

Bond Graph Model of the Three Tank System

Bond graph modelling of this hydraulic plant is straightforward. The valves in the pipes connecting the tanks are modelled by resistors. Their constitutive relation is given by Bernoulli's law. The pressure at the bottom of the tanks is represented by a 0-junction and the storage of potential energy in the tanks is taken into account by a C element. Accordingly, Figure 12.61 represents a bond graph model of the three tank system.

Let A_{ij} be the cross section area of the valve between pressures p_i and p_j. According to Bernoulli's law, the volume flow Q_{ij} through the valve equals

$$\begin{aligned} Q_{ij} &= A_{ij}\,\mathrm{sign}(\Delta \mathrm{p_{ij}})\sqrt{\frac{2}{\varrho}|\Delta \mathrm{p_{ij}}|} \\ &= A_{ij}\,\mathrm{sign}(\Delta \mathrm{h_{ij}})\sqrt{2\mathrm{g}|\Delta \mathrm{h_{ij}}|}\,. \end{aligned} \tag{12.71}$$

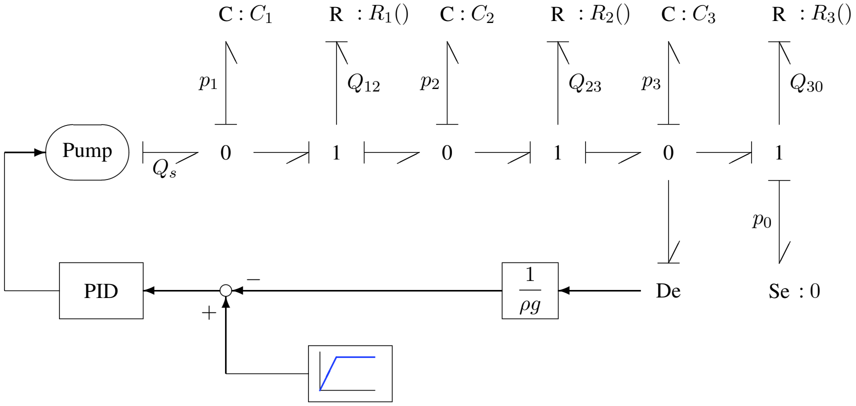

Fig. 12.61 Bond graph of the three tank system

Dynamic Equations of the Three Tank System

The dynamic equations are immediately derived from the bond graph of Figure 12.61.

$$\dot{p}_1 = \frac{1}{C_1}\left(Q_s - Q_{12}\right) \tag{12.72a}$$

$$\dot{p}_2 = \frac{1}{C_2}\left(Q_{12} - Q_{23}\right) \tag{12.72b}$$

$$\dot{p}_3 = \frac{1}{C_1}\left(Q_{23} - Q_{30}\right) \tag{12.72c}$$

An equal cross section area for all three valves implies that in steady state

$$h_2 = 2h_3 \tag{12.73a}$$

$$h_1 = 3h_3 \tag{12.73b}$$

(as depicted in Figure 12.60) and

$$Q_s = Q_{12} \ = \ Q_{23} \ = \ Q_{30} \ . \tag{12.74}$$

Adopting the values $Q_s = 1 \ m^3/s$ and $A_{12} = 0.1 \ m^2$ results in the steady state fluid levels

$$h_1 = 15.29 \, m \ , \quad h_2 \ = \ 10.19 \, m \ , \quad h_3 \ = \ 5.097 \, m \ . \tag{12.75}$$

Simulation of the Uncontrolled Three Tank System

Simulation of the uncontrolled system's behaviour confirms these steady values (cf. Figure 12.62 and Figure 12.63). Numerical values used for simulation of the uncontrolled systems are listed in Table 12.12.

Simulation of the Controlled Three Tank System

The transfer function of the PID controller is used in the form

Table 12.12 Parameters for simulation of the uncontrolled three tank system

Parameter	Value	Units	Meaning
$A_1 = A_2 = A_3$	1.999	m^2	Cross section area of the tanks
$A_{12} = A_{23} = A_{30}$	0.1	m^2	Cross section area of the valves
ϱ	780	kg/m^3	Fluid density
Q_s	1	m^3/s	Volume flow of the supply

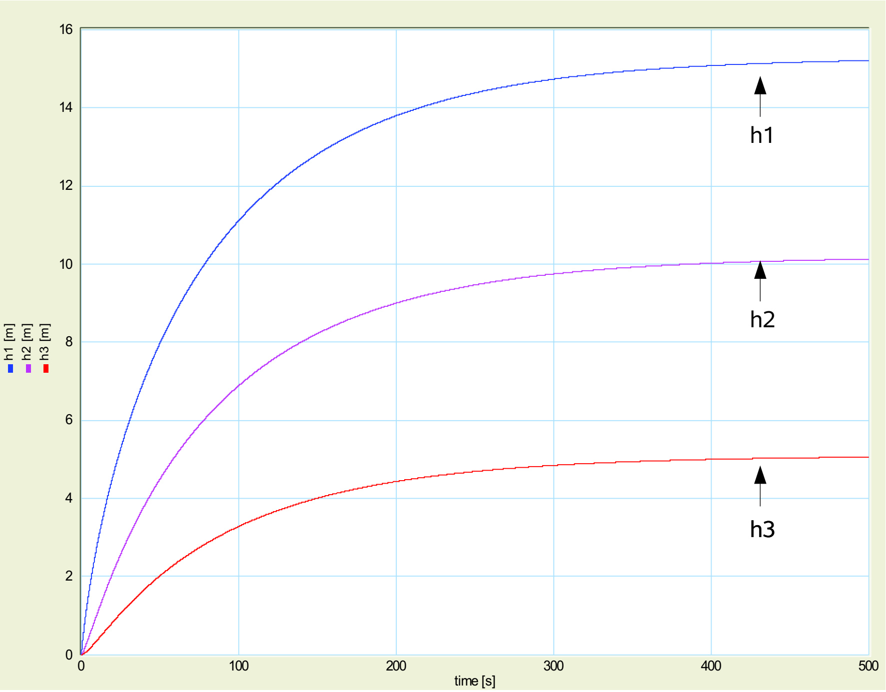

Fig. 12.62 Time evolution of fluid levels in the uncontrolled three tank system due to a step of Q_s

$$U(s) \;=\; K \left[1 + \frac{1}{T_i\, s} + \frac{T_d\, s}{1 + \dfrac{T_d}{N}\, s} \right] E(s) \;, \tag{12.76}$$

where $s \in \mathbb{C}$ and E and U denote the Laplace transforms of the input error and the controller output. Table 12.13 gives the parameters of the PID controller.

If details of the hydraulic power supply subsystem are known, a bond graph can be developed for the submodel called pump in the bond graph of Figure 12.61. Otherwise, it may be appropriate and sufficient to approximate the pump's delay in response to an immediate step in the controller signal by a first order lag signal element and to account for saturation of the volume flow Q_s by a satura-

Table 12.13 Parameters of the PID controller

Parameter	Value	Units	Meaning
K	5		Proportional gain
Ti	50	s	Integral time constant
Td	3	s	Derivative time constant
N	20		Derivative gain limitation

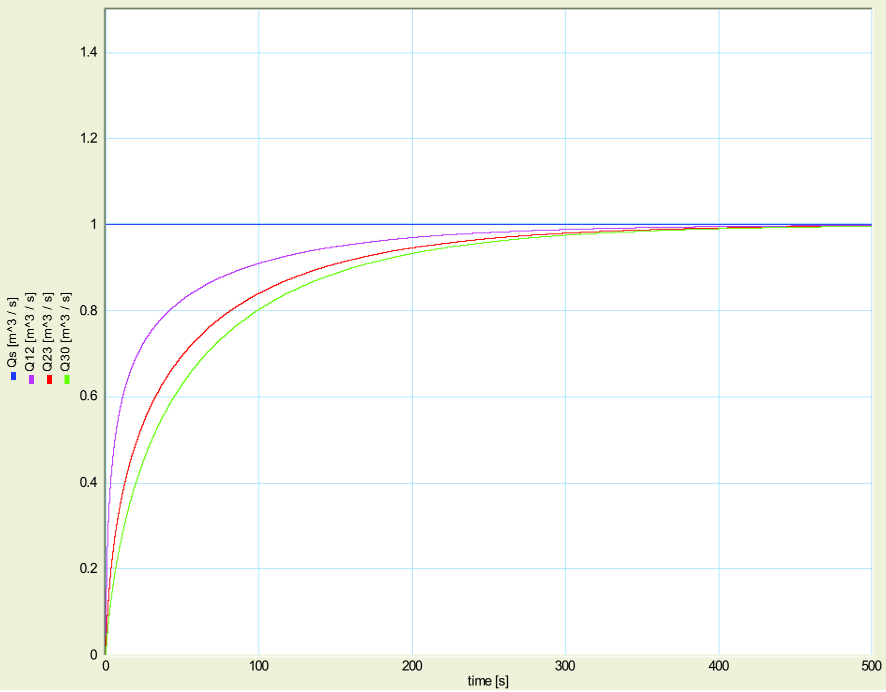

Fig. 12.63 Time evolution of volume flows in the uncontrolled three tank system

tion signal block. The first order lag element is described by a transfer function $G(s) := k/(\tau s+1)$, where k denotes the proportional gain and τ the time constant. Parameters of these two signal blocks are given in Table 12.14.

Figure 12.64 shows the time history of the fluid levels in the tanks if all of them are initially empty and if the set point for the fluid level in the third tank is $1\,m$. Again, in steady state, Equations 12.73a–12.73b hold. Figure 12.65 shows the dynamics of the volume flows in the controlled system.

According to Equation 12.71 and given the set point of $1\,m$ for the fluid level h_3, a steady state value of

$$Q_{30} = A_{30}\sqrt{2g} = 0.1\sqrt{2 \times 9.81} = 0.4429\,m^3/s \tag{12.77}$$

Table 12.14 Parameters of the first order lag element and the saturation block

Parameter	Value	Units	Meaning
k_p	1		Proportional gain
τ	1	s	Time constant
min	0	m^3/s	lower bound
max	2.5	m^3/s	upper bound of the saturation block

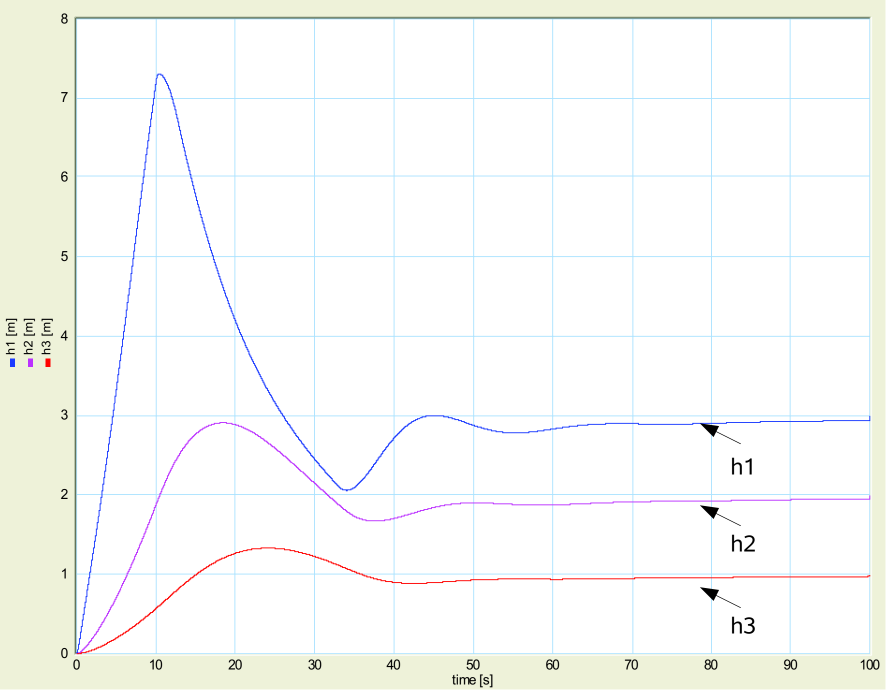

Fig. 12.64 Time evolution of fluid levels in the controlled three tank system

is obtained. This and Equation 12.74 is confirmed by the simulation results in Figure 12.65. Figure 12.66 shows the history of the volume flows in case the set point for the fluid level in tank 3 rises linearly to its value of $1\,m$ within a time interval of $10\,s$. The simulation results displayed in Figure 12.66 agree with those given in [15].

For further reading on bond graph modelling of controlled hydraulic systems, refer to the textbook of Dransfield [9].

12.11 Fault Detection in a Hydraulic Two Tank System

This section illustrates the bond graph model-based approach to FDI introduced in Section 6.8 by application to the simple hydraulic two tank system displayed in Figure 6.12 and reproduced in Figure 12.67 for the sake of convenience. It is assumed that the pressures in both tanks are measured. For simplicity, only the mass flow is considered. Associated thermal convection is not taken into account.

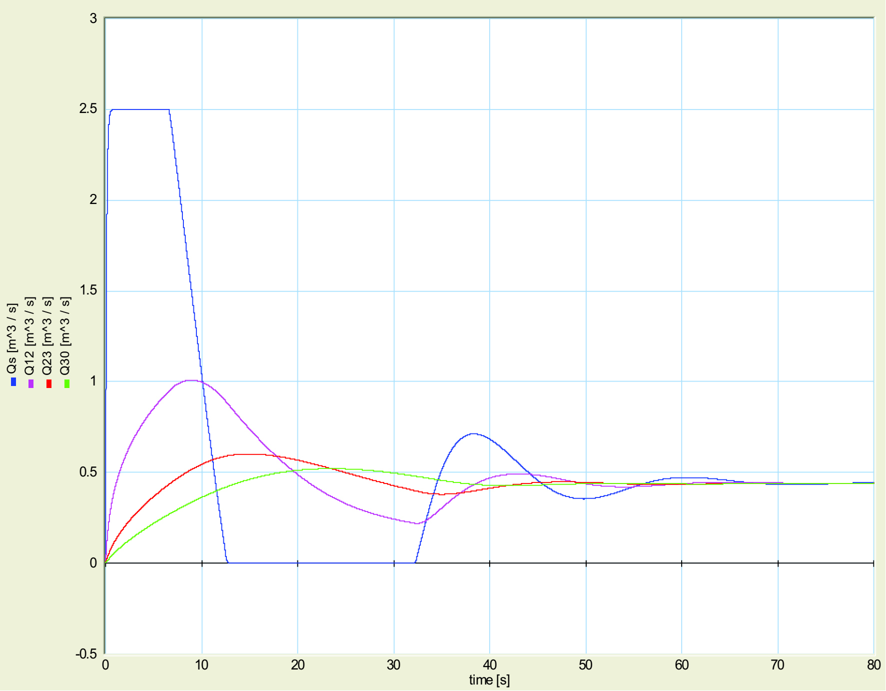

Fig. 12.65 Dynamics of the volume rates in the controlled three tank system

Bond Graph Models of the Two Tank System Coupled by Residual Sinks

Figure 12.68 shows a behavioural model of the process subject to faults (lower part of Figure 12.68) coupled to a model of the faultless process (upper part of Figure 12.68) by modulated effort sources and residual flow sinks. The measuring of the tank pressures has been taken into account by effort detectors (De-elements) attached to the 0-junctions. A fault such as leakage from a tank can be introduced into the model of the real process by switching the modulated flow sinks, MSf, attached to the 0-junctions of the tank pressures on and off.

A partial blockage of a valve results in a reduction of the valve's parameter $k = c_d A_V(t)\sqrt{2/\varrho}$. Hence, k is a function of time, t, that takes into account the way in which the valve blocks. This may take place abruptly or progressively. Accordingly, the valves are represented by modulated resistors in the model of the *faulty* process. As a result, the model of the real process differs from that of the faultless model by these elements allowing, for user introduced faults.

In the integrated model, all energy stores take preferred integral causality. Due to the residual sinks, the underlying mathematical model is a DAE system.

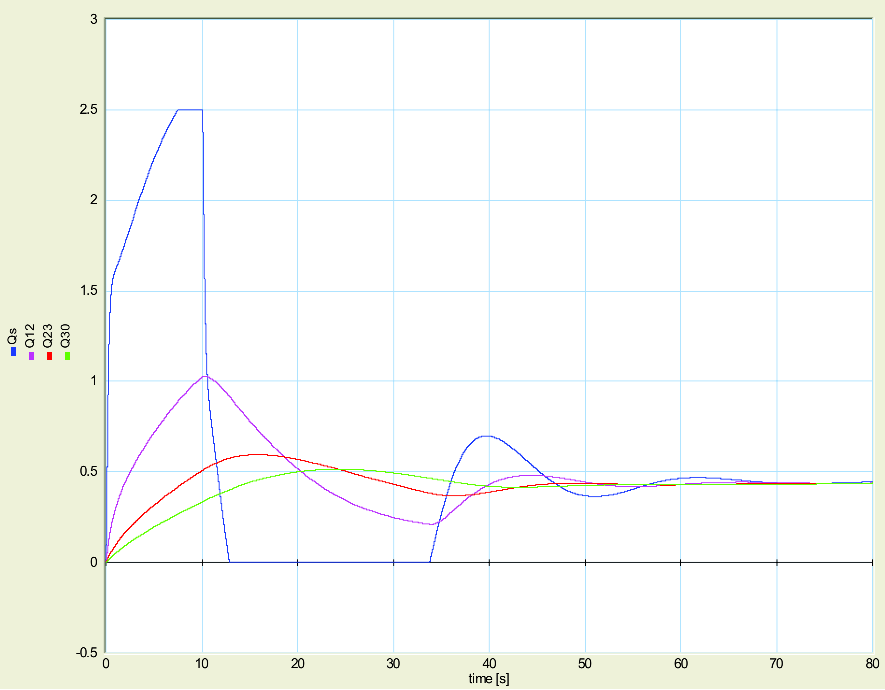

Fig. 12.66 History of the volume rates in the controlled three tank system in case the controller's set point rise is limited

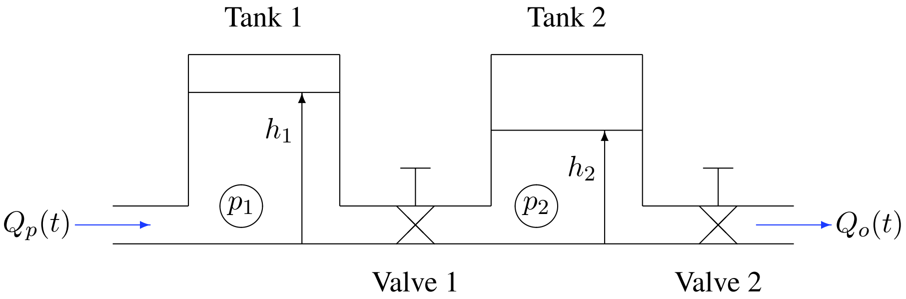

Fig. 12.67 Schematic of a hydraulic two tank system reproduced from Figure 6.12

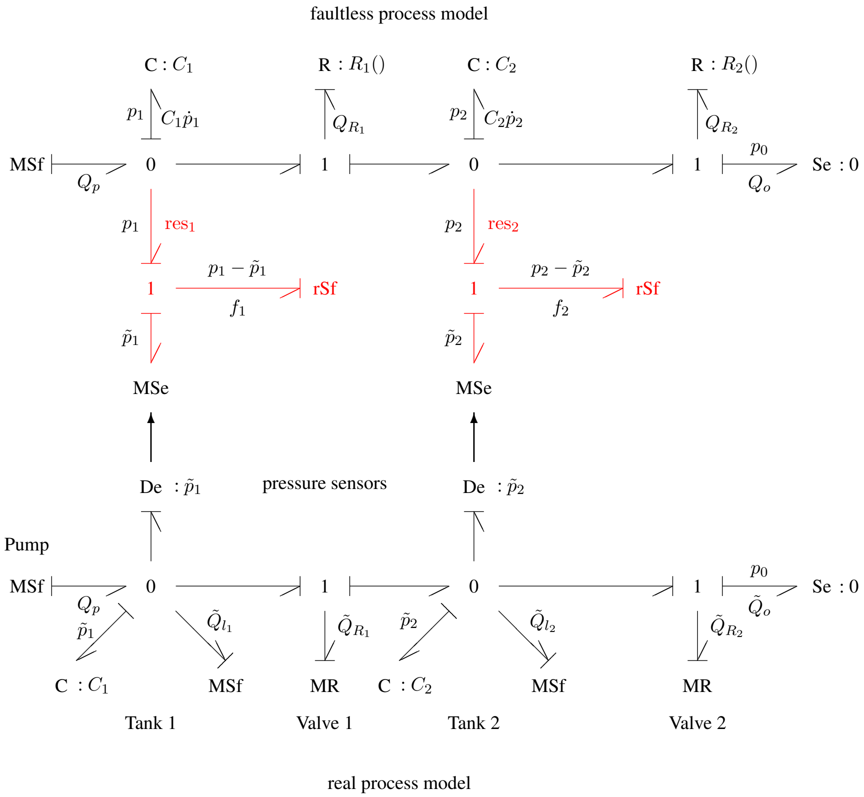

Fig. 12.68 Coupling of a faulty process model (lower part) to a faultless process model (upper part) by means of residual flow sinks

The DAE System Derived from the Coupled Bond Graphs

Derivation of model equations from the causal bond graph in Figure 12.68 is straightforward. In this case study, they have been formulated in Scilab's mathematical input language and stored in a script to be read by Scilab. The Scilab function of the DAE system of the overall model to be passed in a call to the solver DASSL is displayed in Figure 12.69.

The application of the solver DASSL requires that all equations are written in implicit form. In the Scilab script, the residuals r(i), $i = 1, \ldots, 6$, are not to be confused with the residuals of the ARRs to be computed. The latter variables are denoted f_1, f_2. In the behavioural model of the real engineering process, perturbed power variables are denoted by a name that starts with the letter t standing for tilde.

With $\mathbf{x}_p := [p_1, p_2, \tilde{p}_1, \tilde{p}_2]^T$ and $\mathbf{w} := [f_1, f_2]$ as components of a descriptor vector, the DAE system of the example, in fact, is a semi-explicit DAE of the form of Equation 6.105. Its index is 2. In this example, the matrices in Equation 6.106

```
// Scilab function including the DAE system of the two tank models
// coupled by two residual flow sinks
function [res, ires] = daesys(t,x,xdot)

// components of the descriptor vector x = [x_p, w]:
// tank pressures (faultless process model):
p1   = x(1)
p2   = x(2)
// tank pressures (faulty process model):
tp1  = x(3)
tp2  = x(4)   // x_p := [ p1,p2,tp1,tp2 ]
// residuals:
f1   = x(5)
f2   = x(6)   // w := [ f1, f2 ]

// time derivatives of the components of the descriptor vector:
dp1  = xdot(1)
dp2  = xdot(2)
dtp1 = xdot(3)
dtp2 = xdot(4)
df1  = xdot(5)
df2  = xdot(6)

// system inputs: volume flow of the feed pump
Qp   = Flow*pulse(t,tstart,tstop)

// no leakage from the two tanks of the real process:
tQl1 = 0.0
tQl2 = 0.0

// volume flows through the valves:
QR1  = orifice(AV1,p1,p2)
QR2  = orifice(AV2,p2,p0)

// partial blockage of valve 1 for 50.0s <= t <= 60.0s:
tQR1 = (1.0 - pulse2(t,50.0,60.0,0.8))*orifice(AV1,tp1,tp2)
tQR2 = orifice(AV2,tp2,p0)

// continuity equations for the tanks in both submodels:
r(1) = Qp - QR1 - C1*dp1 - f1                // p1
r(2) = QR1 - QR2 - C2*dp2 - f2               // p2
r(3) = Qp - tQR1 - tQl1 - C1*dtp1            // tp1
r(4) = tQR1 - tQR2 - tQl2 - C2*dtp2          // tp2

// equations of the residual flow sinks:
r(5) = p1 - tp1                              // f1
r(6) = p2 - tp2                              // f2

ires = 0  // indicator of successful computation of r
endfunction
```

Fig. 12.69 Scilab function including the DAE system of the two tank models coupled by residual flow sinks take the form

$$\frac{\partial \mathbf{f}_2}{\partial \mathbf{x}_p} = \begin{bmatrix} 1 & 0 & -1 & 0 \\ 0 & 1 & 0 & -1 \end{bmatrix} \tag{12.78}$$

and

$$\frac{\partial \mathbf{f}_1}{\partial \mathbf{w}} = \begin{bmatrix} -1/C_1 & 0 \\ 0 & -1/C_2 \\ 0 & 0 \\ 0 & 0 \end{bmatrix} . \tag{12.79}$$

Consequently,

$$\det\left(\frac{\partial \mathbf{f}_2}{\partial \mathbf{x}_p}\frac{\partial \mathbf{f}_1}{\partial \mathbf{w}}\right) = \det\begin{bmatrix} -1/C_1 & 0 \\ 0 & -1/C_2 \end{bmatrix} = \frac{1}{C_1 C_2} \neq 0 . \tag{12.80}$$

Simulation of the Faultless System Behaviour

The numerical solution of a DAE system requires a consistent set of initial conditions for the components of the descriptor vector and their time derivatives. For the consistent initialisation of a DAE system, the algorithm of Pantelides [22] can be used. To facilitate the specification of a consistent set of initial conditions, it is assumed that the two tanks are empty at initial time $t = 0$ and that the pump delivers a constant volume flow, Q_p, for the time period $10.0\,s \leq t \leq 40.0\,s$. That is, the empty tanks are filled for 30 s. Thereafter, they discharge at a rate depending on how much the valves are open. Figure 12.70 depicts the undisturbed dynamic behaviour. The parameters of the hydraulic two tank system are given in Table 12.15.

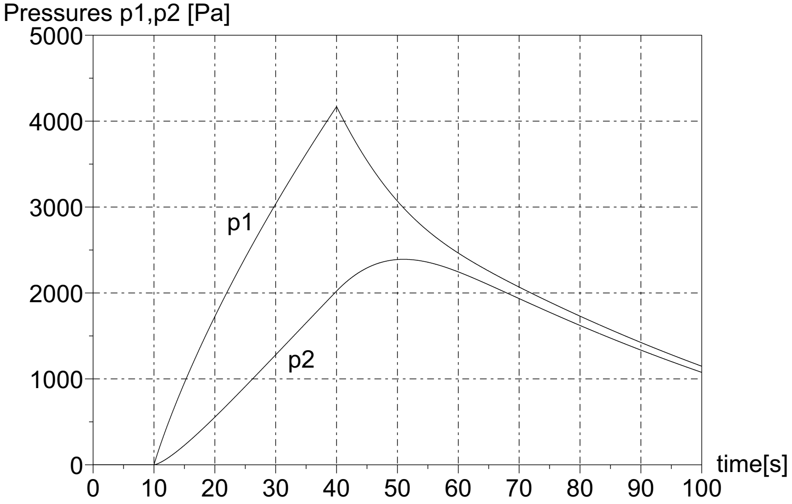

Fig. 12.70 Time history of the tank pressures in faultless operation mode

Table 12.15 Parameters of the hydraulic two tank system

Parameter	Value	Units	Meaning
g	9.81	m/s^2	Gravitational acceleration
ϱ	780	kg/m^3	Oil density
c_d	0.61		Discharge coefficient
$A_{T_1} = A_{T_2}$	0.153	m^2	Cross sectional area of the tanks
$C_1 = C_2 = A_{T_1}/(\varrho\, g)$		m^3/Pa	Capacitances of the tanks
A_{V_1}	$0.2 \cdot 10^{-2}$	m^2	Cross sectional area of valve 1
A_{V_2}	$0.1 \cdot 10^{-2}$	m^2	Cross sectional area of valve 2
Flow	$0.5 \cdot 10^{-2}$	m^3/s	Volume flow of the pump
Q_l	$0.1 \cdot 10^{-2}$	m^3/s	Leakage from tank 1
p_0	0.0	Pa	Pressure of the environment

Study of Fault Scenarios

In this case study, two types of faults are considered, namely leakage from the tanks and partial blockage of the valves. As a first fault scenario, a constant leakage flow from tank 1 is assumed to be effective for the time period $50\,s \leq t \leq 60\,s$, while the two tanks discharge. As a result, the pressures in the tanks decrease at a higher rate during this time period. Figure 12.71 shows the time history of the tank pressures in the case of a leakage from tank 1.

Leakage from tank 1 corresponds to a decrease of the area of its bottom. According to the fault signature matrix of Table 6.5, residual res_1 is affected, while residual

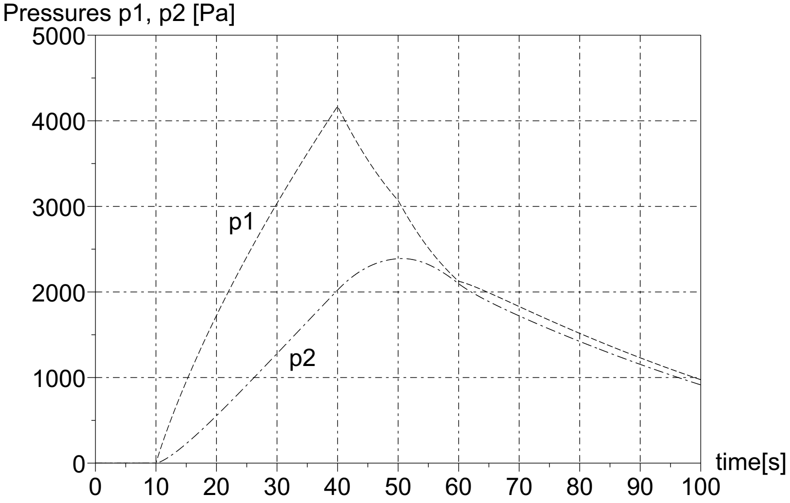

Fig. 12.71 Time history of the tank pressures in the case of a leakage from tank 1

res_2 is not. Figures 12.72 and 12.73 depicting the residuals f_1 and f_2 validate this expectation. Note that at $t = 60\,s$, the leakage from tank 1 abruptly stops. The system abruptly returns to normal mode operation. Accordingly, residual f_1 abruptly drops to zero.

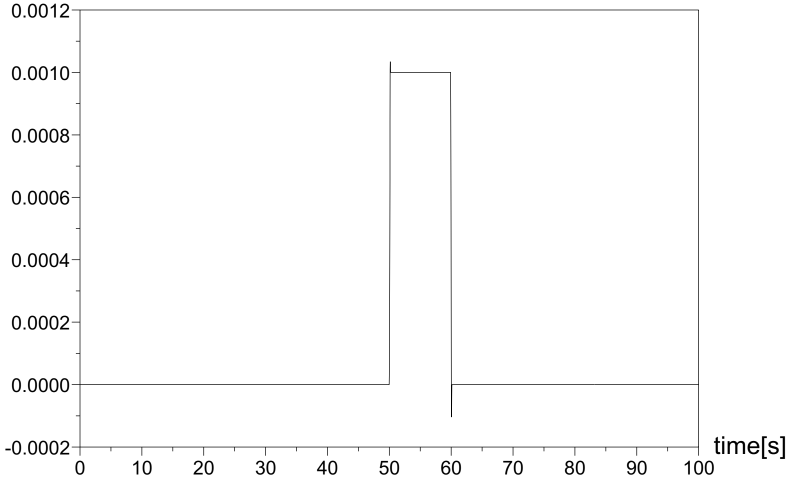

Fig. 12.72 Residual f_1 in the case of a leakage from tank 1 during the time interval $50\,s \leq t \leq 60\,s$

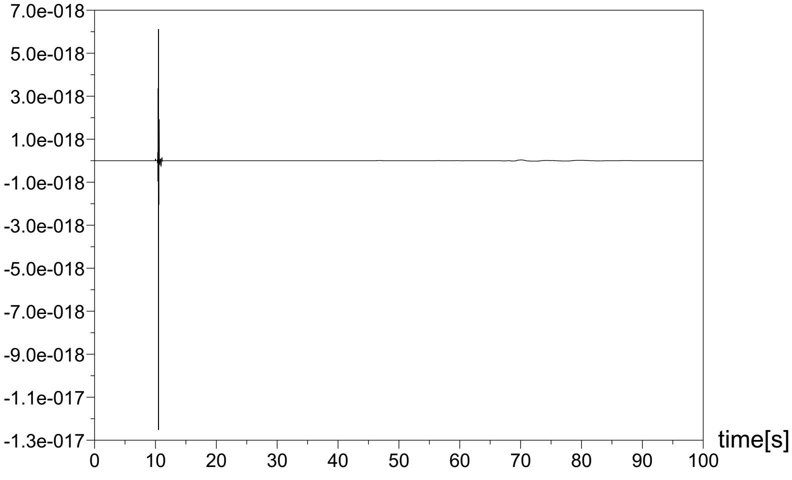

Fig. 12.73 Residual f_2 in the case of a leakage from tank 1

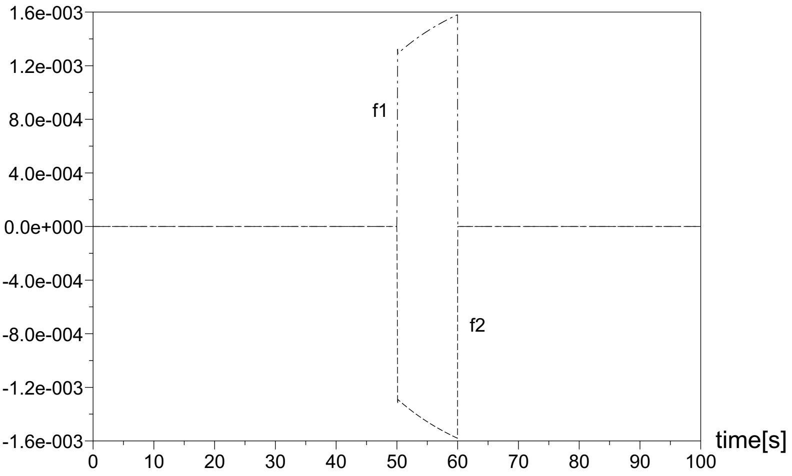

Fig. 12.74 Residuals f_1 and f_2 in the case of partial blockage of the valve 1 during the time interval $50\,s \leq t \leq 60\,s$

As a second fault scenario, partial blockage of the valve between the two tanks is assumed to be effective during the time interval $50\,s \leq t \leq 60\,s$ after the constant flow pump has been switched off. Consequently, the pressure in tank 1 decreases at a lower rate, while the pressure in tank 2 decreases at a higher rate. Its outlet is not affected, but its inlet is chocked. According to the fault signature matrix 6.5, both residuals should be sensitive to this type of fault. This is verified by Figure 12.74.

12.12 Heated Stirred Tank

Bond graph modelling of thermal systems is the subject of a book by Thoma and Bouamama [27]. In this section, the simple example of a single heated stirred tank considered in Section 10.1.1 is taken as a subject of a small modelling and simulation study (cf. [13, 29]). The schematic of the tank and a pseudo bond graph model are redisplayed in Figure 12.75 and Figure 12.76.

The following assumptions apply.

- The fluid flow is one way from left to right.
- The mass flow can be considered incompressible; inertia effects can be neglected.
- The mass flow $\dot{m}_i$ and the temperature T_i at the tank inlet are constant.
- There is a uniform hydrostatic pressure at the bottom of the tank.
- The fluid in the tank is heated. The heat is supplied at constant rate. Stirring ensures a spatially uniformly distributed temperature T.
- Heat losses to the ambient and the heat capacity of the tank wall can be neglected.

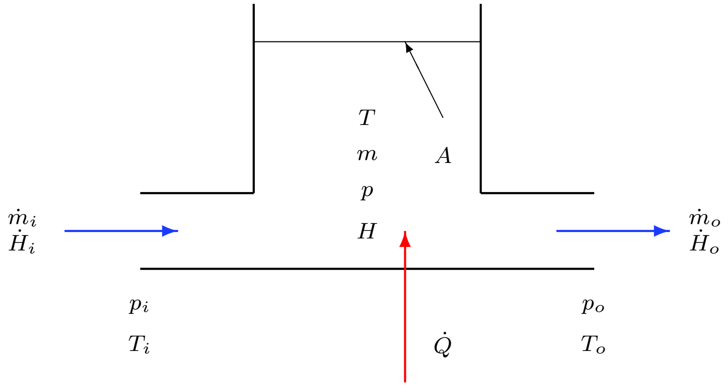

Fig. 12.75 Heated stirred tank

Constitutive Relations of the Elements

As the pressure at the hydraulic inlet resistor only affects the (ideal) source of hydraulic power supply, it can be omitted. The constitutive relation (CR) of the hydraulic outlet resistor is

$$\dot{m}_o = k_2\sqrt{p} \, . \tag{12.81}$$

The constitutive realtion of the hydraulic capacitor is

$$p = \frac{1}{C_h} m \, , \tag{12.82}$$

where $C_h = A/\varrho$.

The thermal capacitor's constitutive relation is

$$T = \frac{1}{C_{therm}} H \, , \tag{12.83}$$

where $C_{therm} = c \times m$.

The constitute relation of the thermal resistors is

$$\dot{H}_{index} = c\,\dot{m}_{index}\,T_{index} \, , \tag{12.84}$$

where index either denotes the inlet or the outlet resistor.

Table 12.16 gives the parameters of the simulation study (cf. [29]). The fluid flow enters the tank at a mass flow of $4 \; kg/s$. At time instance $t = 1500\,s$, this value increases to $4.8 \; kg/s$. That is,

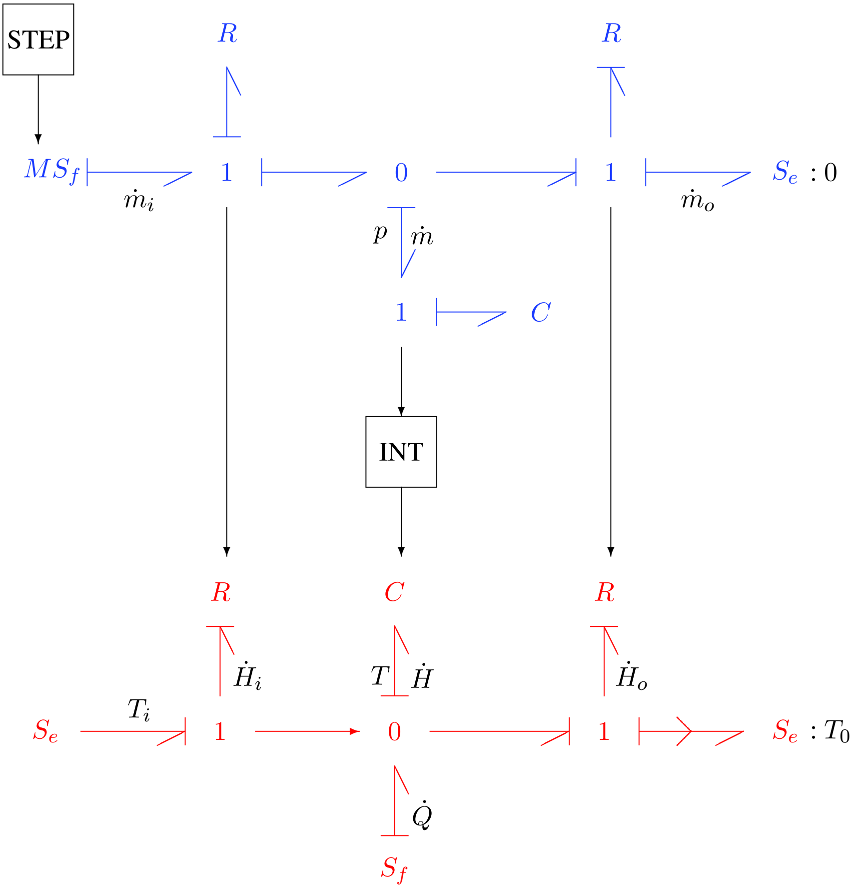

Fig. 12.76 Pseudo bond graph of the heated stirred tank

$$\dot{m}_i = \begin{cases} 4.0\ kg/s & 0\ s \leq t < 1500\ s \\ 4.8\ kg/s & t \geq 1500\ s \end{cases} . \tag{12.85}$$

Simulation Results

Figure 12.77 shows the time evolution of the temperature and the fluid level in the tank. As can be seen from Figure 12.77, the fluid level as well as the temperature in the tank increase due to an inflow at constant mass flow and due to constant heating of the fluid. Then, due to the immediate increase of the mass flow at time $t = 1500\,s$ and a continued unchanged constant heating of the fluid, the fluid level further increases while the temperature in the tank decreases.

Table 12.16 Parameters of the simulation study

Parameter	Value	Units	Meaning
g	9.81	m/s^2	gravitational acceleration
ϱ	800	kg/m^3	Fluid density
c_p	200	$J/(kg\ ^oC)$	specific heat
A	1.0	m^2	Cross section area of the tank
k_2	5.824×10^{-2}	$\sqrt{kg\, m}$	Coefficient of the hydraulic outlet resistor
T_i	20	^oC	Inlet temperature
$\dot{Q}$	40	kW	Heat flow
$h(0)$	0.4	m	Initial fluid level in the tank
$T(0)$	45	^oC	Initial temperature in the tank
$H(0)$	2.88×10^6	J	Initial enthalpy in the tank

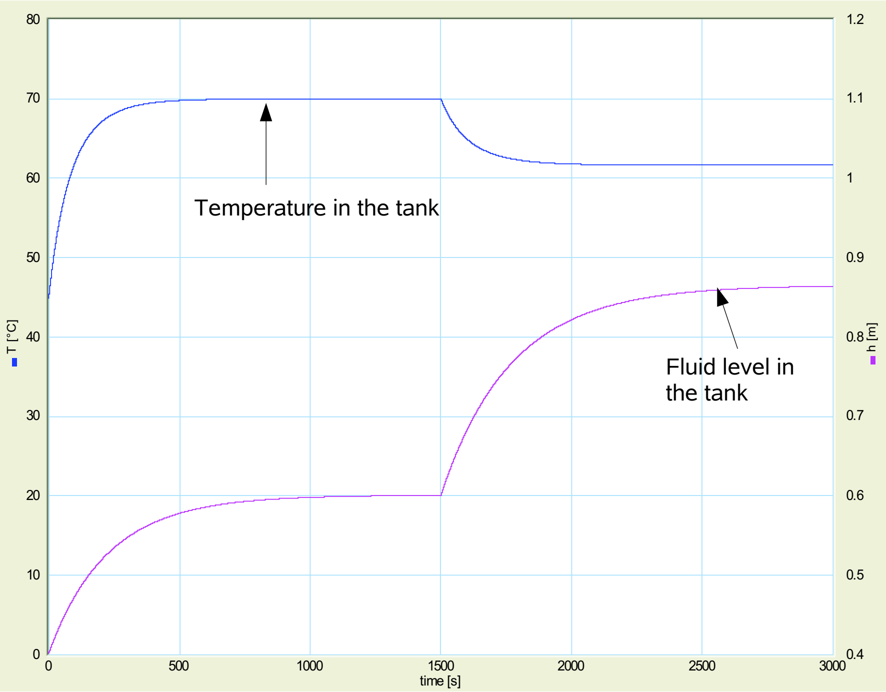

Fig. 12.77 Time evolution of the temperature and the fluid levels in the tank

The steady state values of fluid level and temperature in the tank obtained by simulation can be easily manually verified. Summation of mass flows at the upper 0-junction of the bond graph in Figure 12.76 gives

$$\dot{p} = \frac{1}{C_h}\,(\,\dot{m}_i\ -\ \dot{m}_o\,)$$

$$= \frac{1}{C_h}\,(\,\dot{m}_i \;-\; k_2\,\sqrt{p}\,)$$

$$= \frac{1}{C_h}\,(\,\dot{m}_i \;-\; k_2\,\sqrt{\varrho\,g\,h}\,)\;. \tag{12.86}$$

In steady state, the time derivative of the pressure vanishes. Hence,

$$h \;=\; \frac{\dot{m}_i^2}{k_2^2\,\varrho\,g}\;. \tag{12.87}$$

Using numerical values from Table 12.16 gives $h(t = 3000\,s) = 0.865\,m$.

The steady state value of the temperature in the tank is obtained accordingly. Summation of enthalpy flows at the lower 0-junction of the bond graph in Figure 12.76 in steady state gives

$$0 \;=\; \frac{1}{C_{therm}}\,[\,c_p\,\dot{m}_i\,T_i \;-\; c_p\,\dot{m}_o\,T \;+\; \dot{Q}\,]\;. \tag{12.88}$$

Hence,

$$T \;=\; T_i \;+\; \frac{1}{c_p\,\dot{m}_o}\,\dot{Q}\;. \tag{12.89}$$

The numerical result is $T(t = 3000\,s) = 61.66\,^oC$.

12.13 A Counterflow Heat Exchanger

This section illustrates how the pseudo bond graph approach can be conveniently used for modelling open thermodynamic systems. The example under study is a simple counterflow heat exchanger as is depicted in Figure 12.78. In [25], Scherf directly sets up the equations for a counterflow heat exchanger and uses them for a MATLAB®/Simulink®simulation. In this case study, the parameters given by Scherf are used. A bond graph model of a heat exchanger has also been presented by Thoma and his co-authors [27, 28]. It makes use of a non-standard element they call HEXA (Heat Exchanger).

The simple counterflow heat exchanger in Figure 12.78 can be considered as a tube carrying the cooling water with a counterflow hot oil stream passing through an inner tube. Both tubes have an inlet and an outlet. That is, each tube can be viewed as a control volume with a mass inflow and a mass outflow and can be presented by a pseudo bond graph similar to the one of a heated stirred tank in Section 10.1.1.

For simplicity, it is assumed that

- a one-dimensional concentrated parameter model is appropriate,
- no mass is accumulated in both tubes,
- hydraulic losses can be neglected in both tubes, and
- the wall of pipe enclosing the inner tube is perfectly insulating.

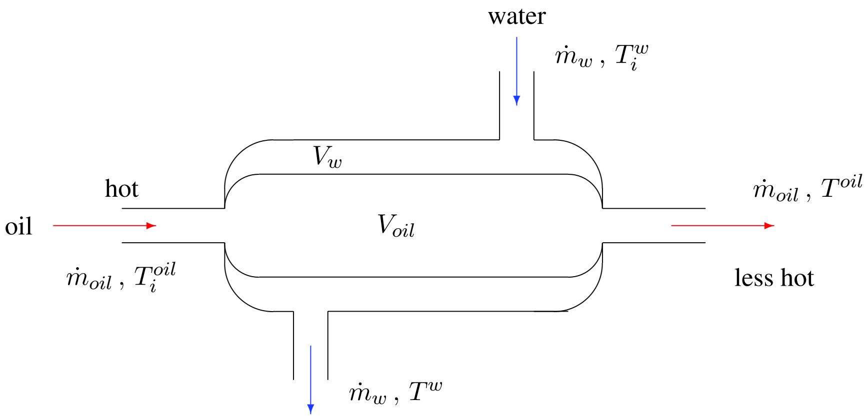

Fig. 12.78 Schematic of a counterflow heat exchanger

A Pseudo Bond Graph Model of the Counterflow Heat Exchanger

According to the pseudo bond graph model of a heated stirred tank (cf. Figure 10.5), Figure 12.79 shows a pseudo bond graph of the heat exchanger. The upper part of the pseudo bond graph model represents the outer tube with the cooling water. The lower part of same structure models the inner pipe carrying the hot oil stream. The hydraulic part of both submodels reduces to a 1-junction of the mass flow as mass accumulation and hydraulic losses have been neglected. Both submodels are coupled by a modulated resistor that accounts for the heat conduction from the hot inner pipe to the enclosing pipe. This R element is modulated by the upstream temperatures of water and oil. Its constitutive equations are

$$\Delta T = \frac{(\, T_i^{oil} - T^w \,) - (\, T^{oil} - T_i^w \,)}{\ln(\, T_i^{oil} - T^w \,) - \ln(\, T^{oil} - T_i^w \,)} \tag{12.90a}$$

$$\dot{H}^{oil} = k\, A\, \Delta T \tag{12.90b}$$

$$\dot{H}^{w} = k\, A\, \Delta T \ , \tag{12.90c}$$

where k denotes the thermal conductance coefficient (assumed to be constant) and A is the surface of the inner pipe effective in the heat exchange.

As pointed out in Section 10.1.1, the enthalpy flow into and out of each pipe does not depend on a temperature difference, but on the upstream temperature. Therefore, the bond with the downstream temperature is activated. Furthermore, the C element in the thermal part of both submodels is modulated, which is no problem in a pseudo bond graph.

The cooling water entering the heat exchanger is provided through a valve. In order to ensure a given constant temperature of the oil at the outlet, the actual tem-

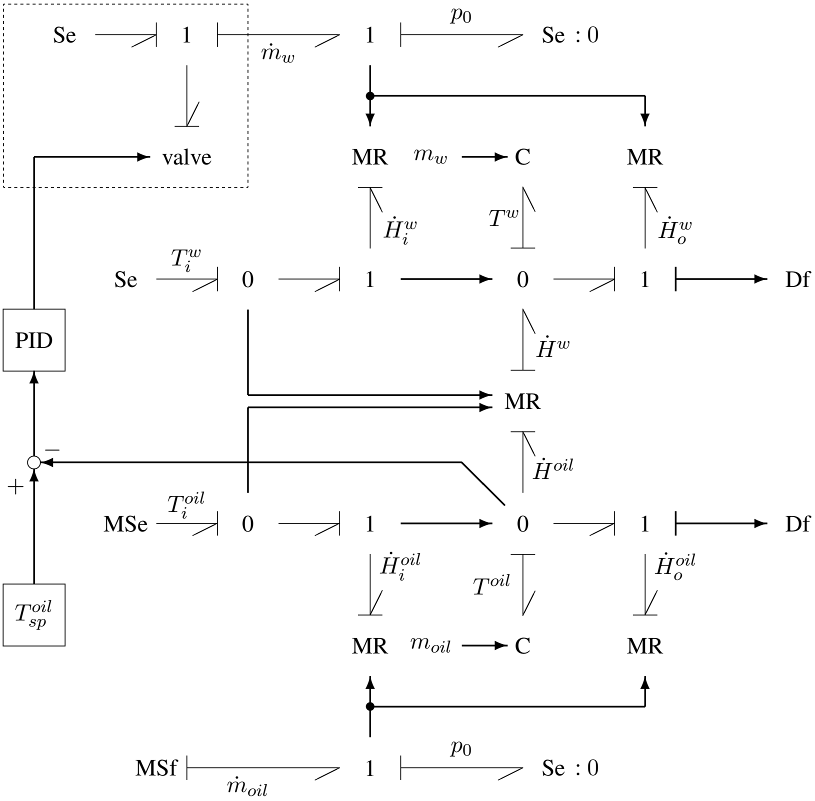

Fig. 12.79 Pseudo bond graph of the counterflow heat exchanger

perature is measured and compared with a set point value. The difference is fed into a PID controller that controls the opening of the water inlet valve. If details of the valve are known, a bond graph model can be developed for the valve. In this study, the limitation of the opening is taken into account by a signal saturation block. The dynamics of the valve opening are modelled by a first order lag signal block.

From the pseudo bond graph in Figure 12.79, the equations describing the dynamics of the heat exchanger are easily derived by summing up flows at the right-hand side 0-junctions. They are, in fact, power balances. The enthalpy flow entering the C element reads

$$\begin{aligned} c_{oil}\, m_{oil}\, \dot{T}^{oil} &= \dot{H}_i^{oil} - \dot{H}^{oil} - \dot{H}_o^{oil} \\ &= c_{oil}\, \dot{m}_{oil}\, T_i^{oil} - k\, A\, \Delta T - \\ &\quad c_{oil}\, \dot{m}_{oil}\, T^{oil} \end{aligned} \tag{12.91a}$$

Table 12.17 Parameters used for simulation runs

Parameter	Value	Units	Meaning
m_{oil}	75	kg	Oil mass in the heat exchanger
m_w	100	kg	Mass of water in the heat exchanger
A	5	m^2	Surface of inner pipe effective in heat conductance
k	85	$J/(s\,m^2\,K)$	Thermal conductance coefficient
c_{oil}	1600	$J/(kgK)$	Specific heat of the oil at constant volume
c_w	4200	$J/(kgK)$	Specific heat of the water at constant volume
$\dot{m}_{oil}$	500	kg/h	Oil mass flow
T_i^{oil}	120	^oC	Oil temperature at the inlet
T_i^w	10	^oC	Water temperature at the inlet

$$\begin{aligned} c_w\, m_w\, \dot{T}^w = c_w\, \dot{m}_w\, T_i^w \; + k\, A\, \Delta T \; - \\ c_w\, \dot{m}_w\, T^w \;, \end{aligned} \tag{12.91b}$$

where c_{oil} and c_w denote the specific heat at constant volume of the oil and the water.

Simulation of the Uncontrolled Counterflow Heat Exchanger

In order to see whether the model correctly reflects the dynamic behaviour of the heat exchanger, first, the uncontrolled system has been simulated. To that end, the parameters in Table 12.17 (cf. [25]) have been used.

If in steady state the outlet temperatures are to be $T_{oil} = 33.8\,^oC$ and $T_w = 43.0\,^oC$ respectively, then for the cooling water flow, the required mass flow is $\dot{m}_w = 0.1382\ kg/s$. Starting from this steady state, the oil mass flow is increased by 10% at $t = 1000\ s$. Furthermore, at $t = 5000\,s$, the temperature of the oil entering the heat exchanger rises from $5\,^oC$ to $125\,^oC$.

Figure 12.80 shows the step responses of the uncontrolled systems. Both events cause an increase in the outlet temperatures as to be expected. As can be seen, the dynamics of the increase are different. At $t = 1000\,s$ the outlet temperature of the oil rises much faster than the one of the water.

Simulation of the Controlled Counterflow Heat Exchanger

The transfer function of the PID controller is

$$U \;=\; K \left[1 + \frac{1}{T_i\, s} + \frac{T_d\, s}{1 + \dfrac{T_d}{N}\, s} \right] E \;, \tag{12.91c}$$

where $s \in \mathbb{C}$. E denotes the Laplace transform of the error into the controller and U the Laplace transform of the controller output. The parameters of the controller have been adopted from [25] and are given in Table 12.18.

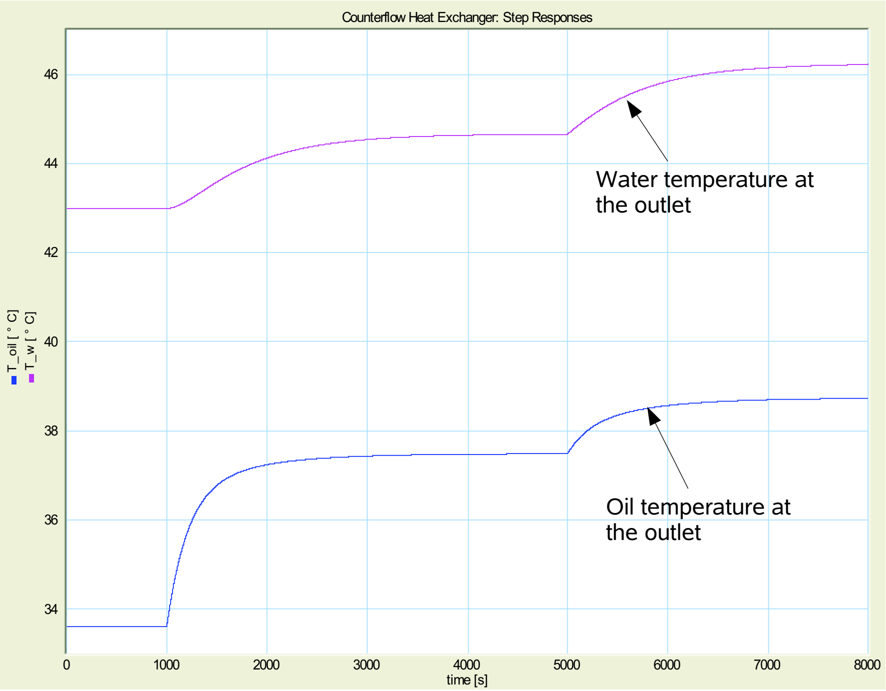

Fig. 12.80 Step responses of the uncontrolled system

Table 12.18 Parameters of the PID controller

Parameter	Value	Units	Meaning
K	-150		Proportional gain
Ti	630	s	Integral time constant
Td	63	s	Derivative time constant
N	63		Derivative gain limitation

As been mentioned above, the major characteristics of the valve have been modelled by a signal saturation block followed by a first order lag signal block with the transfer function $G(s) := k/(\tau s + 1)$. The minimum and the maximum output bound of the saturation block are 0 and 100 respectively. The proportional gain of the first order lag block is $k = 0.005$ so that the output of the valve is limited to $0.5\,kg/s$. The time constant of the first order lag block is $\tau = 1\,s$.

The initial value of the controller's internal integrator, $uI_0 = 27.7$, is the valve's opening that corresponds to the steady state value of the mass flow of the water flow, $\dot{m}_w = 0.1385\,kg/s$, required to maintain a steady state oil temperature $T_{oil} = 33.6\,^oC$ at the outlet.

Figure 12.81 depicts the oil temperature at the outlet of the controlled heat exchanger and the mass flow of the cooling water flow. At $t = 1000\,s$, the set point of

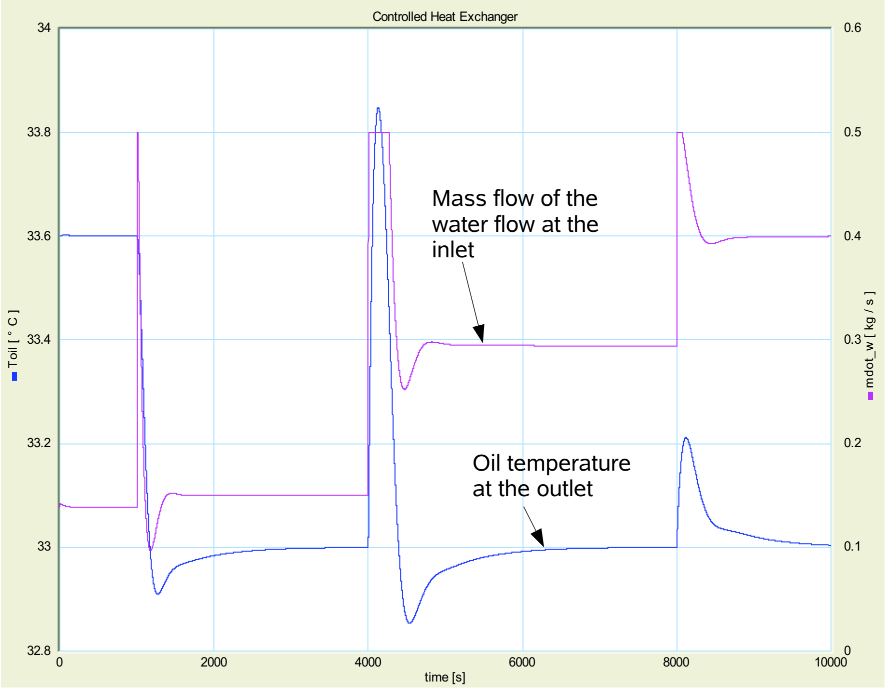

Fig. 12.81 Oil outlet temperature and mass flow of the cooling water flow for the controlled system

the oil outlet temperature instantly drops from $33.6\,^oC$ to $33.0\,^oC$. At $t = 4000\,s$, the mass flow of the entering oil is increased by 10% and at $t = 8000\,s$, the temperature of the entering oil rises by $5\,^oC$. In all three cases, after a more or less significant overshoot, the oil outlet temperature returns to the given set point value. The time evolution of the mass flow of the cooling water flow clearly shows the saturation of the valve.

12.14 Conclusion

In this chapter, bond graph methodology has been used in a number of small elaborated case studies. The aim has been to show that, in fact, bond graph modelling can cover the whole range of engineering applications from mechanical systems to electromechanical systems, robots, hydraulic and to open thermodynamic systems in a unified manner. A further objective of this chapter has been to illustrate the application of different features of bond graph modelling methodology.

- As to mechanical systems, an intuitive and convient modelling approach is to start by considering geometric relations, deriving kinematic constraints from

them and augmenting their bond graph representation so that a model of the system dynamics is obtained.
- Furthermore, classical Lagrange equations, e.g. for robots can be derived directly and systematically from a multibond graph representation. Of course, if simulation of the dynamic behaviour is the purpose and if a standard DAE solver is to be used then these second order ODEs are to be transformed into a set of first order ODEs.
- Three case studies, the engagement of a clutch (Section 12.6), dry friction in a suspension strut of a car (Section 12.7) and a DC-DC buck converter (Section 12.8) have been chosen to show how *hybrid* systems including discrete events can be modelled and simulated in bond graph framework.
- As to hydraulic systems, in general, it is sufficient and appropriate to use a hydrostatic approach. That is, the hydrostatic pressure is chosen as an effort and the amount of hydraulic power is approximated by the product of hydrostatic pressure and volume flow. This assumption has been used in the fluid level control of a three tank system.
- The bond graph model-based approach to FDI presented in Section 6.8 has been illustrated by means of the often used hydraulic two tank system.
- Finally, two small examples including the well known heated stirred tank problem (Section 12.12) and a counterflow heat exchanger (Section 12.13) have been chosen to illustrate the practical use of the pseudo bond graph approach.

In this presentation of a number of small case studies from various disciplines, emphasis has been on bond graph modelling. It has not been the aim to show how existing software can support bond modelling and simulation of the examples. There is one exception with the consideration of dry friction in a suspension leg. For this example, it has been shown in some detail how such a hybrid model, actually, can be computed by means of the open source mathematical software Scilab and the use of an ODE solver with root finding capability.

As to large bond graph models of complex systems, it is clearly beneficial to have some software available that supports a hierarchical modelling approach, provides component model libraries, can automatically set up model equations and can manipulate them symbolically before numerical solution is performed. For models of small up to medium size, an ordered set of model equations can also be derived manually from a causal bond graph in a systematic manner and can be directly formulated, e.g. in the script language of Scilab.

References

[1] B. Allard, H. Morel, Ph. Lautier, and J.M. Retif. Bond graphs for averaged modeling of power electronic converters. In J.J. Granda and G. Dauphin-Tanguy, editors, *Proc. of the 1997 International Conference on Bond Graph Modeling and Simulation*, volume 29(1) of *Simulation Series*, pages 201–206. SCS, 1997.
[2] K.E. Brenan, S.L. Campbell, and L.R. Petzold. *Numerical Solution of Initial-Value Problems in Differential-Algebraic Equations*. SIAM, 1996.

[3] F.T. Brown. *Engineering System Dynamics*. Marcel Dekker, New York, Basel, 2001. ISBN: 0-8247-0616-1.

[4] J. Buisson. Analysis and Characterisation of Hybrid Systems with Bond Graphs. In *1993 IEEE International Conference on Systems, Man and Cybernetics*, volume 1, pages 264–269, 1993.

[5] Y.H. Chin and D. Hollander. A DC to DC Converter for Notebook Computers Using HDT-MOS and Synchronous Rectification. Technical Report AN 1547/D, Motorola Inc., 1995.

[6] H. Christ. *Stationärer und instationärer Betrieb eines federnd gelagerten, unwuchtigen Motors*. PhD thesis, Technische Hochschule Karlsruhe, 1966.

[7] Controllab Products. 20-sim the power in modeling. URL http://www.20sim.com.

[8] J.J. Craig. *Introduction to Robotics Mechanics & Control*. Pearson Prenctice Hall, Upper Saddle, New Jersey, USA, 2005.

[9] P. Dransfield. *Hydraulic Control Systems – Design and Analysis of Their Dynamics*. Springer-Verlag, New York, 1981.

[10] J. Garcia-Gomez. *Approche bond graph pour la modélisation des effets thermiques dans les composants de commutation en lectronique de puissance*. PhD thesis, Université des Sciences et Technologies de Lille, Lille, France, 1997.

[11] J. Garcia-Gomez, G. Dauphin-Tanguy, and Ch. Rombaut. Average bond graph models of dc/dc power converters. In J.J. Granda and F.E. Cellier, editors, *Proc. of the 1999 International Conference on Bond Graph Modeling and Simulation*, volume 31(1) of *Simulation Series*, pages 338–343. SCS, 1999.

[12] P.J. Gawthrop and E. Ronco. A Sensitivity Bond Graph Approach to Estimation and Control of Mechatronic Systems. Technical Report CSC-99018, Centre for Systems and Control, Univ. of Glasgow, Faculty of Engineering, Dec 1999.

[13] P.J. Gawthrop and L. Smith. *Metamodelling: Bond Graphs and Dynamic Systems*. Prentice Hall International (UK) Limited, Hemel Hempstead, 1996. ISBN: 0-13-489824-9.

[14] A.C. Hindmarsh. ODEPACK A Systemized Collection of ODE Solvers. Preprint UCRL-88007, Lawrence Livermore National Laboratory, August 1982.

[15] J. Hoffmann. *MATLAB und Simulink – Beispielorientierte Einführung in die Simulation dynamischer Systeme*. Addison-Wesley, 1998.

[16] D.C. Karnopp. Lagrange's Equations for Complex Bond Graph Systems. *ASME Journal of Dynamic Systems, Measurement, and Control*, 99(4):300–306, December 1977.

[17] D.C. Karnopp, D.L. Margolis, and R.C. Rosenberg. *System Dynamics - Modeling and Simulation of Mechatronic Systems*. John Wiley & Sons Inc., Fourth edition, 2005. ISBN: 0-471-70965-4.

[18] D. Kölsch and G.P. Ostermeyer. Coulombsche Reibung in der Fahrzeugsimulation. *Automobil-Industrie*, 5:385–388, 1992.

[19] B. Messner and D. Tilbury. Control Tutorials for Matlab. URL www.engin.umich.edu/group/ctm/.

[20] H. Morel, B. Allard, H. Elomari, K. Ammous, D. Bergogne, and A. Ammous. Causality Analysis And State Initialization. In J.J. Granda and G. Dauphin-Tanguy, editors, *Proc. of the 2001 International Conference on Bond Graph Modeling and Simulation*, volume 33(1) of *Simulation Series*, pages 91–95. SCS, 2001.

[21] A. Mukherjee, R. Karmakar, and A.K. Samantaray. *Bond Graph in Modeling, Simulation and Fault Identification*. I.K. International Publishing House, New Delhi, India, 2006. ISBN: 81-88237-96-5.

[22] C.C. Pantelides. The consistent initialization of differential-algebraic systems. *SIAM, Journal of Scientific and Statistical Computation*, 9:213–231, 1988.

[23] K. Radhakrishnan and A.C. Hindmarsh. Description and use of LSODE, the Livermore solver for ordinary differential equations. Technical Report UCRL-ID-113855, Lawrence Livermore National Laboratory, December 1993.

[24] V. Ramaswamy. Interactive Power Electronics Online Course. URL http://www.powerdesignersusa.com/InfoWeb/ressources/pe_html/.

[25] H.E. Scherf. *Modellbildung und Simulation dynamischer Systeme*. Oldenbourg, 2004.

[26] Scilab Consortium. Scilab. URL http://www.scilab.org/.
[27] J.U. Thoma and B. Ould Bouamama. *Modeling and Simulation in Thermal and Chemical Engineering (A Bond Graph Approach)*. Springer-Verlag, Berlin, 2000.
[28] J.U. Thoma and G. Mocellin. *Simulation with Entropy in Engineering Thermodynamics*. Springer, Berlin, Heidelberg, New York, 2006. ISBN -10 3-540-32798-3.
[29] M. Vergé and D. Jaume. *Modélisation structurée des systèmes avec les Bond Graphs*. Edition Technip, 2003. ISBN: 2-7108-0838-2.